# Quantum correlations in mesoscopic systems

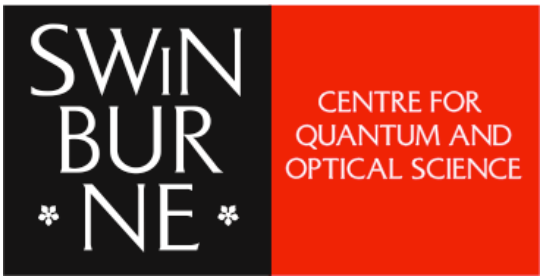


**Run Yan Teh**

Swinburne University of Technology

Submitted in total fulfilment of the requirements of the degree of Doctor of Philosophy.

January 2018

# Acknowledgements

First and foremost, I would like to thank my supervisor, Margaret Reid, for making my dream come true. It is a privilege to be able to research physics, especially on the foundational issues in quantum physics. I think it is rare for a PhD student, in the three year candidature, to love all the projects assigned by a supervisor. I loved and greatly enjoyed working on every single one of my projects. They are full of insights, with complete understanding from grinding the mathematics. For this, I can not thank Margaret enough.

While Margaret is a person with few words, the same cannot be said about the next person I want to thank, my co-supervisor, Peter Drummond. From Beltway bandits to the existence of aliens, from the tragedy of commons to the sinking of the Rainbow Warrior, one cannot but be impressed by the knowledge he possesses. His wide range of interests reflects on the areas of physics involved in his publications.

I would like to thank my colleagues and collaborators. Laura Rosales-Zarate's efficiency, valuable work ethics and extensive notes keeping greatly helped the progress of our projects. I enjoyed working with Laura and her laughter immensely. Bogdan Opanchuk and Simon Kiesewetter for their expert computational and programming skills. Qiongyi He, a hardworker and go-getter, took great care of me and discussed quantum correlations extensively with me in the early stage of my candidature. Rodney Polkinghorne and King Lun Ng for the many thought-provoking discussions. Bryan Dalton who is dedicated to understanding quantum correlations and always generous in sharing references.

Special thanks to Chris Vale, his distinct thinking constantly serves as a reminder on what physics is as a big picture; especially when I find myself elbow-deep in calculations and programming. Berthold-Georg Englert who encouraged me to grit my teeth when the going got tough, and Valerio Scarani who introduced Bell inequalities and more. They shaped my understanding of quantum physics so deeply, and all of them played a huge part in helping me pursue my postgraduate study.

My Italian colleagues, Alessandro Brolis, whom I shared memorable conversations with; Toniolo

Umberto, a mathematical physicist who is both passionate and integrous; Fabio Novelli, my intelligent yet humble friend with admirable physics intuition. Also, I want to thank Pavel Kolesnichenko for his listening ears; Xia-Ji Liu, Kavan Modi, Russell McLean and Tatiana Tchernova for all assistance and advice rendered.

Last but not least, I would like to thank my family for their endless support. My loving wife, Ju Lea, and darling daughter, Gemma, for bringing me all the joy in the world.

# Declaration

This is to certify that this thesis

- contains no material which has been accepted for the award to me of any other degree or diploma, except where due reference is made in the text,
- to the best of my knowledge contains no material previously published or written by another person except where due reference is made in the text, and
- where the work is based on joint research or publications, discloses the relative contributions of the respective workers or authors.

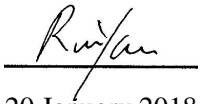

20 January 2018

# Abstract

Quantum correlations arise from the quantum superposition in quantum states. In this thesis, we present criteria to certify quantum correlations that are immediately applicable to experiments. They only involve the statistics of measurable observables and are hence, state independent. Based on these criteria, we study the monogamy of entanglement, concerned with the shareability of entanglement. These criteria are indispensible tools in investigating quantum mechanics in macroscopic systems.

Quantum superpositions are fragile, especially so in macroscopic systems due to decoherence. In the advent of cooling technologies and clever techniques in isolating quantum systems from its environment, quantum states in macroscopic systems have been created. Identifying the existence of a macroscopic quantum state is then one of the most important problems. We present a test for quantum coherence, which of course is the source of quantumness of a quantum state. The quantum coherence test involves an observable which is measurable in experiments. We relate the observable in the quantum coherence test to fidelity, allowing the fidelity to be computed in experiments. The ability to compute fidelity is important as it features in many quantum information protocols such as quantum teleportation and quantum state transfer.

We continue the investigation of quantum mechanics in macroscopic systems by considering an optomechanical system. It is a tangible macroscopic system that has been demonstrated to behave quantum mechanically. In fact, quantum protocols such as quantum state transfer and quantum entanglement have been realised in optomechanical systems. In the analyses of the optomechanical system, adiabatic and linearisation approximations are often employed in the literature. In this thesis, phase space methods in the truncated Wigner and positive P representations are used. They enable optomechanical systems to be simulated without any approximations. In particular, we simulated specific protocols for optomechanical quantum memory and quantum entanglement between two optomechanical systems.

In the optomechanical quantum memory simulation, there are deviations in the results using phase

space methods from the results within the linearisation approximation. Power spectral density reveals spectral overlap between control and signal fields, which is not taken into account in analysis using linearisation approximation. Fidelity of the output state with respect to the input state quantifies the efficiency of optomechanical state transfer and we show how this is computed using phase space methods.

Finally, we analyse entanglement generation between two optomechanical systems that could serve as a testing ground for Furry's hypothesis.

# Publications from this thesis

1. R. Y. Teh and M. D. Reid, *Criteria for genuine N-partite continuous-variable entanglement and Einstein-Podolsky-Rosen steering*, Phys. Rev. A **90**, 062337 (2014).

2. S. Armstrong, M. Wang, R. Y. Teh, Q. H. Gong, Q. Y. He, J. Janousek, Hans-A. Bachor, M. D. Reid, and P. K. Lam, *Multipartite Einstein-Podolsky-Rosen steering and genuine tripartite entanglement with optical networks*, Nat. Phys. **11**, 167 (2015).

3. L. Rosales-Zárate, R. Y. Teh, S. Kiesewetter, A. Brolis, K. Ng, and M. D. Reid, *Decoherence of Einstein–Podolsky–Rosen steering*, J. Opt. Soc. Am. B **32**, A82 (2015).

4. R. Y. Teh, L. Rosales-Zárate, B. Opanchuk, and M. D. Reid, *Signifying the nonlocality of NOON states using Einstein-Podolsky-Rosen steering inequalities*, Phys. Rev. A **94**, 042119 (2016).

5. B. Opanchuk, L. Rosales-Zárate, R. Y. Teh, and M. D. Reid, *Quantifying the mesoscopic quantum coherence of approximate NOON states and spin-squeezed two-mode Bose-Einstein condensates*, Phys. Rev. A **94**, 062125 (2016).

6. S. Kiesewetter, R. Y. Teh, P. D. Drummond, and M. D. Reid, *Pulsed entanglement of two optomechanical oscillators and Furry's hypothesis*, Phys. Rev. Lett. **119**, 023601 (2017).

7. R. Y. Teh, S. Kiesewetter, M. D. Reid, and P. D. Drummond, *Simulation of an optomechanical quantum memory in the nonlinear regime*, Phys. Rev. A **96**, 013854 (2017). – Selected to be an Editors' Suggestion.

8. L. Rosales-Zárate, R. Y. Teh, B. Opanchuk, and M. D. Reid, *Monogamy inequalities for certifiers of continuous-variable Einstein-Podolsky-Rosen entanglement without the assumption of Gaussianity,* Phys. Rev. A **96**, 022313 (2017).

# Summary of contributions

I am grateful for the support of my colleagues in carrying out the work of this thesis. I wish to give a direct acknowledgement of the way in which each colleague helped my work and also to summarise my individual contribution.

For the work done in Chapter 1 of this thesis, on genuine CV multipartite entanglement, the direction of the research and all the mathematical proofs were carried out solely by myself and my supervisor, Margaret Reid. The development of the algorithms and the tests of the criteria for given physical models were my sole responsibility. I thank Qiongyi He, now at Peking University, whose efforts lead to a collaboration with the Australian National University quantum optics experimental group, thus helping to motivate this research.

For the work done in Chapter 2, on the steering and quantum coherence of the NOON states, the strategies for the direction of the research were developed in collaboration with my supervisor Margaret Reid, associate supervisor Laura Rosales-Zarate, and postdoctoral researcher Bogdan Opanchuk. I was solely responsible for the calculation of the steering and correlation moments, both analytical and numerical, and the necessary modelling for realistic systems. However, every calculation was independently checked by either Laura Rosales-Zarate or Bogdan Opanchuk, with whom I worked closely on this project.

The motivation for Chapters 4 and 5, on optomechanical memory and quantum correlations of optomechanical systems, arose from discussions with both my supervisors and Simon Kiesewetter. I was responsible for, and suggested to investigate, nonlinear effects in memory, as outlined in Chapter 3. I carried out all the necessary phase-space calculations and numerical simulations, in close collaboration with my supervisor Peter Drummond. To do this, I used the open source software toolbox xSPDE, based on Matlab, developed by Peter Drummond, Simon Kiesewetter and Rodney Polkinghorne available at www.github.org. The toolbox provides basic integration code for stochastic equations and required

custom-written code extensions that were written and tested by me in order to carry out the research. The calculations and simulations were independently checked by PhD student Simon Kiesewetter, who used a different routine based on his own code. I was solely responsible (with suggestions and feedback from my co-authors) for the writing of the paper on this material, now published in Physical Review A. This writing essentially forms Chapter 4 of this thesis. For Chapter 5, Simon Kiesewetter and I reversed roles, with Simon undertaking the initial work in regard to the solutions for the entangled optical modes, and the solutions for the creation of the mechanical entanglement with a read-out mechanism. However, I independently checked the theory and all linearised calculations, using my own code based on the Matlab xSPDE program. I also contributed significantly by developing the analysis of the pulse strategy of Chapter 4 that is used to store and retrieve the entangled quantum state. Finally, the results on the monogamy of entanglement presented in Appendix A are the collaborative work of Margaret Reid, Laura Rosales-Zarate, Bogdan Opanchuk and myself.

# Contents

# List of Figures

# Part I

# Introduction

Albert Einstein was bothered by quantum entanglement. Its existence, however, is an indisputable experimental fact. Entanglement derives from the fact that quantum superposition in quantum states exists in nature [2–4]. Using an entangled quantum state, Einstein, together with Podolski and Rosen pointed out the contradiction between the completeness of quantum mechanics and the intuitive notion of local realism [5]. They considered a system of two particles where their positions are correlated and their momenta anticorrelated. Two spatially separated detectors measure either the position or momentum of the particles. The position of one particle can be inferred from the measurement of another particle's position. Similarly, a measurement of one particle's momentum allows perfect inference of the other particle's momentum.

At first sight, there is nothing extraordinary about these inferences. We assume both the position and momentum of a particle have predetermined values and these quantities are said to possess physical realities. Also, these particles should satisfy the notion of locality, in the sense where faster-than-light information transfer/signalling is not possible. These properties of the system's state are intuitive and we expect them to always hold. The original EPR paper described these two properties so clearly we quote them below [5]:

- "If, without disturbing a system, we can predict with certainty the value of a physical quantity," then "there exists an element of physical reality corresponding to this physical quantity." The element of reality represents the predetermined value for the physical quantity.

- The locality assumption postulates that no action at a distance, so that measurements at a location $B$ cannot immediately "disturbs" the system at a spatially separated location $A$.

These two premises, i.e. the existence of elements of physical reality and locality constitute what is known as the local realism. Analysis of the EPR paper demonstrated a paradox. What we expect to be true might not be so: Local realism seems to be violated by certain quantum states that are allowed by quantum physics. Is it really the case that local realism does not always hold or is the formalism of quantum mechanics incomplete?

The current (and possibly the only correct) understanding is that quantum mechanics is complete, in the sense that all predictions of quantum mechanics agree with the corresponding experimental results. Following the argument of EPR then, it is the notion of local realism that has to be questioned. Of course, the breakdown of local realism does not mean the absence of physical reality, but rather, our understanding of what physical reality is has to be updated, something Einstein has not for the first time

compelled us to do.

The philosophical debate on the objective reality and the interpretation of a quantum state are still ongoing. At the same time, scientists embrace quantum mechanics and advance the field of quantum information and computation. Entangled pairs of quantum particles separated by 1200 kilometers away were recently created [6]. It is the quantum correlations that bring new paradigm in computations, and it is essential to characterise and quantify them.

Correlations in physical states that satisfy local realism can only be established by one of the two possible mechanisms: signalling and pre-established agreement [7–9]. Let's first consider the signalling mechanism in a bipartite system. A party could measure an observable and communicate the information of both the observable and its corresponding outcome to the other party. The receiving party will carry out a measurement and the corresponding outcome is somehow influenced by the received information such that correlation between the two parties is established. Signalling can be ruled out by separating the two parties spacelike away and as far as we can tell, signalling is not the mechanism. Or, they could establish correlated predetermined values for all possible observables before being measured. These mechanisms are encapsulated in the hidden variables in the so-called hidden variable models to explain quantum correlations. These variables are "hidden" because they are not given in the description of quantum correlations in quantum physics, and serve to reveal the incompleteness of quantum mechanics.

Quantum states that violate local realism then contain quantum correlations which cannot be explained by these two mechanisms. This statement is non-trivial and was discussed, debated and tackled by many of the pioneers in the early days of quantum mechanics. However, it was John Bell who put this issue to rest with his famous Bell inequality [10]. The logic behind the inequality is crystal clear, its conclusion is irrefutable. Bell constructed a mathematical relation that has to be satisfied if local realism were true. He showed that quantum mechanics violates this relation. Since the reasoning leading to the mathematical relation is correct, the assumption must be incorrect. In his work, Bell considered a set of observables and calculate the mathematical bound that these observables have to satisfy if the physical states contain correlations that comply with local realism. Certain quantum states exceed the bound and violate the inequality, which implies the assumption in the derivation of inequality is invalid; quantum correlations have no classical explanation. There are no hidden variables to account for the quantum correlations.

It is perhaps worth stating one of the most widely used Bell inequalities here to demonstrate the

features of the inequality. The inequality is devised for a bipartite system, each party has two possible measurement settings denoted by 0 and 1 with two possible outcomes for each measurement setting, also denoted by 0 and 1. The CHSH inequality is given by [11]

$$E_{00} + E_{01} + E_{10} - E_{11} \leq 2\,, \tag{1}$$

where $E_{xy}$ is the average or expectation value of the observable with measurement settings $x \in \{0,1\}$ and $y \in \{0,1\}$ for the two parties respectively. The inequality (1) depends on the statistics of certain observables which need not concern us here and the bound is satisfied by assuming that the statistics of these observables come from a physical state with classical correlation. It is found that the inequality is violated by a Bell state, defined as:

$$|\psi\rangle = \frac{1}{\sqrt{2}}\left(|01\rangle + |10\rangle\right), \tag{2}$$

where the state could represent, for instance, the spin state of two spin-$\frac{1}{2}$ particles or the polarisation state of a pair of photons. Bell inequalities have the advantage that their derivations do not depend on the specific physical states but rather the nature of these states and are hence general. Also, Bell inequalities involve observables that are measurable in experiments. In this thesis, all criteria for quantum correlations are derived in the same vein as a Bell inequality: A set of observables are chosen and we find the inequality that the statistics of these observables has to satisfy, based on the assumption of the nature of physical states we are investigating. The violation of the inequality then implies our assumption to be false.

**Remark**: It is often confusing in the literature involving jargons such as action-at-a-distance and quantum nonlocality. The author discusses these notions below.

Action-at-a-distance is a concept that implies something that happens at one point in spacetime can affect something else which is spacelike separated instantaneously. A physical theory might be formulated in such a way that seems to suggest action-at-a-distance is at work. Newton's law of gravity is such an example. However, so far, there is no physical phenomena that exhibit this property. In the case of the gravitational law, all action-at-a-distance can be explained by general relativity. In quantum mechanics, action-at-a-distance does not exist too. This is because it will be possible, for instance, to send superluminal signal using quantum correlation in a quantum state if action-at-a-distance were true.

A physical theory that does not allow action-at-a-distance is a local one. Quantum mechanics is a local theory; correlations in quantum states have a local origin. So, what is the claim then that quantum mechanics is nonlocal? In order to understand the origin for this statement, consider the Bell state (2), which is a quantum state. This state carries correlation-at-a-distance. The correlation is preserved and observed even when the two particles are spacelike separated. This is not surprising as correlation-at-a-distance does exist in the classical world.

Let us continue with the Bell state in Eq. (2). If spin measurements along a same, fixed axis for both the particles are carried out, the results predicted by this quantum state are anticorrelated. In fact, this correlation can be explained by pre-established agreement. Their values must have been pre-determined before being measured such that they are anticorrelated and measurements only serve to reveal this correlation. Even though quantum mechanics predicts the same result for these measurement settings, the description of the quantum state is different. Before being measured, the quantum state is in a quantum superposition state of the two possible states and the spin values of these particles do not exist. The argument for nonlocality of quantum mechanics then goes as follow: Since spin values of these particles do not exist before measurement but the anticorrelation in spin values exists nevertheless, the measurement outcome of one spin value must have somehow affected the measurement outcome of the other spin value. Recall that the two particles are spacelike separated with no signalling allowed. It then seems to suggest that this quantum correlation is nonlocal in nature and hence quantum mechanics is nonlocal.

Hence, the term "nonlocal correlations" in literature translates to mean probability distributions that cannot be reproduced by pre-established agreement [7–9] (this will be explained in the next section). To avoid confusion, in this thesis, we use the generic term "quantum correlations".

**Remark**: The argument for quantum nonlocality is often summarised by the collapse of wavefunctions. The author takes the viewpoint that the argument for nonlocality amounts to searching for mechanisms for the observed correlation. No mechanisms exist, as far as we can tell. It is worth reminding the readers a few irreducible, fundamental facts of quantum mechanics. First of all, quantum superposition exists and it holds true for any number of parties/modes. This is the origin of quantum correlations. Secondly, these quantum correlations have a local nature in the sense that they are established locally. Finally, when observables are measured, the outcomes are randomly realised, obeying the probabilities prescribed by a quantum state.

## 0.1 Different classes of quantum correlations

As we consider physical states and their statistics for some observables, different assumptions can be given to the nature of these physical states. These different assumptions form different classes of quantum correlations. In this thesis, we consider three classes of quantum correlations, namely quantum entanglement, EPR-steering and Bell nonlocality. We define these three classes of quantum correlations for bipartite systems in this section.

Since quantum mechanics is probabilistic and measurement outcomes of a physical system can be formulated in terms of probability distributions in general, we classify correlations in terms of probability distributions. Let us first establish the notation. We denote the two parties $A$ and $B$ with their corresponding measurement settings $m_A$ and $m_B$ respectively. Of course, there are many settings they can choose from. In other words, the measurement settings $m_A$ and $m_B$ are elements of the sets of possible measurements, i.e. $m_A \in M_A$ and $m_B \in M_B$. Similarly, their corresponding outcomes are $a \in D_A$ and $b \in D_B$, where $D_A$ and $D_B$ are the sets of possible outcomes of measurements for party $A$ and $B$ respectively. We consider the joint probability distribution because any correlations between the two parties can be characterised by joint probability distributions. The joint probability distribution of observing outcomes $a$ and $b$ from measuring $m_A$ and $m_B$ is denoted by $P(a,b|m_A,m_B)$. Following Scarani [8], the set of joint probability distributions for all possible measurement outcomes for all possible measurement settings is called the observed statistics $P_{M_A,M_B}$:

$$P_{M_A,M_B} = \{P(a,b|m_A,m_B), a \in D_A, b \in D_B\}_{m_A \in M_A, m_B \in M_B} \tag{3}$$

This set contains $M_A M_B$ probability distributions, where each probability distribution is specified by

$m_A m_B$ numbers. Of course, the observed statistics must arise from a physical state.

### 0.1.1 Bell nonlocality

Having established the notation, we proceed to describe the joint probability distribution we can infer from experimental measurements. Since measurements are made by both parties $A$ and $B$ separately, they can each write down their probability distributions of their measurements $P(a|m_A)$ and $P(b|m_B)$ respectively. If the joint probability distribution is a product of the separate probability distributions $P(a|m_A)$ and $P(b|m_B)$, i.e. $P(a,b|m_A,m_B) = P(a|m_A)P(b|m_B)$, then the two parties are not correlated. In order to explain any correlations between the two parties, we introduce the variable $\lambda$ that describes the observed correlations. The joint probability distribution for two parties with correlations between them can then be expressed as [10]

$$P(a,b|m_A,m_B) = \sum_i P(\lambda_i)\,P(a|m_A,\lambda_i)\,P(b|m_B,\lambda_i)\,. \tag{4}$$

The observed statistics with joint probability distributions in the form (4) has a local hidden variable. In local hidden variable models, the variable $\lambda$ serves as the local hidden variables that explain the observed correlations. The "local" in the local hidden variable model is implicit in the expression for the probability distributions $P(a|m_A,m_B,\lambda_i) = P(a|m_A,\lambda_i)$ and $P(b|m_B,m_A,\lambda_i) = P(b|m_B,\lambda_i)$, where the probability distribution for the outcome $a$ ($b$) only depends on the measurement setting $m_A$ ($m_B$) and this means no signalling. In this model, correlations between the two parties are restricted to those that arise from the pre-established agreement mentioned in the previous section. When the observed statistics admit no local hidden variable, the physical state that gives rise to the joint probability distribution is said to be Bell nonlocal.

Bell inequalities are derived as a consequence of Eq. (4) and their violation, therefore, rules out local hidden variable models for certain quantum states [9]. These inequalities do not rule out nonlocal hidden variable models, where locality here is in the context of relativity theory with no signalling. However, as mentioned previously, there is no experimental evidence for signalling and hence nonlocal hidden variable models do not concern us here.

### 0.1.2 Quantum entanglement

We saw how Bell nonlocality is defined. In that case, the probability distributions $P(a|m_A,\lambda)$ and $P(b|m_B,\lambda)$ can be any valid probability distributions. We could restrict these probability distributions to those that satisfy probability distributions arising from a quantum state, denoted by $P_Q(a|m_A,\lambda)$ and $P_Q(b|m_B,\lambda)$. Mathematically, they are obtained using

$$P_Q(a|m_A,\lambda) = \mathrm{Tr}_B\left(\rho \Pi^a_{M_A} \otimes I\right), \tag{5}$$

where $\rho$ is the density operator characterising the quantum state of the bipartite system, $\Pi^a_{M_A}$ is a projection operator that returns the outcome $a$ for the measurement setting $M_A$ for the party $A$ and the trace is carried out on the other party $B$.

Now, the joint probability distribution $P(a,b|m_A,m_B)$ corresponds to a physical state that is separable if the joint probability can be expressed as

$$P(a,b|m_A,m_B) = \sum_i P(\lambda_i) P_Q(a|m_A,\lambda_i) P_Q(b|m_B,\lambda_i). \tag{6}$$

If the observed statistics with joint probability distributions cannot be expressed in the form (6), the corresponding physical state is a quantum entangled state.

Hence, depending on the assumption of the nature of a physical state that is reflected on the probability distributions, we obtain different classes of quantum correlations. It is straightforward to see that Bell nonlocality is a stricter class of quantum correlations. A physical state with joint probability that cannot be expressed in the form (6) can still, in principle, be expressed in the form (4). In other words, a quantum entangled state could still be explained by a local hidden variable model: classical mechanism for correlations in a quantum entangled state can be found.

**Remark:** Entanglement was first coined by Schrodinger [12] where a pure quantum state was considered. The detection and characterisation of entanglement in a mixed state is non-trivial and were first studied by Werner [13], Peres [14] and Horodecki et al. [15].

### 0.1.3 EPR-steering

Following the same exercise as in the case of quantum entanglement, we could choose to describe the probability distribution of one party, say $A$, to be any valid probability distribution $P(a|m_A,\lambda)$ while choosing the probability distribution of another party to come from a quantum state $P_Q(b|m_B,\lambda)$.

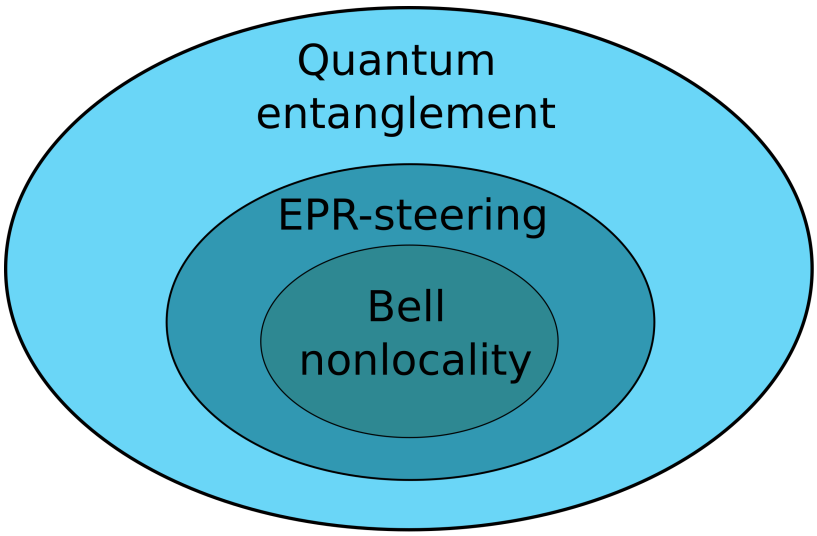


Figure 1: Different classes of quantum correlations and their relations. The Bell nonlocality has a stronger quantum correlation that is harder to demonstrate, and hence constitutes a smaller subset of quantum correlations. A Bell nonlocal state is also an EPR-steering state and a quantum entangled state, which is to say these different classes of quantum correlations are not mutually exclusive. Detailed discussions to be found in the main text.

This constitutes another class of quantum correlation which is called EPR-steering. Steering was first considered by Schrodinger [16] in his response to the EPR paper. It is only after much later that an experimental criterion that demonstrates steering was derived [17]. The wider concept of steering has been developed and formalised by Wiseman et al. [18], and the term "EPR-steering" was coined in Cavalcanti et al. [19].

In the literature, a local hidden state (LHS) is a physical state where the observed statistics has joint probability distributions $P(a,b|m_A,m_B)$ that can be expressed as [18]

$$P(a,b|m_A,m_B) = \sum_i P(\lambda_i) P(a|m_A,\lambda_i) P_Q(b|m_B,\lambda_i) \,. \tag{7}$$

Of course, we could have chosen the probability distribution for party $A$ to come from a quantum state instead. This suggests that, unlike Bell nonlocality and quantum entanglement, EPR-steering is directional and asymmetric. This feature has led to many interesting ideas and proposals for applications, for example the one-sided device independent quantum key distribution (QKD) [20].

Here, we discuss the relation between the three different classes of quantum correlations presented above. The different classes arise from the different assumptions placed on the statistics of the measurement outcomes. We reiterate what has been described previously. In a local hidden variable model

(which is a classical model), the only requirement on the observed statistics is that they come from a valid probability distribution. The joint probability distribution that cannot be expressed as Eq. (4) must then be nonclassical and is said to be Bell nonlocal. On the other hand, a quantum state that contains quantum entanglement cannot be explained by a separable model. In this model, we assume that the probability distributions come from a quantum state. Since we restrict these probability distributions to arise from a quantum state, the violation of the separable model does not rule out the local hidden variable model, where no assumptions on the probability distributions are made. Hence, a quantum entangled state could, in principle, be explained by a local hidden variable model. In other words, the local hidden variable model cannot be ruled out in a quantum entangled state. In this sense, the Bell nonlocality has a stronger nonclassicality than both the EPR-steering and quantum entanglement, with the EPR-steering containing a stronger nonclassicality than quantum entanglement. We note that these different classes of quantum correlations are not mutual exclusive. If a physical state is found to demonstrate the Bell nonlocality, then the state also contains both the EPR-steering and quantum entanglement. All discussions in this paragraph is encapsulated by a Venn diagram, as shown in Fig. 1.

## 0.2 Thesis rationale and overview

Studies of quantum correlations not only allow understanding of the fundamental issues in quantum mechanics, it also has practical applications, especially in the field of quantum information and computation. Quantum entanglement is the most widely featured resource in a plethora of quantum protocols. It is used in quantum cryptography [21–25] where entanglement allows quantum key distribution between two parties, which ensures secure encryption of messages exchanged between them. Another astonishing protocol is quantum teleportation [26–28] where shared entanglement between two parties is required for the transmission of quantum states with high fidelity. It is then essential to detect and quantify quantum correlations that exist in a quantum state. This is no easy task. There is no single universal criterion that verifies the presence of quantum correlations. To make matter worse, the characterisation and quantification of quantum correlations in mixed states are highly non-trivial. For instance, Werner states [13], which are mixed entangled states, do not violate any Bell inequality. More recently, it has been shown by Opanchuk et al. [29] that continuous variable entanglement can be faked

if the entanglement criterion is not chosen appropriately. In that work, the positive Wigner function of a two-mode squeezed state is used to generate a string of classically correlated numbers that are sent to two separated observers Alice and Bob. If a third party Charlie believes that the numbers are generated using quantum optical measurement devices in a laboratory, he may use the Tan-Duan CV entanglement criterion to incorrectly deduce that Alice and Bob share an entangled state. The work of Opanchuk et al. [29] showed that if one party (Alice) can be trusted to report to Charlie only the results of genuine quantum measurements, then an EPR-steering criterion can be used to certify whether entanglement is genuinely shared between the two parties. In this context, criteria that verify stronger non-classicality as described in the previous section are thus required to show that quantum correlations really do exist in a quantum state. This is to do with the issue of device-independent criteria [20, 30, 31]. Hence, it is not only important to detect the presence of quantum correlations but also to classify and quantify them.

There are various approaches in determining and characterising different classes of quantum correlations. One of the approaches involves convex analysis. We briefly describe how this approach is used to derive criterion that certifies the Bell nonlocality for a given physical state. Criteria for other classes of quantum correlations can be derived similarly. First, consider probability distributions in the observed statistics in Eq. (3) that admits local hidden variable model, which can be expressed in the form of Eq. (4). These probability distributions are elements of a set called the convex set. The problem can then be turned into a geometrical one, where elements in the convex set are now represented as points in higher dimensional space, which form a geometrical object called polytope. For example, a polygon is a two-dimensional polytope. Now, a hyperplane, a higher dimension plane, called the facet can be defined. From this, a vector $n$ normal to the facet can be found such that any point $p$ on this facet satisfies the relation $n.p = f$, where $f$ is a number. It can be shown that for a probability distribution that admits local hidden variable model $p_{local}$, it satisfies the inequality $n.p_{local} \leq f$. A probability distribution with Bell nonlocality will then violate this inequality. For a detailed description of this approach, readers are referred to the paper of Scarani [8]. In that paper, an explicit example showing the derivation of the CHSH inequality using this approach can be found. Note that in the derivation of the CHSH inequality, there are only two measurement settings with two possible outcomes for each setting. For larger number of measurement settings and outcomes, this approach has to be solved numerically. In the case of continuous variable systems where the outcomes have continuous values, this approach is not feasible. In summary, these approaches are rather abstract and not immediately applicable to

experiments.

In this thesis, we devise criteria that unambiguously detect different classes of quantum correlations. These criteria are similar to the EPR-Reid criterion, which is a criterion first derived by Reid [17] to demonstrate the inconsistency between local realism and completeness of quantum mechanics. This is where the condition of reality as discussed in the EPR paper was extended to include physical quantities that have intrinsic uncertainties. These criteria involve measurable observables and their statistics, making them readily applicable in experiments, and are examples of EPR-steering criteria. Recall the joint probability distributions that admit a local hidden state or a separable state. They contain probability distributions that arise from quantum states as in Eq. (5) which satisfy Heisenberg uncertainty principle. Eq. (5) suggests that the knowledge of density operator is required to obtain the corresponding probability distribution and hence the resulting criteria will be state dependent. As we will show in Chapter 1, the explicit quantum state does not appear in the derivation and only the quantum nature of the state which is manifested by the Heisenberg uncertainty principle is used to bound these quantum correlations criteria. Also, these criteria can be used to investigate other quantum properties of a quantum state such as the monogamy of quantum entanglement, which aims to find out the shareability of quantum entanglement.

With these criteria, we are at a better position to tackle the foundational question that is as old as quantum mechanics: Can quantum properties and quantum correlations persist in mesoscopic/macroscopic systems? There is nothing that rules out quantum properties in macroscopic systems in the formalism of quantum mechanics. However, we do not really observe quantum strangeness in the everyday classical world. There seems to be a border separating quantum physics from classical physics. There is a prevailing sense that quantum physics governs the microscopic regime while the macroscopic regime by classical physics. This idea is misleading, especially in the advent of technology where experimentalists are constantly attempting to coax macroscopic systems into behaving quantum mechanically.

To this end, we should mention that there are many views on what constitutes a macroscopic quantum system. The most intuitive macroscopic systems are massive or large objects. These objects are tangible and they obey classical mechanics typically. If these objects do behave quantum mechanically, we say that they are macroscopic quantum systems. An example of such systems is an optomechanical system. A quantum system can also be considered a macroscopic one if there are many degrees of freedom involved. For instance, a quantum optical system with many spatially separated modes. Here, the system contains photons, which are massless. But they can nevertheless exhibit genuine multipartite

entanglement and hence demonstrate quantum properties. Finally, a system can be massless and have a small number of modes, but contains a very large number of excitations, and be considered in this sense macroscopic (or mesoscopic). A NOON state with large $N$ is an example of this. For a recent review on macroscopic quantum systems, refer to Frowis et al. [32]. In this thesis, we investigate different macroscopic quantum systems that include all of the aspects that are discussed above.

Macroscopic systems can indeed behave quantum mechanically. The reason that we do not have to compute the wavefunction of the universe to predict the behaviour of nature is the observation that the system of interest always interacts with its environment. These interactions can destroy any quantum properties of the system, a mechanism known as the decoherence [33–35]. This is especially so for macroscopic quantum systems where quantum properties of the state are fragile and sensitive to the slightest of disturbance.

Experimentalists have successfully isolated quantum systems from the interactions with its environment and created Schrodinger's cat states in these systems [36–45]. To be sure that cat states are indeed created, it is important to be able to distinguish a cat state from a statistical mixture of distinguishable classical states. There are many proposed measures to signify a cat state such as interference fringes in probability distributions of certain observables [46, 47], negativity of Wigner function [41], and fidelity [39, 48]. However, these measures either do not take into account or can not identify and exclude all the nonideal, but more prevalent cat-like states. For example, some states that admit classical descriptions have high fidelities with respect to a macroscopic superposition state [46]. Similarly, interference fringes do not in itself suffice to exclude all alternative classical description.

In this thesis, we show how to prove unambiguously that multiple different systems are genuinely entangled. We study continuous-variable systems and derive criteria that could be applied to mesoscopic massive systems. We also look at macroscopic quantum coherence, which of course, is the reason why a cat state exists. We consider a quantum coherence test using observables that can be measured in experiments to check for the presence of macroscopic quantum coherence. This test will be shown to neatly relate quantum coherence with a particular quantum fidelity, which is a measure of "closeness" between two quantum states. The ability to compute fidelity is important as it features in many quantum information protocols such as quantum teleportation and quantum state transfer.

It is expected that it is preferable to work with ultracold systems for the creation of large cat states that have mass. More impressively, tangible macroscopic objects in environments with relatively high temperature have been demonstrated to behave quantum mechanically [49–57]. These are the op-

tomechanical systems with nonlinear radiation pressure interaction between its optical and mechanical degrees of freedom. Protocols such as state transfer [58, 59] and quantum entanglement generation [60–62] in an optomechanical system have been realised in different implementations of the system. A major stumbling block in the analyses of the dynamics of these optomechanical systems is that the full quantum mechanical description required resulted in equations that are hard to solve. They are operator equations in the Heisenberg picture, which is intrinsically nonlinear. To complicate the issue further, thermal noises due to the interaction of the system with its environment essentially render these operator equations intractable.

Most analyses in the literature are thus carried out under certain approximations, most notably the linearisation approximation. The validity of this approximation relies on the weak optomechanical coupling strength. For the vast majority of optomechanical experiments, the linearisation approximation has worked well. The cases where the linearisation approximation fails are, however, interesting as nonlinear quantum effects will arise. This is the single-photon strong coupling regime, where a single photon is sufficient to affect the dynamics of the quantum optomechanical system. In this regime, highly nonclassical states such as Fock and Schrodinger's cat states can be generated in the mechanical degree of freedom [63–68]. Other effects that require strong coupling strength include optomechanical induced photon blockade [69], which has been proposed as a quantum simulator of the Bose-Hubbard model, and single-photon generation of entanglement [70]. In this thesis, we present the phase space methods in the truncated Wigner and positive P representations [71–73], where the full dynamics of the optomechanical system can be studied without any approximations. In particular, we look at specific protocols for optomechanical quantum memory and quantum entanglement between two optomechanical systems.

In the optomechanical quantum memory protocol for storage and retrieval of a coherent state, deviations in our numerical results from results within the linearisation approximation were observed. This suggested that the approximation often employed in the literature breaks down even in the weak interaction regime where it is supposed to hold. Power spectral densities reveal large spectral overlap between the control and signal fields, which is not taken into account in calculations with linearisation approximation. Another essential issue in quantum memory is the efficiency of state transfer. In most experiments, it is the power spectral densities that are recorded. From a power spectral density, the energy of the stored state is then inferred. The phase information of the state is, however, lost in this method. A more suitable measure is the quantum fidelity. We discuss the numerical computations of the

fidelity using phase space methods, and determine parameter regimes for which a fidelity is genuinely sufficient for the realisation of a quantum memory.

We continue the investigation of quantum mechanics in macroscopic systems by considering quantum entanglement between two optomechanical systems. The proposal involves well-established techniques in generating entanglement using parametric down-conversion and subsequently transfers the entanglement to two spatially separated optomechanical systems. Using an entanglement criterion, we can determine the experimental parameters and conditions of the environment under which entanglement between the two optomechanical systems is still feasible. It is of interest to generate a long-lived entanglement between the oscillators. This will be useful for quantum network applications and may also provide a way to test the existence of entanglement between spatially separated yet large massive objects. It was conjectured by Furry that such entanglement may be subjected to intrinsic decay [74]. The methods developed for the optomechanical quantum memory to store and retrieve a quantum state using a pulsed optomechanical system are here to be extended to enable storage of entanglement. This provides a way to test alternative quantum mechanical models that include different decoherence mechanisms such as the Furry's hypothesis, where the decoherence could vary with distance.

This thesis is about certifying quantum correlations and studying quantum mechanics in macroscopic systems, which form two parts of this thesis. The first part investigates quantum correlations and criteria to certify these correlations. Other properties of quantum correlations such as monogamy relations of quantum entanglement and also quantum coherence in a quantum state are studied. The second part of the thesis deals with quantum physics in mesoscopic/macroscopic systems. In particular, a quantum optomechanical system is studied where the optical and mechanical degrees of freedom and interactions between them require the quantum mechanical description. Since quantum properties are known to be extremely susceptible to decoherence, we take into account the interactions between the quantum optomechanical system with its environment. Quantum correlations in the quantum optomechanical system are certified using the criteria for quantum correlations of the type presented in Part I of this thesis. Phase space methods in the truncated Wigner and positive P representations are used to simulate two specific protocols for optomechanical quantum memory, and quantum entanglement between two optomechanical systems.

# Part II

# Quantum Correlations and Criteria

# Chapter 1

# Criteria for Genuine Continuous-Variable (CV) Multipartite Entanglement

In this chapter, we investigate quantum correlations in continuous variables (CV) of a quantum optical system. In particular, we devise criteria to certify genuine multipartite entanglement, which is a different notion from a multipartite entanglement. These criteria are derived using the Heisenberg uncertainty principle, which provides bounds for the uncertainties of measurable conjugated observables. A brief description of a squeezed state, which is essential in establishing quantum correlations in subsequent sections, is provided in Section 1.1. In Section 1.2, we describe the specific quantum optical system and its continuous variables, which will be used in the derivations of the criteria in Section 1.3. In Section 1.4, we further discuss these criteria to optimise the verification of quantum correlations in the system. Of course, no physical system is ideal and effects of losses have to be considered. This is explained in Section 1.5. The quantities involved in the criteria derived in this chapter are also useful in investigating certain properties of quantum correlations, such as the monogamy of quantum entanglement. The entanglement monogamy provides insights on the shareability of quantum correlations among different parties in multipartite systems. This chapter is based on the work by Teh and Reid [75] and Rosales-Zárate et al. [76].

## 1.1 Description of the CV quantum states

All information presented in this section should already be familiar to readers with basic knowledge of quantum mechanics and quantum optics. Workers in the field of quantum optics might wish to skip

this section entirely. Extensive details on the description of a quantum state of light can be found in all quantum optics textbooks, and hence only the bare minimum needed for this thesis is presented. We refer readers to standard quantum optics textbooks such as Walls and Milburn [77], and Drummond and Hillery [78]. The purpose of this section is mainly to set the notation that will be used throughout Part I of this thesis.

The standard description of a quantum optical system is used, that is a quantum optical system is modelled as a quantum harmonic oscillator. The quantum harmonic oscillator is most often described in the Heisenberg picture, i.e. the quantum operators involved evolve in time while quantum states are time independent. Everything that can be known about a quantum optical system can be studied using the non-Hermitian creation $\hat{a}_k^\dagger$ and annihilation $\hat{a}_k$ operators. Here, $k$ denotes the different possible light modes. These different modes could have different frequencies or they can have the same frequency but with different polarisations or are spatially separated: they are distinguishable. These operators satisfy the following commutation relation:

$$\left[\hat{a}_k, \hat{a}_{k'}^\dagger\right] = \delta_{k,k'} \,. \tag{1.1}$$

Also, these operators can be defined in terms of Hermitian quadrature operators $\hat{X}$ and $\hat{P}$, in an appropriate rotating frame, as follows:

$$\begin{aligned} \hat{a} &= \frac{1}{2}\left(\hat{X} + i\hat{P}\right) \\ \hat{a}^\dagger &= \frac{1}{2}\left(\hat{X} - i\hat{P}\right) , \end{aligned} \tag{1.2}$$

where $\hat{X}$ and $\hat{P}$ satisfy the commutation relation

$$\left[\hat{X}, \hat{P}\right] = 2i \,. \tag{1.3}$$

The quadratures are quantities that are typically measured in quantum optical experiments with the homodyne detection scheme.

Commutation relations are related to another fundamental notion in quantum physics - the Heisen-

berg uncertainty principle. Mathematically, their relation follows from the inequality

$$\Delta\hat{A}\Delta\hat{B} \geq \left| \frac{\langle [\hat{A},\hat{B}] \rangle}{2i} \right|, \tag{1.4}$$

where $\hat{A}$ and $\hat{B}$ are operators satisfying the commutator $\left[\hat{A},\hat{B}\right]$. Physically, non-commutativity implies uncertainties in measurement outcomes in the corresponding pair of operators/observables. A pair of operators that do not commute is a pair of conjugated operators. Eq. (1.4) says: A pair of conjugated observables cannot be **simultaneously** measured with **arbitrary precision and accuracy**, and the minimal uncertainty achievable is determined by their commutation relation.

Next, we look at how a quantum state of light can be expressed in terms of the creation/annihilation operators and the quadrature operators. In particular, we focus on squeezed states [79, 80] as they will appear throughout the thesis. A squeezed state can be generated by a parametric down-conversion process [81]. As we will see, the parametric down-conversion process not only produces single mode, quantum states of light that are highly nonclassical, but also EPR entangled states [17, 82, 83]. We first consider the degenerate parametric down-conversion process, where an intense pump field is sent into a nonlinear medium, leading to two output fields with frequencies half that of the pump frequency. This process is described by the Hamiltonian, in the interaction picture, as follows:

$$H = i\hbar\frac{\kappa}{2}\left(\hat{a}^\dagger\hat{a}^\dagger e^{i\phi} - \hat{a}\hat{a}e^{-i\phi}\right). \tag{1.5}$$

Here, $\kappa$ is proportional to the pump amplitude, $\phi$ is the pump phase, $\hat{a}$ and $\hat{a}^\dagger$ are the annihilation and creation operators of the output field, respectively. The time evolution of the output mode $\hat{a}$ is obtained from the Heisenberg equation of motion

$$\begin{aligned} \dot{\hat{a}} &= -\frac{i}{\hbar}[\hat{a},H] = \kappa e^{i\phi}\hat{a}^\dagger \\ \dot{\hat{a}}^\dagger &= -\frac{i}{\hbar}\left[\hat{a}^\dagger,H\right] = \kappa e^{-i\phi}\hat{a}. \end{aligned} \tag{1.6}$$

The solutions to the above equations are

$$\begin{aligned} \hat{a}(t) &= \hat{a}(0)\cosh(\kappa t) + \hat{a}^\dagger(0)e^{i\phi}\sinh(\kappa t) \\ \hat{a}^\dagger(t) &= \hat{a}(0)e^{-i\phi}\sinh(\kappa t) + \hat{a}^\dagger(0)\cosh(\kappa t). \end{aligned} \tag{1.7}$$

The squeezing in a squeezed state becomes clear when we look at the time evolution of the corresponding quadrature operators. Choosing, for instance, $\phi = 0$, we get

$$\begin{aligned} \hat{x}(t) &= \mathrm{e}^{\kappa t}\hat{x}(0) \\ \hat{p}(t) &= \mathrm{e}^{-\kappa t}\hat{p}(0)\,. \end{aligned} \tag{1.8}$$

The variance of the $x$-quadrature $\Delta^2[\hat{x}(t)] = \mathrm{e}^{2\kappa t}\Delta^2[\hat{x}(0)]$ increases while the variance of the $p$-quadrature $\left\langle \Delta^2[\hat{p}(t)]\right\rangle = \mathrm{e}^{-2\kappa t}\left\langle \Delta^2[\hat{p}(0)]\right\rangle$ decreases. The uncertainty in the $p$-quadrature is said to be squeezed. One can, of course, choose to squeeze the uncertainty in the $x$-quadrature instead. This is done by choosing $\phi = \pi$. The choice of the pump phase $\phi$ allows squeezing in any arbitrary direction in the quadrature phase space.

There is a more general parametric down-conversion process known as the non-degenerate parametric down-conversion. The setup is identical to the degenerate case, the only difference is the different frequencies in the two output fields. Here, we present the Hamiltonian describing the non-degenerate parametric down-conversion and provide the solutions without explicit calculations. The dynamical solutions of this process reveal that the two output modes are entangled [17]. Indeed, the non-degenerate parametric down-conversion process is used routinely to generate entangled pairs of photons. This process is used in the second part of this thesis where quantum entanglement between two modes is generated. The interaction picture Hamiltonian of the non-degenerate parametric down-conversion is given by

$$H = i\hbar\kappa\left(\hat{a}^\dagger\hat{b}^\dagger\mathrm{e}^{i\phi} - \hat{a}\hat{b}\mathrm{e}^{-i\phi}\right), \tag{1.9}$$

where $\hat{a}$ and $\hat{b}$ are the two output modes with different frequencies. The time evolution of the two output modes are [17]

$$\begin{aligned} \hat{a}(t) &= \hat{a}(0)\cosh\left(\kappa e^{i\phi}t\right) + \hat{b}^\dagger(0)\sinh\left(\kappa e^{i\phi}t\right) \\ \hat{b}(t) &= \hat{b}(0)\cosh\left(\kappa e^{i\phi}t\right) + \hat{a}^\dagger(0)\sinh\left(\kappa e^{i\phi}t\right). \end{aligned} \tag{1.10}$$

The first treatment establishing these solutions as giving the EPR correlations was given by Reid [17]. The correlations are between the different quadratures of these two modes. They are neatly quantified by criterion that involves variances of the form $\Delta^2(X_a - g_x X_b)$ and $\Delta^2(P_a + g_p P_b)$. Explicit calculations

for these expressions can be found, for example, in the paper by Rosales-Zárate et al. [84]. A full review of that analysis and how that treatment enabled the first realisation of continuous-variable (CV) entanglement is given in Reid [17], Reid et al. [82] and Rosales-Zárate et al. [84]. The experimental proposal for the generation of this EPR entangled state was first given by Drummond et al. [83] and realised experimentally by Ou et al. [85].

The corresponding quantum state in the Schrodinger picture can be obtained [86, 87]. Expressing in terms of photon number basis, the quantum state, known as the two-mode squeezed state, is

$$|\psi\rangle = \frac{1}{\cosh(\kappa t)} \sum_{n=0}^{\infty} e^{in\phi} (\tanh \kappa t)^{2n} |n\rangle_a |n\rangle_b . \tag{1.11}$$

It is easy to see from Eq. (1.11) that the photon number of these two modes are highly correlated. For details on how Eq. (1.11) is obtained and some properties of the two-mode squeezed state, readers are referred to [86–88].

With the described quantum model of light, we look at two classes of quantum optical states – the CV GHZ states and CV EPR-type states – in the next section.

## 1.2 CV GHZ states and CV EPR-type states

The quantum state considered by Einstein, Podolski and Rosen in 1935 to elegantly demonstrate the contradiction between local realism and the completeness of quantum mechanics is a continuous-variable (CV) EPR state [5]. Due to the technological limitations at that time, a CV EPR state was not created. The CV EPR states can be created by the nondegenerate parametric down conversion as suggested in Refs. [17, 82] and discussed in the previous section. Alternatively, the EPR states can be created using two degenerate parametric amplifiers and a beam splitter, which was realised in the experiment of Bowen et al. [89]. For a detailed review of the experimental realisations, readers are referred to Ref. [90].

In 1985, Greenberger, Horne and Zeilinger [91] proposed an experiment with a tripartite quantum state involving the spin degree of freedom of spin-$\frac{1}{2}$ particles, now known as the GHZ state. Their arguments lead to a more dramatic prediction from quantum mechanics: a single measurement of the spin values of all three particles along a fixed axis suffices to show the contradiction between quantum mechanics and local realism [92]. The realism in the local realism falls apart: conjugated observables have no predetermined values before they are measured or observed.

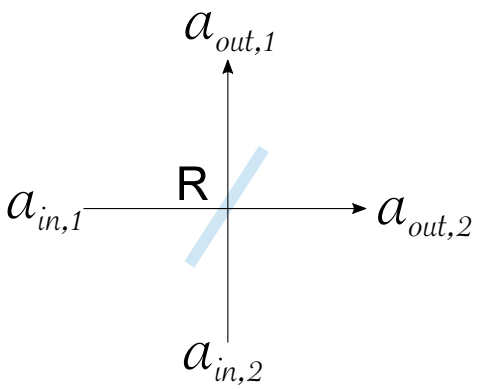


Figure 1.1: The beam splitter with two input modes $a_{in,1}$, $a_{in,2}$ and two output modes $a_{out,1}$, $a_{out,2}$. $R$ is the reflectivity of the beam splitter. The beam splitter operation describing the output modes in terms of the input modes is given in Eq. (1.12).

Paradoxes revealed by both the EPR and GHZ states have profoundly reviewed our intuition on the physical reality; local realism is a universal truth no longer. There are many local hidden variable theories created, attempting to explain away the predictions of quantum mechanics with hidden mechanisms. In the advent of quantum optical tools and techniques, CV EPR and CV GHZ states are now generated routinely. These states hold no hidden mechanisms in their correlations that would be consistent with local hidden states, and we explain how these states are generated in a multi-partite form for a quantum optical system and discuss their properties.

### 1.2.1 Tripartite CV GHZ and CV EPR-type states

The creation of the CV GHZ states in a quantum optical system was first proposed by van Loock et al. [93, 94] and realised in the experiment of Aoki et al. [95]. CV EPR-type states were created in the experiments of Armstrong et al. [96, 97]. The experimental setup required to create these quantum states is simple enough. The exact experimental setups for tripartite CV GHZ and CV EPR states are shown in Figure 1.2 and Figure 1.3, respectively. Both setups involve sending squeezed lights into beam splitters with variable reflectivities. We provide detailed calculations in terms of quantum operators to show the properties of these quantum states. For simplicity, all quantum operators are expressed without the "caret" symbol.

Firstly, we need to establish the operation of a beam splitter, as shown in Fig. 1.1, that is used throughout this thesis. The beam splitter operation is a unitary operation on the incoming light modes

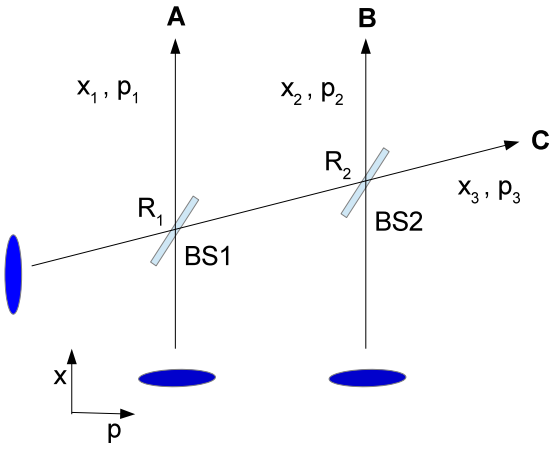


Figure 1.2: Experimental setup for the CV GHZ state generation with squeezed inputs.

and is given by

$$\begin{aligned} a_{out,1} &= \sqrt{R}a_{in,1} + \sqrt{1-R}a_{in,2} \\ a_{out,2} &= \sqrt{1-R}a_{in,1} - \sqrt{R}a_{in,2}\,. \end{aligned} \tag{1.12}$$

Here, $a_{out,1}$, $a_{out,2}$ are the two output modes of a beam splitter, $a_{in,1}$, $a_{in,2}$ are the two input modes into the input ports of a beam splitter and $R$ is the reflectivity of the beam splitter. In this chapter, these mode operators correspond to modes that are distinguishable by their spatial separations.

Using Eq. (1.12), the beam splitter output modes for the configuration in Figure 1.2, in terms of the input modes, are as follows:

$$\begin{aligned} a_1 &= \frac{1}{\sqrt{3}}a_1^{(in)} + \frac{\sqrt{2}}{\sqrt{3}}a_2^{(in)} \\ a_2 &= \frac{1}{\sqrt{3}}a_1^{(in)} - \frac{1}{\sqrt{3}}\frac{1}{\sqrt{2}}a_2^{(in)} + \frac{1}{\sqrt{2}}a_3^{(in)} \\ a_3 &= \frac{1}{\sqrt{3}}a_1^{(in)} - \frac{1}{\sqrt{3}}\frac{1}{\sqrt{2}}a_2^{(in)} - \frac{1}{\sqrt{2}}a_3^{(in)}\,. \end{aligned} \tag{1.13}$$

The input mode $a_1^{(in)}$ is squeezed vacuum in the p-quadrature, while $a_2^{(in)}$ and $a_3^{(in)}$ are squeezed in the x-quadrature.

Expressed in terms of the quadratures, it is easy to show that

$$\begin{aligned} \left\langle x_1 - \frac{(x_2+x_3)}{2} \right\rangle &= \sqrt{\frac{3}{2}} \left\langle x_2^{(in)} \right\rangle \to 0 \\ \langle p_1 + p_2 + p_3 \rangle &= \sqrt{3} \left\langle p_1^{(in)} \right\rangle \to 0 \end{aligned} \tag{1.14}$$

for large squeezing. In the large squeezing limit, Eq. (1.14) implies that the tripartite CV GHZ state is a simultaneous eigenstate of the observable $x_1 - \frac{(x_2+x_3)}{2}$ and the observable $p_1 + p_2 + p_3$. Let us treat, for a moment, $x_i$ and $p_i$ as position and momentum of the $i$-th particle. It is hardly surprising that we are allowed to know, at the same time, the total momentum and some observable involving differences in positions, without any uncertainties. The Heisenberg uncertainty principle, however, is not violated in each mode. The quadratures of each mode still obey

$$\Delta x_i \Delta p_i \geq \left| \frac{\langle [x_i, p_i] \rangle}{2} \right| . \tag{1.15}$$

What is more interesting lies in the correlations between the quadratures in different modes. In the Schrodinger picture [93], a tripartite CV GHZ state is indeed an entangled state in both the $x$ and $p$ basis. However, a classical physics explanation of these correlations cannot be ruled out a priori. The nature of these correlations cannot be determined easily. We address this issue with criteria involving inequalities in Section 1.3.

Next, we go through the same calculation for the CV EPR-type states. As shown in Figure 1.3, only two squeezed vacuum modes are needed rather than three. The input mode $a_1^{(in)}$ is squeezed in the $p$-quadrature, $a_2^{(in)}$ is squeezed in the $x$-quadrature and $a_3^{(in)}$ is a vacuum mode. The output modes are given by

$$\begin{aligned} a_1 &= \frac{1}{\sqrt{2}} \left[ a_1^{(in)} + a_2^{(in)} \right] \\ a_2 &= \frac{1}{2} \left[ a_1^{(in)} - a_2^{(in)} \right] + \frac{1}{\sqrt{2}} a_3^{(in)} \\ a_3 &= \frac{1}{2} \left[ a_1^{(in)} - a_2^{(in)} \right] - \frac{1}{\sqrt{2}} a_3^{(in)} . \end{aligned} \tag{1.16}$$

In the case of CV EPR-type states, the correlations differ slightly from that of a CV GHZ state. Inter-

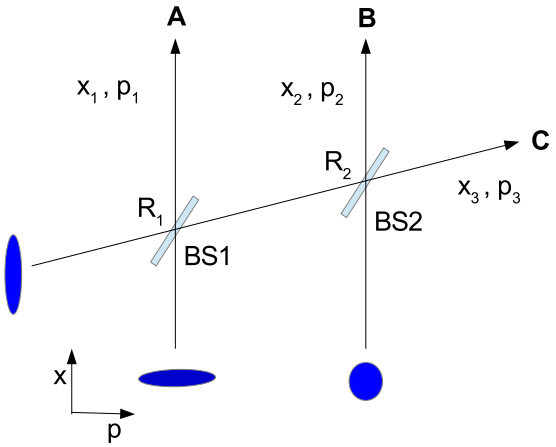


Figure 1.3: Experimental setup for the CV EPR-type state generation with two squeezed input states and a vacuum input at the second beam splitter. .

estingly, correlations between quadratures of different modes exist despite the fact that one of the input modes is vacuum. The correlations are:

$$\begin{aligned} \left\langle x_1 - \frac{(x_2+x_3)}{\sqrt{2}} \right\rangle &= \sqrt{2}\left\langle x_2^{(in)} \right\rangle \to 0 \\ \left\langle p_1 - \frac{(p_2+p_3)}{\sqrt{2}} \right\rangle &= \sqrt{2}\left\langle p_1^{(in)} \right\rangle \to 0\,, \end{aligned} \tag{1.17}$$

for large squeezing.

It is perhaps worth stating the obvious on how Eq. (1.14) and Eq. (1.17) imply correlations in CV GHZ and CV EPR-type states, respectively. For instance, $\left\langle x_1 - \frac{(x_2+x_3)}{\sqrt{2}} \right\rangle = 0$ means that knowing the values of $x_2$ and $x_3$ allow the inference of the value of $x_1$. The inference is possible only if $x_1, x_2$ and $x_3$ are correlated. Once again, the nature of these correlations in Eq. (1.14) and Eq. (1.17) are not known yet, i.e. we cannot say, at this stage, whether these correlations are classical or quantum in nature. This question is dealt with in Section 1.3. Another point is that any inference has uncertainty and it depends on the degree of squeezing, with perfect inference for very large squeezing. It turns out that these uncertainties are the key to understanding quantum correlations. Indeed, we shall see that the uncertainties in these inferences determine the nature of the correlation of a given physical state.

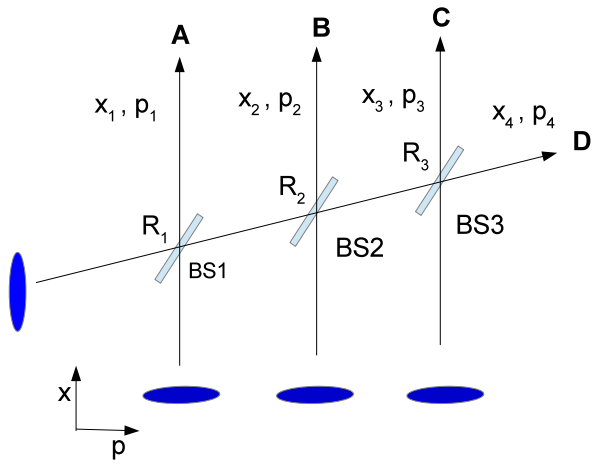


Figure 1.4: Schematic of the generation of a 4-partite CV GHZ state.

### 1.2.2 *N*-partite CV GHZ and CV EPR-type states

The tripartite setups in Fig. 1.2 and Fig. 1.3 are easily generalized to $N$-partite: one simply adds more beam splitters and squeezed input lights.

The $N$-partite CV GHZ state is generated using one squeezed input state and $N-1$ orthogonally squeezed input states with $N-1$ beam splitters. The reflectivities of these beam splitters are chosen such that $R_n = \frac{1}{N+1-n}$, where $n = 1,2,...,N-1$. We provide here the explicit calculation for the 4-partite case to show the correlations among the different parties/modes. The experimental setup for 4-partite CV GHZ state is shown in Fig. 1.4. The optical output mode operators are

$$
\begin{aligned}
a_1 &= \sqrt{\frac{1}{4}}a_1^{(in)} + \sqrt{\frac{3}{4}}a_2^{(in)} \\
a_2 &= \sqrt{\frac{1}{4}}a_1^{(in)} - \sqrt{\frac{1}{4}}\sqrt{\frac{1}{3}}a_2^{(in)} + \sqrt{\frac{2}{3}}a_3^{(in)} \\
a_3 &= \sqrt{\frac{1}{4}}a_1^{(in)} - \sqrt{\frac{1}{4}}\sqrt{\frac{2}{3}}\sqrt{\frac{1}{2}}a_2^{(in)} - \sqrt{\frac{1}{3}}\sqrt{\frac{1}{2}}a_3^{(in)} + \sqrt{\frac{1}{2}}a_4^{(in)} \\
a_4 &= \sqrt{\frac{1}{4}}a_1^{(in)} - \sqrt{\frac{1}{4}}\sqrt{\frac{2}{3}}\sqrt{\frac{1}{2}}a_2^{(in)} - \sqrt{\frac{1}{3}}\sqrt{\frac{1}{2}}a_3^{(in)} - \sqrt{\frac{1}{2}}a_4^{(in)} .
\end{aligned}
\tag{1.18}
$$

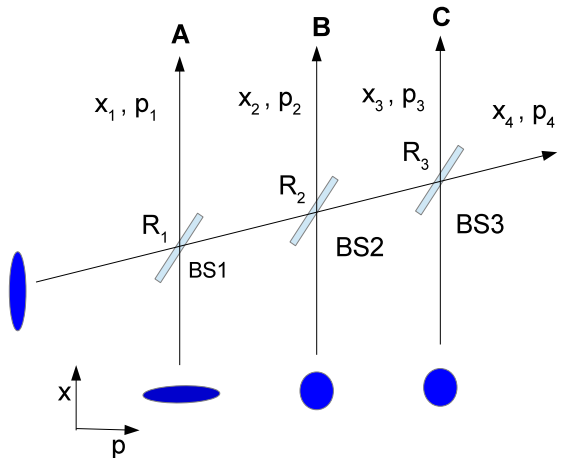


Figure 1.5: Schematic of the generation of an asymmetric 4-partite EPR-type state $I$.

Again, in terms of the quadratures, the correlations are

$$\begin{aligned} \left\langle x_1 - \frac{(x_2+x_3+x_4)}{3} \right\rangle &= \sqrt{\frac{4}{3}} \left\langle x_2^{(in)} \right\rangle \to 0 \\ \langle p_1 + (p_2+p_3+p_4) \rangle &= \sqrt{4} \left\langle p_1^{(in)} \right\rangle \to 0\,, \end{aligned} \tag{1.19}$$

for large squeezing.

In contrast, the $N$-partite EPR-type state is generated using two orthogonally squeezed input states and $N-2$ vacuum inputs with $N-1$ beam splitters. Even though only two squeezed input states are needed for this case, correlations exist in this class of states. One might jump to the conclusion that $N$-partite CV EPR states are better: only two squeezed inputs are required while the rest are merely vacuum modes. It might be easier to generate the $N$-partite CV EPR states than the $N$-partite CV GHZ states. But the amount of quantum correlation in these states is yet to be quantified in this thesis. It might well be that CV EPR states contain less correlations than the CV GHZ states. We know that quantum correlations are resources in quantum computations and the greater, the better. Hence, measures that quantify quantum correlations are pivotal. Criteria derived in the next section shed light on this issue.

Back to the CV EPR-type states, depending on the experimental setup, two different subtypes

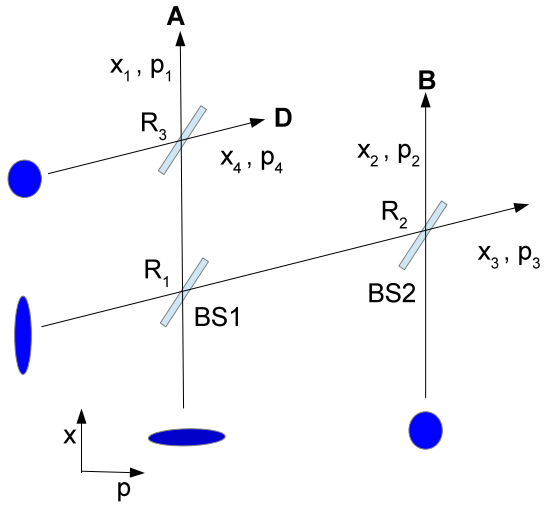


Figure 1.6: Schematic of the generation of a symmetric 4-partite EPR-type state *II*.

of states can be generated. We label them as the asymmetric EPR-type state *I* and the symmetric EPR-type state *II*. These states are generated in experimental setups as shown in Fig. 1.5 and Fig. 1.6, respectively. The reflectivities of the beam splitters in these experimental setups are specifically chosen. For asymmetric EPR-type state *I*, the sequence of beam splitters have reflectivities $R_1 = \frac{1}{2}$ and $R_n = \frac{1}{N-n+1}$, where $N$ is the total number of modes and $n = 2,3,...,N$.

On the other hand, the beam splitter reflectivities for generating the symmetric EPR-type state *II* can only be expressed clearly after setting the notation used for each mode, which we present now. Following Fig. 1.6, there are $\left(\frac{N}{2}-1\right)$ beam splitters to the right of the first beam splitter BS1 and $\left(\frac{N}{2}-1\right)$ beam splitters to the left of the first beam splitter BS1, where $N$ is the total number of modes. Note that the number of beam splitters to the right and left of the first beam splitter BS1 are the same, hence the choice of the name symmetric EPR-type state *II*. The reflectivity of the first beam splitter BS1 is always $\frac{1}{2}$. The reflectivities of beam splitters to the right of BS1 are labeled as $R_n$, where $n = 2,3,...,\frac{N}{2}$ and it is given by $R_n = \frac{1}{\frac{N}{2}-n+2}$; while the reflectivities of beam splitters to the left of BS1 are labeled as $R_{n+\frac{N}{2}-1}$, where $n = 2,3,...,\frac{N}{2}$ and $R_{n+\frac{N}{2}-1} = R_n$. Experimental details on how an asymmetric EPR-type state *II* is generated and measured can be found in the paper by Armstrong et al. [96].

In the following, we express the output modes for both the asymmetric EPR-type state *I* and the

symmetric EPR-type state *II*. For the asymmetric EPR-type state *I*, the output modes are

$$\begin{aligned}
a_1 &= \frac{1}{\sqrt{2}}a_1^{(in)} + \frac{1}{\sqrt{2}}a_2^{(in)} \\
a_2 &= \frac{1}{\sqrt{6}}a_1^{(in)} - \frac{1}{\sqrt{6}}a_2^{(in)} + \sqrt{\frac{2}{3}}a_3^{(in)} \\
a_3 &= \frac{1}{\sqrt{6}}a_1^{(in)} - \frac{1}{\sqrt{6}}a_2^{(in)} - \sqrt{\frac{1}{6}}a_3^{(in)} + \sqrt{\frac{1}{2}}a_4^{(in)} \\
a_4 &= \frac{1}{\sqrt{6}}a_1^{(in)} - \frac{1}{\sqrt{6}}a_2^{(in)} - \sqrt{\frac{1}{6}}a_3^{(in)} - \sqrt{\frac{1}{2}}a_4^{(in)} .
\end{aligned} \tag{1.20}$$

The corresponding correlations in quadratures can then be shown to be

$$\begin{aligned}
\langle x_1 - \frac{1}{\sqrt{3}}(x_2 + x_3 + x_4)\rangle &= \sqrt{2}\langle x_2^{(in)}\rangle \to 0 \\
\langle p_1 + \frac{1}{\sqrt{3}}(p_2 + p_3 + p_4)\rangle &= \sqrt{2}\langle p_1^{(in)}\rangle \to 0 ,
\end{aligned} \tag{1.21}$$

for large squeezing. Similarly, the output modes for the symmetric EPR-type state *II* are

$$\begin{aligned}
a_1 &= \frac{1}{2}a_1^{(in)} + \frac{1}{2}a_2^{(in)} + \sqrt{\frac{1}{2}}a_4^{(in)} \\
a_2 &= \frac{1}{2}a_1^{(in)} - \frac{1}{2}a_2^{(in)} + \sqrt{\frac{1}{2}}a_3^{(in)} \\
a_3 &= \frac{1}{2}a_1^{(in)} - \frac{1}{2}a_2^{(in)} - \sqrt{\frac{1}{2}}a_3^{(in)} \\
a_4 &= -\frac{1}{2}a_1^{(in)} - \frac{1}{2}a_2^{(in)} + \sqrt{\frac{1}{2}}a_4^{(in)} ,
\end{aligned} \tag{1.22}$$

with correlations in the quadratures

$$\begin{aligned}
\langle x_1 - (x_2 + x_3 + x_4)\rangle &= 2\langle x_2^{(in)}\rangle \to 0 \\
\langle p_1 + (p_2 + p_3 - p_4)\rangle &= 2\langle p_1^{(in)}\rangle \to 0 ,
\end{aligned} \tag{1.23}$$

for large squeezing.

In the next section, we derive criteria to check for genuine multipartite quantum entanglement. These criteria are based on the statistics of continuous quadrature amplitudes that are described in this

section. We apply these criteria to the CV GHZ states and CV EPR-type states and demonstrate the existence of genuine multipartite quantum entanglement in these states.

## 1.3 Criteria for Genuine Multipartite Quantum Correlations

We address two fundamental issues in this section. The first issue: Given a quantum state, what is the nature of its correlations (if any)? This leads to the second issue: How do we quantify quantum correlations?

We derive criteria to check for genuine multipartite quantum entanglement for the continuous-variable quantum optical systems described in Section 1.2. The genuine multipartite entanglement is first defined and based on this definition, the corresponding criteria are derived.

### 1.3.1 Full tripartite inseparability and genuine tripartite entanglement

In order to understand and define what we mean by multipartite quantum entanglement, we start from the standard definition of a bipartite quantum entangled state and try to extend this to the multipartite case. For clarity and generality, density operators are used. A bipartite entangled state cannot be expressed as product states of the two parties. A state that can be expressed as product states of all the parties involved is called a separable state:

$$\rho = \sum_i P_i \rho_A^i \rho_B^i \,, \tag{1.24}$$

where $\rho_A^i$ and $\rho_B^i$ are density operators that correspond to quantum states of party $A$ and $B$, respectively, and $P_i$ is the probability for the system to be in the state $\rho_A^i \rho_B^i$. To be mathematically precise, the sum in Eq. (1.24) is a convex linear combination/sum of separable states $\rho_A^i \rho_B^i$. Physically, Eq. (1.24) means that the state is a statistical mixture of states $\rho_A^i \rho_B^i$. A quantum state is bipartite entangled if it cannot be expressed as a separable state. Since a density operator encodes all statistics of a given physical state, the definition of bipartite quantum entanglement here is equivalent to the definition given in terms of joint probability distributions in Section 0.1.

It is straightforward to extend the definition in Eq. (1.24) of a bipartite entangled state to a tripartite entangled state. To this end, a tripartite state is tripartite entangled if it cannot be expressed as a

separable state, i.e.

$$\rho \neq \sum_i P_i \rho_A^i \rho_B^i \rho_C^i \,. \tag{1.25}$$

A counter-example suffices to demonstrate the inadequacy of the definition given in Eq. (1.25). We consider a tripartite state that contains a pair of entangled parties and a party that is not correlated to them. The tripartite system is, for instance, in the state $\rho = \rho_A \rho_{BC}$; a product state of party $A$, $\rho_A$ and bipartite entangled state $\rho_{BC}$. A product state such as this is called a biseparable state. Even though this state $\rho$ satisfies Eq. (1.25), it cannot be a tripartite entangled state as it is obviously biseparable. The state contains quantum entanglement but the entanglement is not shared among all three parties. It is clear from this counter-example that all possible biseparable states have to be negated for a tripartite entangled state. In the following, we define the notion of tripartite inseparability. A tripartite state is **full tripartite inseparable** if the state cannot be expressed in any of the following set of tripartite states:

$$\begin{aligned}
\rho &= \sum_i \eta_i \rho_{12}^i \rho_3^i \\
\rho &= \sum_i \eta_i \rho_{13}^i \rho_2^i \\
\rho &= \sum_i \eta_i \rho_{23}^i \rho_1^i \\
\rho &= \sum_i \eta_i \rho_1^i \rho_2^i \rho_3^i \,.
\end{aligned} \tag{1.26}$$

In other words, a full tripartite inseparable state cannot be expressed as product states of the three-party system and as any one of the biseparable states. The full tripartite inseparability was used in some works as the definition of tripartite entanglement. It turns out that the above set of tripartite states does not encompass all possible states to demonstrate that quantum entanglement is indeed shared among all three parties. For instance, the state $\rho = \frac{1}{2}\rho_{12}\rho_3 + \frac{1}{2}\rho_{23}\rho_1$ cannot be expressed in any of the tripartite states listed in Eq. (1.26). However, it is a statistical mixture of biseparable states $\rho_{12}\rho_3$ and $\rho_{23}\rho_1$, and hence the state cannot be tripartite entangled. We see from this example that for a tripartite state to be entangled, full tripartite inseparability is necessary, but not sufficient. It is clear as to why full tripartite inseparability is not sufficient as mixed states are not considered in the set of states given in Eq. (1.26).

This leads to the definition of **genuine tripartite quantum entanglement**. In order to be sure that

quantum entanglement is shared among all parties, we have to rule out the possibility that the state is in (1) any of the possible biseparable states and (2) any statistical mixture of all possible biseparable states. Mathematically, a genuine tripartite entangled state cannot be expressed as

$$\rho_{BS} = P_1 \sum_R \eta_R^{(1)} \rho_{1,Q}^R \rho_{23,Q}^R + P_2 \sum_{R'} \eta_{R'}^{(2)} \rho_{2,Q}^{R'} \rho_{13,Q}^{R'} + P_3 \sum_{R''} \eta_{R''}^{(3)} \rho_{3,Q}^{R''} \rho_{12,Q}^{R''}. \tag{1.27}$$

Here, $R$,$R'$ and $R''$ differentiate between different bipartitions and the subscript $Q$ in $\rho_Q$ denotes a quantum density operator.

This definition is more general and harder to show than the full tripartite inseparability as the latter excludes only each individual bipartition but not mixtures of them. Hence, the two different definitions of tripartite quantum entanglement mean different things but they have been used interchangeably in the literature. The genuine tripartite entanglement and full tripartite inseparability coincide for pure quantum states but not for mixed states.

### 1.3.2 Full multipartite inseparability criteria

Before deriving the criteria for genuine multipartite entanglement in quantum optical systems, it is instructive to look at criteria for full multipartite inseparability. They tell us what observables we should measure and what to expect of the outcomes of these observables should the correlations in the system be classical in nature.

Van Loock and Furusawa first derived criteria based on the definition of full multipartite inseparability, the violation of which imply full multipartite inseparability. In this section, we only list down the criteria and discuss their general features. For a three-party system, Van Loock and Furusawa consider a set of three inequalities [1]

$$\begin{aligned} B_I &\equiv [\Delta(x_1 - x_2)]^2 + [\Delta(p_1 + p_2 + g_3 p_3)]^2 \geq 4, \\ B_{II} &\equiv [\Delta(x_2 - x_3)]^2 + [\Delta(g_1 p_1 + p_2 + p_3)]^2 \geq 4, \\ B_{III} &\equiv [\Delta(x_1 - x_3)]^2 + [\Delta(p_1 + g_2 p_2 + p_3)]^2 \geq 4, \end{aligned} \tag{1.28}$$

which are defined for arbitrary real parameters $g_1$, $g_2$, and $g_3$. They show that the inequality $B_I \geq 4$ in Eq. (1.28) is satisfied by both the biseparable states $\rho_{13,2}$ and $\rho_{23,1}$, which implies that modes 1 and 2 are separable. Similarly, the second inequality $B_{II} \geq 4$ is satisfied by the biseparable states $\rho_{13,2}$

and $\rho_{12,3}$, while the third inequality $B_{III} \geq 4$ is satisfied by the biseparable states $\rho_{12,3}$ and $\rho_{23,1}$. It follows that the violation of any two of the inequalities in Eq. (1.28) is sufficient to negate any of the biseparable states $\rho_{12,3}$, $\rho_{13,2}$, or $\rho_{23,1}$. The state is then a "*fully inseparable tripartite entangled state*".

Let's discuss the features of these inequalities given in Eq. (1.28). They consist of uncertainties in observables, where these observables are linear combinations of quadratures from different modes. The uncertainties of these observables satisfy certain lower bounds if we assume these uncertainties arise from certain class of correlation. In other words, these bounds are answers to the question: How big should these uncertainties be if these outcomes are due to states that belong to a certain class of correlation? Perhaps an example will clear up any potential confusions. We consider the quantity $\Delta\left[x_1 - \frac{(x_2+x_3)}{2}\right]\Delta[p_1+p_2+p_3]$. Suppose that we found the lower bound for which this quantity has to satisfy if the state is tripartite separable, and the bound is a nonzero number $c$. This means that any number which is smaller than $c$ violates the assumption used to derive the bound, which is that the state is tripartite separable. We have seen, for example, that a CV GHZ state for large squeezing has the following properties as given in Eq. (1.14):

$$\left\langle x_1 - \frac{(x_2+x_3)}{2} \right\rangle = \sqrt{\frac{3}{2}} \left\langle x_2^{(in)} \right\rangle \to 0$$
$$\langle p_1 + p_2 + p_3 \rangle = \sqrt{3} \left\langle p_1^{(in)} \right\rangle \to 0\,.$$

The quantity $\Delta\left[x_1 - \frac{(x_2+x_3)}{2}\right]\Delta[p_1+p_2+p_3]$ is smaller than $c$ and CV GHZ state is tripartite inseparable.

As discussed in section 1.3.1, fully inseparable tripartite entangled state is not enough to show that entanglement is really being shared among all three parties, as the system can be in a mixture of different biseparable states and yet violate any two of the inequalities of Eq. (1.28). However, we can still use the same logic and techniques used here to derive criteria for the genuine tripartite entanglement. This is presented in the next section.

For completeness, there is a product version of the van Loock-Furusawa inequalities given in Eq.

(1.28):

$$\begin{aligned} S_I &\equiv \Delta(x_1 - x_2)\Delta(p_1 + p_2 + g_3 p_3) \geq 2, \\ S_{II} &\equiv \Delta(x_2 - x_3)\Delta(g_1 p_1 + p_2 + p_3) \geq 2, \\ S_{III} &\equiv \Delta(x_1 - x_3)\Delta(p_1 + g_2 p_2 + p_3) \geq 2. \end{aligned} \tag{1.29}$$

They work the same way as the sum version in Eq. (1.28), where a violation of any two of the inequalities in Eq. (1.29) is sufficient to negate any of the biseparable states $\rho_{12,3}$, $\rho_{13,2}$, or $\rho_{23,1}$. Having said that, a product criterion always implies the sum criterion [75]. This can be seen with the simple identity $x^2 + y^2 \geq 2xy$, which holds for any real numbers $x$ and $y$. From this, the violation of a sum inequality automatically implies the violation of a product inequality. The violation of a product inequality, however, does not imply the violation of a sum inequality. In this sense, a product inequality is a better criterion in the verification of quantum correlations.

We see from these criteria that we have to first choose a set of linear combinations of quadratures from different modes and look at their uncertainties. The bounds for these uncertainties are then derived by assuming the nature of the states, depending on the class of quantum correlation we are investigating.

### 1.3.3 Genuine multipartite entanglement criteria

The criteria listed in the previous section consist of a set of inequalities. It is also possible to devise criteria using only a single inequality and the derivations of criteria in this thesis belong to this class.

We now derive criteria for genuine multipartite entanglement, which rule out the possibility that a given state is in a mixture of different biseparable quantum states. For simplicity, the criteria for genuine tripartite entanglement are first derived. Derivation of genuine multipartite entanglement criteria in the same fashion will be presented later.

Recall the definition of genuine tripartite entanglement as impossibility of the state to be expressed in the form given by Eq. (1.27):

$$\rho_{BS} = P_1 \sum_R \eta_R^{(1)} \rho_{1,Q}^R \rho_{23,Q}^R + P_2 \sum_{R'} \eta_{R'}^{(2)} \rho_{2,Q}^{R'} \rho_{13,Q}^{R'} + P_3 \sum_{R''} \eta_{R''}^{(3)} \rho_{3,Q}^{R''} \rho_{12,Q}^{R''}.$$

We reiterate the line of reasoning behind the derivation. Firstly, assume that the statistics of the

measured outcomes are due to a state that can be expressed in the form in Eq. (1.27). Based on this definition, find the corresponding inequality or bound that the statistics must satisfy. The violation of the inequality implies false assumption and that the statistics corresponds to that of a genuine tripartite entangled state. The quantities that are measured in a quantum optical system in this thesis are the continuous-variable quadrature amplitudes $x_i, p_i$ and the quantities that we would like to have in our criteria have the following form:

$$\begin{aligned}(\Delta u)^2 &= \left[\Delta\left(h_1x_1 + h_2x_2 + ... + h_nx_n\right)^2\right] \\ (\Delta v)^2 &= \left[\Delta\left(g_1p_1 + g_2p_2 + ... + g_np_n\right)^2\right], \end{aligned} \tag{1.30}$$

where $(\Delta u)^2$ and $(\Delta v)^2$ are the variances of $u$ and $v$, respectively. $x_i$ and $p_i$ are complementary/conjugated observables of the mode $i$ and they do not commute. The coefficients $h_1,...,h_n;g_1,...,g_n$ can be optimized depending on the state and they give us information about the correlations between quadrature amplitudes of different parties/modes for that state. The criteria will involve the sum or product of these quantities $(\Delta u)^2$ and $(\Delta v)^2$.

#### 1.3.3.1 Tripartite case

The task is to derive bound for the quantity $(\Delta u)^2 + (\Delta v)^2$ such that the violation of the bound implies genuine multipartite quantum entanglement. The derivation is lengthy but essential in demonstrating the concepts and logic involved so we include them in this section. Bounds for different quantities and also for the general $N$-partite case are derived using the same techniques.

Now, we present the derivation of the lower bound for $(\Delta u)^2 + (\Delta v)^2$ in the tripartite case, assuming that the state is a biseparable mixture state $\rho_{BS} = P_1 \sum_R \eta_R^{(1)} \rho_1^R \rho_{23}^R + P_2 \sum_{R'} \eta_{R'}^{(2)} \rho_2^{R'} \rho_{13}^{R'} + P_3 \sum_{R''} \eta_{R''}^{(3)} \rho_3^{R''} \rho_{12}^{R''}$, as given in Eq. (1.27). We dropped the subscript $Q$ to simplify the notation, but all density operators here are quantum density operators. Suppose that the statistics for $u$ and $v$ arise from the biseparable mixture state $\rho_{BS}$ and using the Cauchy-Schwarz inequality, we obtain

$$\triangle^2 u \geq P_1 \sum \eta_R^{(1)} \Delta^2 u_R + P_2 \sum \eta_{R'}^{(2)} \Delta^2 u_{R'} + P_3 \sum \eta_{R''}^{(3)} \Delta^2 u_{R''} \tag{1.31}$$

and

$$\triangle^2 v \geq P_1 \sum \eta_R^{(1)} \Delta^2 v_R + P_2 \sum \eta_{R'}^{(2)} \Delta^2 v_{R'} + P_3 \sum \eta_{R''}^{(3)} \Delta^2 v_{R''} \,. \tag{1.32}$$

Here, $\Delta^2 u_R$ is the variance of $h_1 x_1 + h_2 x_2 + h_3 x_3$ for the state $\rho_1^R \rho_{23}^R$, $\Delta^2 u_{R'}$ is the variance of $h_1 x_1 + h_2 x_2 + h_3 x_3$ for the state $\rho_2^{R'} \rho_{13}^{R'}$ and $\Delta^2 u_{R''}$ is the variance of $h_1 x_1 + h_2 x_2 + h_3 x_3$ for the state $\rho_3^{R''} \rho_{12}^{R''}$. Similarly, $\Delta^2 v_R$, $\Delta^2 v_{R'}$ and $\Delta^2 v_{R''}$ are variances of $g_1 p_1 + g_2 p_2 + g_3 p_3$ for the states $\rho_1^R \rho_{23}^R$, $\rho_2^{R'} \rho_{13}^{R'}$ and $\rho_3^{R''} \rho_{12}^{R''}$, respectively. From Eq. (1.31) and Eq. (1.32), their sum satisfies

$$\begin{aligned}(\Delta u)^2 + (\triangle v)^2 \geq\; & P_1 \sum \eta_R^{(1)} \left[ (\Delta u_R)^2 + (\Delta v_R)^2 \right] + P_2 \sum \eta_{R'}^{(2)} \left[ (\Delta u_{R'})^2 + (\Delta v_{R'})^2 \right] \\ & + P_3 \sum \eta_{R''}^{(3)} \left[ (\Delta u_{R''})^2 + (\Delta v_{R''})^2 \right] .\end{aligned} \tag{1.33}$$

Next, we find the bounds for each of the individual terms $\left[ (\Delta u_R)^2 + (\Delta v_R)^2 \right]$, $\left[ (\Delta u_{R'})^2 + (\Delta v_{R'})^2 \right]$ and $\left[ (\Delta u_{R''})^2 + (\Delta v_{R''})^2 \right]$ in the above inequality (1.33). We do that by deriving the inequality satisfied by $\left(\Delta u_\xi\right)^2 + \left(\Delta v_\xi\right)^2$ that corresponds to an arbitrary bipartition $\rho_{km}^\xi \rho_n^\xi$. The variances of $u_\xi$ and $v_\xi$ are

$$\begin{aligned}\left(\Delta u_\xi\right)^2 &= [\Delta(h_n x_n)]^2 + [\Delta(h_k x_k)]^2 + [\Delta(h_m x_m)]^2 + 2 h_k h_m (\langle x_k x_m \rangle - \langle x_k \rangle \langle x_m \rangle) \\ &= [\Delta(h_n x_n)]^2 + [\Delta(h_k x_k + h_m x_m)]^2 \end{aligned} \tag{1.34}$$

and

$$\begin{aligned}\left(\Delta v_\xi\right)^2 &= [\Delta(g_n p_n)]^2 + [\Delta(g_k p_k)]^2 + [\Delta(g_m p_m)]^2 + 2 g_k g_m (\langle p_k p_m \rangle - \langle p_k \rangle \langle p_m \rangle) \\ &= [\Delta(g_n p_n)]^2 + [\Delta(g_k p_k + g_m p_m)]^2 \,. \end{aligned} \tag{1.35}$$

From Eqs. (1.34) and (1.35), $\left(\Delta u_\xi\right)^2 + \left(\Delta v_\xi\right)^2$ has the lower bound:

$$\begin{aligned}\left(\Delta u_\xi\right)^2 + \left(\Delta v_\xi\right)^2 &= [\Delta(h_n x_n)]^2 + [\Delta(g_n p_n)]^2 + [\Delta(h_k x_k + h_m x_m)]^2 + [\Delta(g_k p_k + g_m p_m)]^2 \\ &\geq |h_n g_n| \frac{[x_n, p_n]}{2} + |h_k g_k \frac{[x_k, p_k]}{2} + h_m g_m \frac{[x_m, p_m]}{2}| \\ &= |h_n g_n| + |h_k g_k + h_m g_m| \,. \end{aligned} \tag{1.36}$$

The Heisenberg uncertainty principle is employed going from the first to second line.

With the above inequality in Eq. (1.36), we consider each bipartition separately. For the bipartition $\rho_1\rho_{23}$, we have $\left[(\Delta u_R)^2+(\Delta v_R)^2\right] \geq |h_1g_1|+|h_2g_2+h_3g_3|$ . Similarly, for the bipartition $\rho_2\rho_{13}$, $\left[(\Delta u_{R'})^2+(\Delta v_{R'})^2\right] \geq |h_2g_2|+|h_1g_1+h_3g_3|$ and $\left[(\Delta u_{R''})^2+(\Delta v_{R''})^2\right] \geq |h_3g_3|+|h_1g_1+h_2g_2|$ for the bipartition $\rho_3\rho_{12}$. Thus, Eq. (1.33) becomes

$$\begin{aligned}
(\Delta u)^2+(\triangle v)^2 &\geq P_1\sum\eta_R^{(1)}\left[(\Delta u_R)^2+(\Delta v_R)^2\right]+P_2\sum\eta_{R'}^{(2)}\left[(\Delta u_{R'})^2+(\Delta v_{R'})^2\right] \\
&\quad +P_3\sum\eta_{R''}^{(3)}\left[(\Delta u_{R''})^2+(\Delta v_{R''})^2\right] \\
&\geq P_1\sum_R\eta_R^{(1)}\left(|h_1g_1|+|h_2g_2+h_3g_3|\right)+P_2\sum_{R'}\eta_{R'}^{(2)}\left(|h_2g_2|+|h_1g_1+h_3g_3|\right) \\
&\quad +P_3\sum_{R''}\eta_{R''}^{(3)}\left(|h_3g_3|+|h_1g_1+h_2g_2|\right) \\
&\geq \min\left\{|h_1g_1|+|h_2g_2+h_3g_3|,|h_2g_2|+|h_1g_1+h_3g_3|,|h_3g_3|+|h_1g_1+h_2g_2|\right\} .
\end{aligned} \tag{1.37}$$

The violation of the inequality (1.37) implies genuine tripartite entanglement. Following the same idea, we derive a set of genuine tripartite entanglement criteria. For instance, the product criterion is given by

$$\Delta u\Delta v \geq \min\left\{|h_1g_1|+|h_2g_2+h_3g_3|,|h_2g_2|+|h_1g_1+h_3g_3|,|h_3g_3|+|h_1g_1+h_2g_2|\right\} . \tag{1.38}$$

In the following, we list down the criteria that are used in this thesis to certify genuine tripartite entanglement in continuous-variable quantum optical systems. These criteria are derived using the same approach just presented. More details can be found in Teh and Reid [75].

**Criterion (1) :** The violation of inequality

$$B_I+B_{II}+B_{III} \geq 8 \tag{1.39}$$

is sufficient to confirm genuine tripartite entanglement, where $B_I$, $B_{II}$ and $B_{III}$ are defined in Eq. (1.28).

**Criterion (2) :** The violation of inequality

$$S_I + S_{II} + S_{III} \geq 4 \tag{1.40}$$

is sufficient to confirm genuine tripartite entanglement, where $S_I$, $S_{II}$ and $S_{III}$ are defined in Eq. (1.29).

**Criterion (3) :** The violation of inequality

$$\left[\Delta\left(x_1 - \frac{(x_2+x_3)}{\sqrt{2}}\right)\right]^2 + \left[\Delta\left(p_1 + \frac{(p_2+p_3)}{\sqrt{2}}\right)\right]^2 \geq 2 \tag{1.41}$$

is sufficient to confirm genuine tripartite entanglement.

**Criterion (4) :** The violation of inequality

$$\left[\Delta\left(x_1 - \frac{(x_2+x_3)}{\sqrt{2}}\right)\right]\left[\Delta\left(p_1 + \frac{(p_2+p_3)}{\sqrt{2}}\right)\right] \geq 1 \tag{1.42}$$

is sufficient to confirm genuine tripartite entanglement.

**Criterion (5) :** The following generalized criterion is derived above.

$$(\Delta u)^2 + (\triangle v)^2 \geq \min\left\{|h_1 g_1| + |h_2 g_2 + h_3 g_3|, |h_2 g_2| + |h_1 g_1 + h_3 g_3|, |h_3 g_3| + |h_1 g_1 + h_2 g_2|\right\}. \tag{1.43}$$

The violation of which confirms genuine tripartite entanglement.

**Criterion (6) :** This generalized criterion is derived above.

$$\Delta u \Delta v \geq \min\left\{|h_1 g_1| + |h_2 g_2 + h_3 g_3|, |h_2 g_2| + |h_1 g_1 + h_3 g_3|, |h_3 g_3| + |h_1 g_1 + h_2 g_2|\right\}. \tag{1.44}$$

The violation of which confirms genuine tripartite entanglement. This criterion is stronger than Criterion (5) as the violation of this criterion implies the violation of criterion (5). As described in the previous section, this can be seen with the simple identity $x^2 + y^2 \geq 2xy$, which holds for any real numbers $x$ and $y$.

**Criterion (7) :** Using Eq. (1.28), there is genuine tripartite entanglement if

$$\tilde{B}_I + \tilde{B}_{II} \geq 4 \tag{1.45}$$

(or $\tilde{B}_I + \tilde{B}_{III} \geq 4$, or $\tilde{B}_{II} + \tilde{B}_{III} \geq 4$) is violated. Here, $\tilde{B}_I$, $\tilde{B}_{II}$ and $\tilde{B}_{III}$ have the same expressions as those in Eq. (1.28) but with $g_1 = g_2 = g_3 = 1$.

The criteria listed above allow quantum correlations to be quantified. These criteria are sufficient, but not necessary in showing genuine tripartite entanglement. What this means is that the violation of a criterion is **sufficient** to demonstrate genuine tripartite quantum entanglement. On the other hand, not violating a criterion does not **necessarily** imply the absence of genuine tripartite quantum entanglement. For instance, Criteria (3) and (4) are designed to check for genuine tripartite entanglement of EPR-type states. The CV GHZ state might not violate these criteria. However, not violating these criteria does not necessarily mean that the CV GHZ state is not genuinely tripartite entangled. This is true for all the criteria for all different classes of quantum correlations that we derive.

We point out another feature of these criteria. When these criteria are violated, the degree of violation, i.e. how different the value is from the bound, quantifies the amount of quantum multipartite EPR-type correlations. In other words, these criteria are "measures" that quantify quantum correlations in a given quantum state, in the sense of EPR where one makes predictions at one location based on measurements at another. As described before, the ability to quantify quantum correlations is essential in quantum information and computing protocols. For instance, the fidelity, which measures how "close" the output state with respect to a quantum input state, in a quantum teleportation scheme depends on the amount of quantum correlations as the resource shared between two parties [27].

#### 1.3.3.2 Multipartite case

We use the method in Section 1.3.3.1 for three parties to arbitrary $N$ parties. Recall, from the derivation of the tripartite sum inequality in Eq. (1.36), that for an arbitrary bipartition $\rho^{\xi}_{km}\rho^{\xi}_{n}$, the sum inequality is given by $\left(\Delta u_\xi\right)^2 + \left(\Delta v_\xi\right)^2 \geq |h_n g_n| + |h_k g_k + h_m g_m|$. The right side of the inequality is a sum of two terms: the absolute value of the gain coefficients for all the parties in one partition and the absolute value of the gain coefficients for all the parties in another partition. For a general $N$-partite system, we first identify all possible bipartitions and then write down their corresponding inequalities. This is described explicitly in Criterion (8) below:

**Criterion (8) [75] :** We define $u = \sum_i h_i x_i$ and $v = \sum_k g_k p_k$ ($h_1$ and $g_1$ are chosen to be 1), and denote each bipartition by $S_r - S_s$ where $S_r$ and $S_s$ are two disjoint sets of parties/modes so that their union is

the whole set of $N$ parties/modes. The $N$-partite single inequality is then

$$(\Delta u)^2 + (\Delta v)^2 \geq 2\min\{S_B\}, \tag{1.46}$$

where $S_B$ is the set of the numbers $\left(\left|\sum h_r g_r\right| + \left|\sum h_s g_s\right|\right)$, where the sums involve all modes in a particular bipartition. The violation of this inequality (1.46) demonstrates genuine $N$-partite entanglement.

For concreteness, let's consider the 4-partite case. The bipartitions for this case are $S_r - S_s = \{123-4, 124-3, 234-1, 134-2, 12-34, 13-24, 14-23\}$ and the corresponding set of numbers $S_B$ is then

$$\{|1+h_2g_2+h_3g_3|+|h_4g_4|, |1+h_2g_2+h_4g_4|+|h_3g_3|, |h_2g_2+h_3g_3+h_4g_4|+1,$$
$$|1+h_2g_2|+|h_3g_3+h_4g_4|, |1+h_3g_3|+|h_2g_2+h_4g_4|, |1+h_4g_4|+|h_2g_2+h_3g_3|\}.$$

Thus far, we derived criteria, first for genuine tripartite entanglement, and then genuine multipartite entanglement. In the next section, we are concerned about how these criteria can be optimally violated, as a function of the input state and the degree of squeezing in the input state.

## 1.4 Optimisation of gains

In Section 1.3.3, we discussed the quantities that are to be measured in a quantum optical experiment involving CV GHZ states and CV EPR-type states. They are given by Eq. (1.30) and are listed below:

$$(\Delta u)^2 = \left[\Delta\left(h_1x_1 + h_2x_2 + ... + h_nx_n\right)^2\right]$$
$$(\Delta v)^2 = \left[\Delta\left(g_1p_1 + g_2p_2 + ... + g_np_n\right)^2\right], \tag{1.47}$$

where $h_1, ..., h_n$ and $g_1, ..., g_n$ are real numbers that are not yet determined. Depending on the quantum state, specific choices of these coefficients minimise the variances of quantities in Eq. (1.47). For

instance, the tripartite CV EPR state, in the limit of large squeezing, has the following correlations:

$$\left\langle x_1 - \frac{(x_2+x_3)}{\sqrt{2}} \right\rangle = \sqrt{2}\left\langle x_2^{(in)} \right\rangle \to 0$$
$$\left\langle p_1 - \frac{(p_2+p_3)}{\sqrt{2}} \right\rangle = \sqrt{2}\left\langle p_1^{(in)} \right\rangle \to 0\,, \tag{1.48}$$

Choosing $h_1 = g_1 = 1$ and $h_2 = h_3 = g_2 = g_3 = \frac{1}{\sqrt{2}}$ minimise $(\Delta u)^2$ and $(\Delta v)^2$ and as a result, a Criteria (5) and (6) can be violated optimally for a tripartite CV EPR state. For the case where the squeezing of input states is finite or when there are noises in the input states, the violation of that criterion is no longer optimal with those coefficients in the example above. Coefficients can then be chosen to reflect the corresponding different correlations among different modes. In this sense, the criteria derived so far are flexible and general.

Note, however, that our derivations are independent of the quantum states that these criteria certify. The lesson here is that criteria can be violated more easily if we choose the coefficients in Eq. (1.47) as a function of the quantum state that one wishes to certify. With that in mind, we choose the set of coefficients $h_1,...,h_n$ and $g_1,...,g_n$ such that the variances $(\Delta u)^2$ and $(\Delta v)^2$ are minimised, and we expect these coefficients to depend on the amount of squeezing in the input states.

In this section, we relate the choices of these coefficients to the input states of the experimental setups described in Section 1.2. Incidentally, both the coefficients and input states are the only controllable parameters in the experimental setups described in Section 1.2 (Actually, this is not quite accurate. The beam splitter reflectivities can be changed. However, once these reflectivities are fixed, the input modes and gain coefficients are the only free parameters.). In the preparation stage, the input modes are characterised by their corresponding squeezing parameters; while the coefficients are electronic gains that can be tuned in the detection stage [96].

Here, we describe how quantities in Eq. (1.47) are measured in an experiment. The quadratures $x_i$'s and $p_i$'s are measured using the standard homodyne detection scheme. Appropriate electronic gains are applied to these measured quadratures according to the set of coefficients $h_1,...,h_n$ and $g_1,...,g_n$. Depending on the sign of these coefficients, the outputs are then electronically summed/subtracted, and the variances of these quantities are subsequently inferred from the noise power using spectrum analysers.

### 1.4.1 Tripartite case

Let's begin by considering the tripartite case. In both the experimental setups to generate CV GHZ and EPR-type states, we choose $h_1 = g_1 = 1$. In the following, we calculate the choices of $h_2$, $h_3$, $g_2$ and $g_3$ explicitly for the tripartite CV GHZ state. Using Eq. (1.16) that relates the output modes $a_j$ to the input modes $a_j^{(in)}$:

$$\begin{aligned} a_1 &= \frac{1}{\sqrt{2}}\left[a_1^{(in)} + a_2^{(in)}\right] \\ a_2 &= \frac{1}{2}\left[a_1^{(in)} - a_2^{(in)}\right] + \frac{1}{\sqrt{2}}a_3^{(in)} \\ a_3 &= \frac{1}{2}\left[a_1^{(in)} - a_2^{(in)}\right] - \frac{1}{\sqrt{2}}a_3^{(in)}, \end{aligned} \tag{1.49}$$

we express the quantity $\Delta^2 u$ in terms of the input modes as below:

$$\begin{aligned} (\Delta u)^2 &= \left[\Delta\left(x_1 + h_2 x_2 + h_3 x_3\right)^2\right] \\ &= \left(\frac{1}{\sqrt{2}} + \frac{h_2}{2} + \frac{h_3}{2}\right)^2 \left(\Delta x_1^{(in)}\right)^2 + \left(\frac{1}{\sqrt{2}} - \frac{h_2}{2} - \frac{h_3}{2}\right)^2 \left(\Delta x_2^{(in)}\right)^2 \\ &\quad + \left(\frac{h_2}{\sqrt{2}} - \frac{h_3}{\sqrt{2}}\right)^2 \left(\Delta x_3^{(in)}\right)^2. \end{aligned} \tag{1.50}$$

Here, $\left(\Delta x_j^{(in)}\right)^2$ is the variance of the $x$ quadrature of the $i$-th input mode. Next, we compute $\frac{d}{dh_2}[\Delta u]^2$, which will be set to zero in order to find the optimal $h_2$ that minimises $(\Delta u)^2$. We obtain

$$\begin{aligned} \frac{d}{dh_2}[\Delta u]^2 =& h_2\left(\frac{1}{\sqrt{2}} + \frac{h_2}{2} + \frac{h_3}{2}\right)\left(\Delta x_1^{(in)}\right)^2 - h_2\left(\frac{1}{\sqrt{2}} - \frac{h_2}{2} - \frac{h_3}{2}\right)\left(\Delta x_2^{(in)}\right)^2 \\ &+ \sqrt{2}h_2\left(\frac{h_2}{\sqrt{2}} - \frac{h_3}{\sqrt{2}}\right)\left(\Delta x_3^{(in)}\right)^2. \end{aligned} \tag{1.51}$$

We note that the right side of Eq. (1.51) is identical to the expression we get for $\frac{d}{dh_3}[\Delta u]^2$. Thus, $h_2 = h_3 = h$. Setting $\frac{d}{dh_2}[\Delta u]^2 = 0$, the optimal $h_2$ is found to be

$$h = -\frac{(\Delta x_1^{(in)})^2 - (\Delta x_2^{(in)})^2}{(\Delta x_2^{(in)})^2 + 2(\Delta x_1^{(in)})^2}, \tag{1.52}$$

where $(\Delta x_1^{(in)})^2 = e^{2r}$ and $(\Delta x_2^{(in)})^2 = e^{-2r}$ with $r$ as the squeezing parameter. By carrying out the same procedure for $(\Delta v)^2$, we find $g_2 = g_3 = g$ and

$$g = -\frac{(\Delta p_1^{(in)})^2 - (\Delta p_2^{(in)})^2}{(\Delta p_2^{(in)})^2 + 2(\Delta p_1^{(in)})^2}, \tag{1.53}$$

where $(\Delta p_1^{(in)})^2 = e^{-2r}$ and $(\Delta p_2^{(in)})^2 = e^{2r}$ are the variances of $p$ quadratures of the input modes. For large squeezing, $h = -\frac{1}{2}$ and $g = 1$, which coincide with the correlations given in Eq. (1.14). The second derivative test shows that these optimal choices of $h$ and $g$ minimise the variances $\Delta^2 u$ and $\Delta^2 v$.

| **r** | **CV GHZ** | | **EPR** | |
|---|---|---|---|---|
| | **g** | **h** | **g** | **h** |
| 0 | 0 | 0 | 0 | 0 |
| 0.25 | 0.36 | -0.27 | 0.33 | -0.33 |
| 0.5 | 0.68 | -0.40 | 0.54 | -0.54 |
| 0.75 | 0.86 | -0.46 | 0.64 | -0.64 |
| 1 | 0.95 | -0.49 | 0.68 | -0.68 |
| 1.5 | 0.99 | -0.50 | 0.70 | -0.70 |
| 2 | 1.00 | -0.50 | 0.70 | -0.70 |

Table 1.1: Values of $g$ and $h$ used for the plots of Fig 1.7.

On the other hand, the set of coefficients for the CV GHZ state, using the exact procedure presented above, are:

$$\begin{aligned} h &= -\frac{(\Delta x_1^{(in)})^2 - (\Delta x_2^{(in)})^2}{\sqrt{2}[(\Delta x_2^{(in)})^2 + (\Delta x_1^{(in)})^2]} \\ g &= -\frac{(\Delta p_1^{(in)})^2 - (\Delta p_2^{(in)})^2}{\sqrt{2}[(\Delta p_2^{(in)})^2 + (\Delta p_1^{(in)})^2]}. \end{aligned} \tag{1.54}$$

The variances for the $x$ and $p$ quadratures of the input modes are the same as the CV GHZ state. Again, in the large squeezing limit, we have $h = -\frac{1}{\sqrt{2}}$ and $g = \frac{1}{\sqrt{2}}$, which are exactly the coefficients used in Criterion (3) and Criterion (4) in Eq. (1.41) and Eq. (1.42), respectively.

The coefficients in Criterion (5) and Criterion (6) for both the tripartite CV GHZ and tripartite CV EPR states are presented in Table 1.1. These coefficients are obtained from the analytical expressions

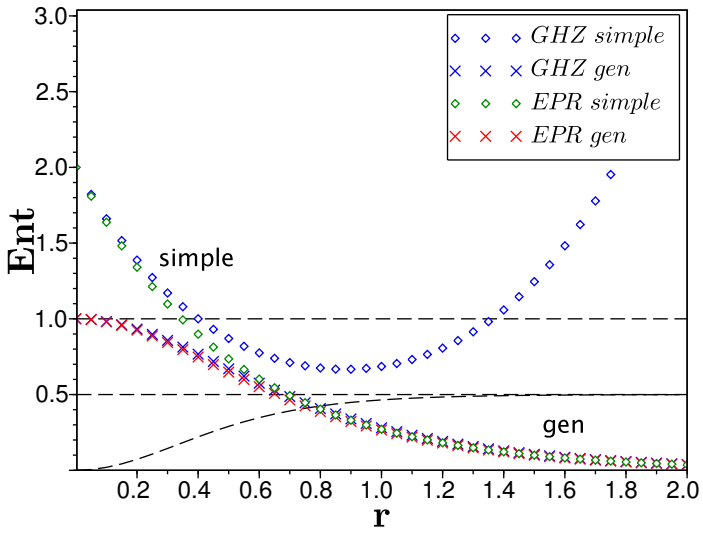


Figure 1.7: Genuine tripartite entanglement and EPR steering detection as a function of the squeezing parameter $r$. Criteria (3) and (4) are labelled as "simple" in the legend and their results are indistinguishable. Criteria (5) and (6) are labelled as "gen" in the legend and again their results are indistinguishable. These criteria are normalised so that $Ent < 1$ implies genuine tripartite entanglement.

given in Eq. (1.52) and Eq. (1.53) for the tripartite CV GHZ state and in Eq. (1.54) for the tripartite CV EPR state. From the Table 1.1, we see that $g$ and $h$ are zero when there is no squeezing. This is expected as there are no correlations between quadratures of different modes without squeezed inputs. Also, for the squeezing parameter $r = 2$, the coefficients are the same as those predicted in the large squeezing limit, suggesting that this limit is already reached for $r = 2$. To get a feel for the magnitude, in the work of Armstrong et al. [97], where the squeezing is large enough to observe both genuine tripartite entanglement and EPR steering, the maximum squeezing achieved experimentally in the variance of an input mode quadrature is $-4.1$dB, relative to the quadrature of a vacuum mode. This corresponds to a squeezing parameter $r$ of 0.472.

We plot the values of Criteria (3), (4), (5) and (6) in Fig. 1.7. Since these criteria have different lower bounds, we divide the left side by the right side of these criteria and define this as $Ent$. This allows different values of these different criteria to be plotted in a single figure. W normalise these criteria such that if $Ent$ is less than 1, genuine tripartite entanglement is certified and if $Ent$ is less than 0.5, genuine tripartite EPR steering is certified.

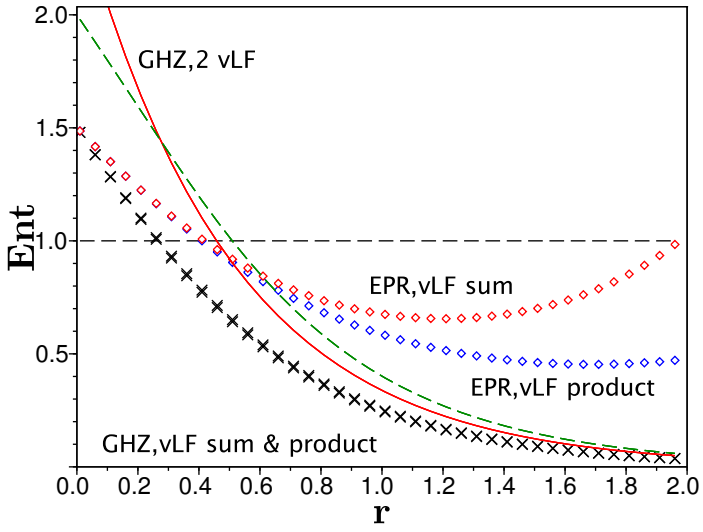


Figure 1.8: Genuine tripartite entanglement and EPR steering detection as a function of the squeezing parameter $r$. Criteria (1) and (2) are labelled as "vLF sum" and "vLF product" respectively; while Criterion (7) is labelled as "2 vLF". These criteria are normalised so that $Ent < 1$ implies genuine tripartite entanglement.

Table 1.2: Values of $g_i$ $(i = 1,2,3)$ for the plots of Figure 1.8. The same values are used for the sum and product versions of the criteria.

| **r** | **GHZ** | | | **EPR** | | |
|---|---|---|---|---|---|---|
| | $g_1$ | $g_2$ | $g_3$ | $g_1$ | $g_2$ | $g_3$ |
| 0 | 0 | 0 | 0 | 0 | 0 | 0 |
| 0.25 | 0.53 | 0.53 | 0.53 | 0.63 | 0.29 | 0.29 |
| 0.5 | 0.81 | 0.81 | 0.81 | 1.08 | 0.44 | 0.44 |
| 0.75 | 0.93 | 0.93 | 0.93 | 1.28 | 0.50 | 0.50 |
| 1 | 0.97 | 0.97 | 0.97 | 1.36 | 0.50 | 0.50 |
| 1.5 | 1.00 | 1.00 | 1.00 | 1.41 | 0.46 | 0.46 |
| 2 | 1.00 | 1.00 | 1.00 | 1.41 | 0.43 | 0.43 |

For Criterion (7) in Eq. (1.45), the coefficients in $B_I$, $B_{II}$ and $B_{III}$ as given in Eq. (1.28) are obtained using the same method as described above. We list the coefficients in Criterion (7) for both the CV GHZ and CV EPR states in Table 1.2. Based on these coefficients, we plot the values of Criteria (1), (2) and (7) as a function of squeezing parameter $r$ for both the CV GHZ and CV EPR states in Fig. 1.8. Identical to Fig. 1.7, the criteria are normalised such that $Ent < 1$ implies genuine tripartite entanglement.

### 1.4.2 Multipartite case

We also obtain analytical expressions for the quantities $(\Delta u)^2$ and $(\Delta v)^2$ for the arbitrary $N$-partite case. They are obtained using exactly the same method as described in the previous section. However, explicit calculations are tedious and not instructive to be included here, and we only present the final expressions. For CV GHZ state, $(\Delta u)^2$ and $(\Delta v)^2$ are expressed in terms of the variances of input modes as follows:

$$(\Delta u)^2 = \frac{1}{N}[(N-1)^2h^2 + 2h(N-1) + 1](\Delta x_1^{(in)})^2 + \frac{(N-1)}{N}[h^2 - 2h + 1](\Delta x_2^{(in)})^2$$

$$(\Delta v)^2 = \frac{1}{N}[(N-1)^2g^2 + 2g(N-1) + 1](\Delta p_1^{(in)})^2 + \frac{(N-1)}{N}[g^2 - 2g + 1](\Delta p_2^{(in)})^2, \qquad (1.55)$$

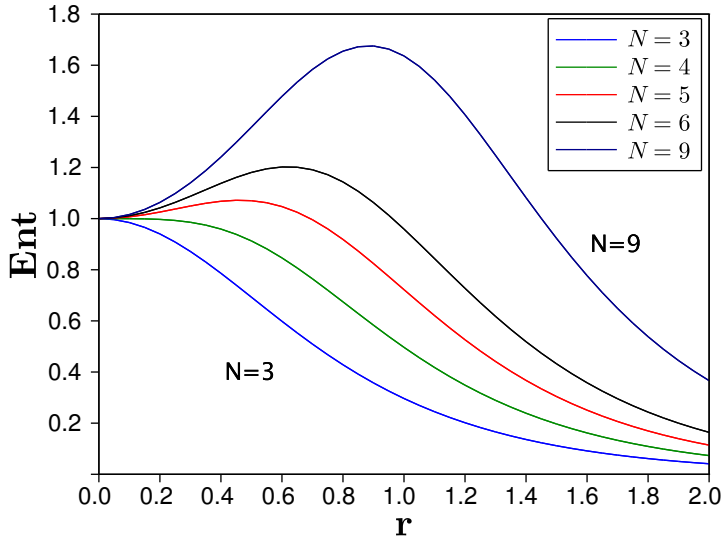


Figure 1.9: Genuine $N$-partite entanglement using Criterion (8) as a function of the squeezing parameter $r$ for the CV GHZ state.

which gives, after differentiating, the choice of

$$h = -\frac{(\Delta x_1^{(in)})^2 - (\Delta x_2^{(in)})^2}{(\Delta x_2^{(in)})^2 + (N-1)(\Delta x_1^{(in)})^2}$$
$$g = -\frac{(\Delta p_1^{(in)})^2 - (\Delta p_2^{(in)})^2}{(\Delta p_2^{(in)})^2 + (N-1)(\Delta p_1^{(in)})^2}\,. \tag{1.56}$$

Here $(\Delta x_1^{(in)})^2 = e^{2r}$ , $(\Delta x_2^{(in)})^2 = e^{-2r}$ , $(\Delta p_1^{(in)})^2 = e^{-2r}$ and $(\Delta p_2^{(in)})^2 = e^{2r}$ are the variances of the two inputs into the first beam splitter. For the $N = 4$, the gain coefficients reduce to $g = 1$ and $h = -1/3$ in the large $r$ limit. In general, for $g, h$ values satisfying $|gh| \leq 1$, $gh < 0$, $1 - 2gh \geq 1$, one can show that the right-side of Criterion (8) reduces to $2[1 + (N-3)gh]$. Table 1.3 lists the coefficients $g$ and $h$ for the CV GHZ state for 4, 5 and 6 parties/modes. The values of the normalised Criterion (8) for multipartite CV GHZ state as a function of the squeezing parameter $r$ is shown in Fig. (1.9).

The gains for the asymmetric EPR-type state I are obtained with the same method and they are given by:

Table 1.3: Gains for single inequality Criterion (8) for the CV GHZ. Here, $h_1 = g_1 = 1, h_2 = h_3 = h_4 = h, g_2 = g_3 = g_4 = g$.

| r | N=4 | | N=5 | | N=6 | |
|---|---|---|---|---|---|---|
| | g | h | g | h | g | h |
| 0 | 0 | 0 | 0 | 0 | 0 | 0 |
| 0.25 | 0.30 | -0.19 | 0.26 | -0.14 | 0.22 | -0.12 |
| 0.5 | 0.61 | -0.28 | 0.56 | -0.21 | 0.52 | -0.17 |
| 0.75 | 0.83 | -0.31 | 0.79 | -0.23 | 0.76 | -0.19 |
| 1 | 0.93 | -0.33 | 0.91 | -0.24 | 0.90 | -0.20 |
| 1.5 | 0.99 | -0.33 | 0.99 | -0.25 | 0.99 | -0.20 |
| 2 | 1.00 | -0.33 | 1.00 | -0.25 | 1.00 | -0.20 |

$$h = -\frac{(\Delta x_1^{(in)})^2 - (\Delta x_2^{(in)})^2}{\sqrt{(N-1)}[(\Delta x_2^{(in)})^2 + (\Delta x_1^{(in)})^2]}$$
$$g = -\frac{(\Delta p_1^{(in)})^2 - (\Delta p_2^{(in)})^2}{\sqrt{(N-1)}[(\Delta p_2^{(in)})^2 + (\Delta p_1^{(in)})^2]}. \tag{1.57}$$

For $N = 4$, the gain coefficients reduce to $g = 1/\sqrt{3}$ and $h = -1/\sqrt{3}$ at large $r$.

Table 1.4: Gains for the single inequality Criterion (8), as used for the asymmetric EPR-type state I.

| r | N=4 | | N=5 | | N=6 | |
|---|---|---|---|---|---|---|
| | g | h | g | h | g | h |
| 0 | 0 | 0 | 0 | 0 | 0 | 0 |
| 0.25 | 0.27 | -0.27 | 0.23 | -0.23 | 0.21 | -0.21 |
| 0.5 | 0.44 | -0.44 | 0.38 | -0.38 | 0.34 | -0.34 |
| 0.75 | 0.52 | -0.52 | 0.45 | -0.45 | 0.40 | -0.40 |
| 1 | 0.56 | -0.56 | 0.48 | -0.48 | 0.43 | -0.43 |
| 1.5 | 0.57 | -0.57 | 0.50 | -0.50 | 0.45 | -0.45 |
| 2 | 0.58 | -0.58 | 0.50 | -0.50 | 0.45 | -0.45 |

Finally, the analytical expressions of the gain coefficients for the symmetric EPR-type state II can be obtained in the same way. However, the expressions depend on whether the number of parties that are involved is even or odd. We do not include them here and just list the values of these coefficients.

Table 1.5: Gains for single inequality Criterion (8) for the symmetric EPR-type II state. Here $h_1 = g_1 = 1, h_2 = h_3 = ... = h_R, g_2 = g_3 = ...g_R, h_4 = h_6 = ... = h_L = g_4 = g_6 = ... = g_L$.

| **r** | **N=4** | | | **N=5** | | | **N=6** | | |
|---|---|---|---|---|---|---|---|---|---|
| | $h_R$ | $h_L$ | $g_R$ | $h_R$ | $h_L$ | $g_R$ | $h_R$ | $h_L$ | $g_R$ |
| 0 | 0 | 0 | 0 | 0 | 0 | 0 | 0 | 0 | 0 |
| 0.25 | -0.24 | -0.06 | 0.24 | -0.20 | -0.06 | 0.20 | -0.17 | -0.04 | 0.17 |
| 0.5 | -0.46 | -0.21 | 0.46 | -0.38 | -0.21 | 0.38 | -0.33 | -0.15 | 0.33 |
| 0.75 | -0.63 | -0.40 | 0.63 | -0.52 | -0.40 | 0.52 | -0.50 | -0.31 | 0.50 |
| 1 | -0.76 | -0.58 | 0.76 | -0.62 | -0.58 | 0.62 | -0.63 | -0.50 | 0.63 |
| 1.5 | -0.91 | -0.82 | 0.91 | -0.74 | -0.82 | 0.74 | -0.83 | -0.75 | 0.83 |
| 2 | -0.96 | -0.93 | 0.96 | -0.79 | -0.93 | 0.79 | -0.93 | -0.90 | 0.93 |

Table 1.4 and Table 1.5 list the coefficients $g$ and $h$ for the asymmetric CV EPR *I* and the symmetric CV EPR *II* states, respectively, for 4, 5 and 6 parties/modes. The normalised Criterion (8) for the asymmetric CV EPR *I* state as a function of the squeezing parameter $r$ is plotted in Fig. 1.10.

## 1.5 Effect of losses

The results presented thus far are for pure states that can only be generated under ideal conditions with optimal control of the quantum system. Even if they are generated, noises and fluctuations from the environment would inevitably degrade these idealised states, turning them into mixed states. Two main sources of noises in the experiments are the impurity of the input squeezed states and the losses that occur during transmission along the channels. The impurity of the input squeezed states can be taken into account by using input states with larger quadrature variances than those predicted in theory as in Eq. (1.8). In this section, we focus on the effect of losses.

We model the transmission losses with a simple beam splitter model that has the unitary transformations on the modes given in Eq. (1.12), such that the detected output is $a_{out} = \sqrt{\eta}a_{in} + \sqrt{(1-\eta)}a_{vac}$, where $a_{in}$ is the mode before loss, $a_{vac}$ is a vacuum state and $\eta$ is the transmissivity that characterise the efficiency of the transmission or the detection process.

The effect of loss on the genuine tripartite entanglement as detected by the Criteria (5) and (6) is shown in the Fig. 1.11 and Fig. 1.12. Fig. 1.11 shows the effect of losses in mode labelled 1 while modes 2 and 3 are lossless; while Fig. 1.12 shows the effect of losses in modes labelled 2 and 3, without

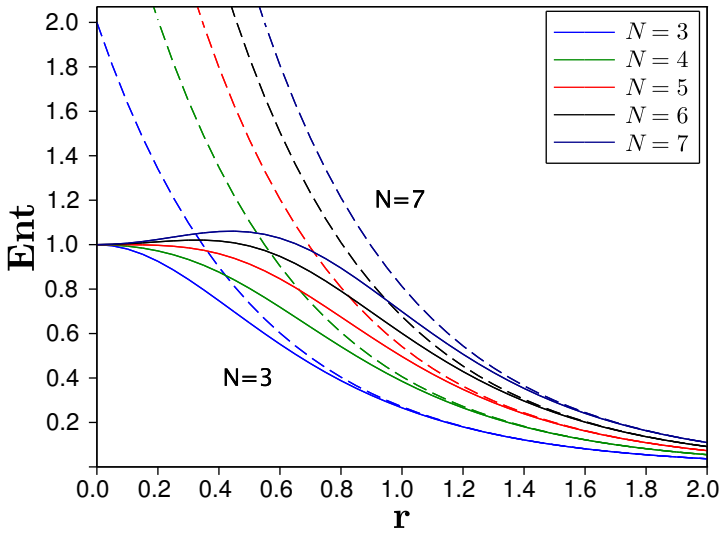


Figure 1.10: Genuine N-partite entanglement for the asymmetric EPR-type state I, using the generalised Criterion (8) (solid lines) for different number of parties. The dashed lines correspond to a criterion not described in this thesis. It is derived by van Loock et. al [1] and is given by $Ent = \frac{\Delta^2 u + \Delta^2 v}{4/(N-1)}$ . The values of $g_i$ and $h_i$ are given in Table 1.4.

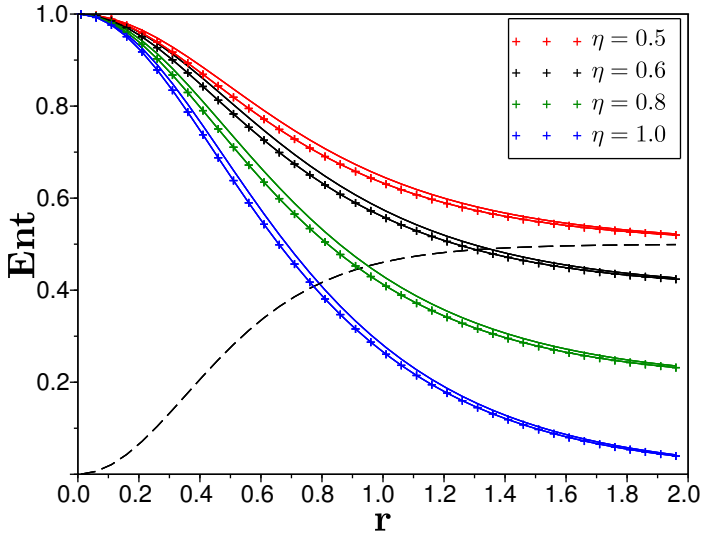


Figure 1.11: Genuine tripartite entanglement with losses on the mode 1, using Criterion (6). The solid curves correspond to GHZ states while + curves correspond to EPR-type states.

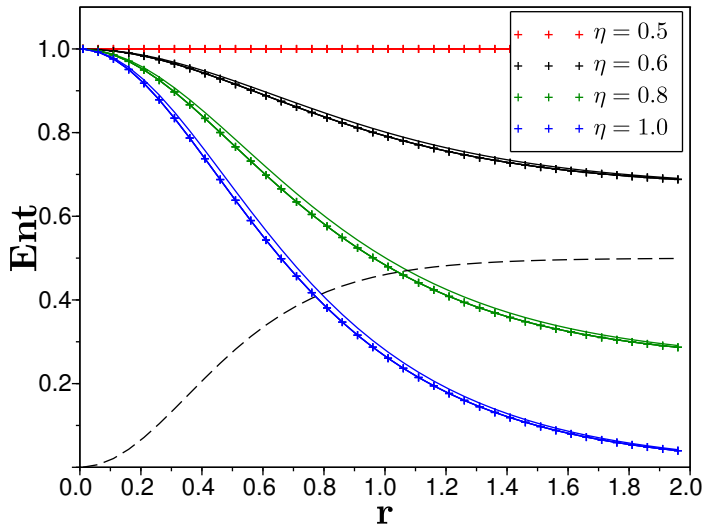


Figure 1.12: Genuine tripartite entanglement with losses on the modes 2 and 3, using Criterion (6). The solid curves correspond to GHZ states while + curves correspond to EPR-type states.

losses in mode 1. Recall that the quantity $Ent < 1$ implies genuine tripartite entanglement. We see that the degree of tripartite entanglement reduces with the decreasing transmission efficiency $\eta$. However, with large enough squeezing, genuine tripartite entanglement is still observed even for relative low transmission efficiencies.

We also investigated the notion of quantum entanglement monogamy in these quantum optical systems. The entanglement monogamy provides insights on the shareability of quantum entanglement. Monogamy relations are derived and a few CV tripartite states are used to check for these monogamy relations. These relations are found to always hold. All related results can be found in Appendix A.

Here, we just want to point out that these monogamy relations have been confirmed, for instance, in the experiment of Bowen et al. [89]. The experiment detected continuous-variable entanglement in a pair of beams generated using optical parametric amplifiers and a beam splitter. In that experiment, they considered the effect of losses on a bipartite continuous-variable entanglement that is certified using a particular criterion, known as the TDGCZ entanglement certifier. In particular, they observed that when the detection efficiency is 50%, the TDGCZ criterion is saturated. In other words, the criterion detects no bipartite continuous-variable entanglement at that level of efficiency. Using the same experimental configuration, the TDGCZ monogamy relation of Result (1) (see Appendix A) replicated this

observation: the saturation observed in the experiment is a simple consequence of the system satisfying the monogamy relation.

This observation is by no means the only example that can be explained by the monogamy of entanglement. For instance, in the investigation of genuine tripartite EPR-steering in both the CV GHZ and CV EPR-type states with losses [75], results show that no matter how large the squeezing parameter $r$ is, as long as the transmission efficiency is equal or less than 50%, there is no EPR-steering. Similar to the scenario in the experiment of Bowen et al., this can be explained with the result in the work of Reid based on monogamy relations of EPR-steering in a continuous-variable tripartite system [98].

## 1.6 Summary and outlook

We defined the notion of genuine multipartite continuous-variable quantum entanglement. Based on the definition, we derived the corresponding criteria to certify genuine multipartite continuous-variable quantum entanglement. In particular, we consider quantum states generated from quantum optical systems and apply our criteria to these states. The effect of losses in the system was also investigated. The genuine tripartite entanglement was detected in an experiment carried out by the quantum optics group in Australian National University (ANU) [97]. Armstrong et al. [96] devised a programmable multimode quantum network that emulates a linear optics network, and used this to create CV tripartite EPR-type states that are described in Fig. 1.3. The different quadratures of all modes were then measured with a homodyne detection scheme, which were then used to check for the genuine tripartite entanglement criterion (4) as given in Eq. (1.42). The minimum value of the genuine tripartite entanglement obtained from experimental measurements is around 0.7, which remarkably agrees with the theoretical prediction within the error bars due to imperfect homodyne detection. This unambiguously demonstrates genuine tripartite entanglement in a continuous-variable quantum optical system as presented in this chapter. For a review of the various experiments on the detection of continuous-variable EPR entanglement, see Ref. [90].

It is worth briefly discussing the classes of quantum correlations not presented in this chapter. In the criteria for genuine multipartite continuous-variable entanglement, all biseparable states in a bipartition are quantum mechanical. They satisfy Heisenberg uncertainty principle and thus constrains and place a bound for the uncertainties of certain observables. We can proceed the same way with genuine

multipartite EPR-steering, with the difference that only one partition in the bipartition is quantum mechanical and satisfies the uncertainty principle; while the other partition does not. The associated variances in the non-quantum partition are assumed to be non-negative and hence have a lower bound of zero. The resulting criteria will then have a smaller lower bound, which means that the certifier (the variances of certain observables involved in the corresponding criterion) has to be lower too to violate the inequality. In other words, stronger quantum correlations are needed to reduce the certifiers and demonstrate genuine EPR-steering.

In the case of continuous-variable Bell nonlocality, all biseparable states in all bipartitions are non-quantum. It is immediately obvious that the criteria of the form discussed will not rule out the hidden local variables model as there is no uncertainty principle to provide a non-zero lower bound. We note, however, that Bell inequalities that certify multipartite continuous-variable Bell nonlocality have been derived, for instance, the Cavalcanti-Foster-Reid-Drummond inequalities in Ref. [99–101] and in the case of discrete multipartite, the Svetlichny inequalities [102].

Even though the criteria presented in this chapter are for the continuous-variable case, the approach used in deriving these criteria would also work for the discrete-variable case, where the observables have discrete outcomes. This would require the appropriate uncertainty relations to be used. Criteria for multipartite quantum correlations in discrete-variable high spin systems with a finite dimension have been derived, for instance, in the works in Refs. [101, 103]. These criteria do not, however, detect genuine multipartite entanglement. Reviews on quantum correlation criteria for the discrete-variable case can be found in Refs. [104–106].

The publications that are relevant to this chapter are:

- R. Y. Teh and M. D. Reid, *Criteria for genuine N-partite continuous-variable entanglement and Einstein-Podolsky-Rosen steering*, Phys. Rev. A **90**, 062337 (2014).

- L. Rosales-Zárate, R. Y. Teh, B. Opanchuk, and M. D. Reid, *Monogamy inequalities for certifiers of continuous-variable Einstein-Podolsky-Rosen entanglement without the assumption of Gaussianity,* Phys. Rev. A **96**, 022313 (2017).

# Chapter 2

# Quantum correlations in NOON states

A Bell state $|\psi\rangle = \frac{1}{\sqrt{2}}\left(|10\rangle_{AB} + e^{i\phi}|01\rangle_{AB}\right)$ is a maximally entangled state, where $|10\rangle_{AB}$ is a state with one particle in mode $A$ and zero particle in mode $B$ ($|01\rangle_{AB}$ is defined similarly). It is well-known that its non-classicality cannot be demonstrated from the statistics of photon number measurements; a local hidden variable explanation exists. A Bell inequality is required to rule out the possibility of a hidden variable model.

A NOON state

$$|\psi_{NOON}\rangle = \frac{1}{\sqrt{2}}\left(|N0\rangle_{AB} + e^{i\phi}|0N\rangle_{AB}\right) \tag{2.1}$$

is also a maximally entangled state. In fact, for large $N$, the NOON state is a Schrodinger's cat state - a quantum superposition of states with macroscopically different quantum number $N$ in each mode. It is similar to the Bell state above, but at a larger scale. Devising a way to investigate the quantum nature of the NOON state is a challenge. Previous work has proposed Bell inequalities for the NOON state, but so far there has been no experiment for $N > 1$ to our knowledge. Instead, we want to demonstrate the EPR-steering in a NOON state. As described in Section 0.1, EPR-steering is an intermediate class of quantum correlations between Bell nonlocality and quantum entanglement. Although a weaker class of quantum correlation compared to Bell nonlocality, EPR-steering in a physical state is easier to demonstrate and verify.

In Section 2.1, we look at some observables and derive criteria in terms of these observables to show the quantum nature of a NOON state. In particular, we investigate steering, which is a stricter quantum correlation than entanglement, in the NOON state. We do this for the ideal NOON state before

considering the more realistic scenario where losses are taken into account.

The quantum nature of a NOON state lies in the fact that it contains quantum superposition or quantum coherence. However, detecting and quantifying the quantum coherence in a quantum state is nontrivial. We present a test and discuss how the observables in the test can be measured in experiments. It turns out that this test not only detects the presence, but also quantifies, the quantum coherence in a NOON-like state. These are to be found in Section 2.2. This chapter is based on the work by Teh et al. [107] and Opanchuk et al. [108].

## 2.1 Steering inequalities for the NOON state

Let us first discuss the correlation that exists in a NOON state. It is obvious by inspection of Eq. (2.1) that if the mode number of one of the modes is known, the mode number of the other mode is exactly known. In other words, the variance of the observable $\hat{n}_A - \hat{n}_B$ is zero, i.e. $\Delta^2(\hat{n}_A - \hat{n}_B) = 0$. This mathematical expression can be understood as the variance of the mode number inference of, say mode $B$, given measurement outcomes of the mode number of mode $A$. For simplicity, we represent this understanding as $\Delta^2_{inf}\hat{n}_B$.

Of course, to determine that the correlation in a given state is indeed of quantum nature, another observable which is conjugated to the mode number is needed. Any observable that has a nonzero commutation relation with the mode number will work. In this section, we propose the quadratures as the corresponding conjugated observables. This is mainly because quadrature measurements are well established and routinely performed in laboratories.

We certify EPR steering in the NOON state, which is a stricter form of quantum correlation than quantum entanglement. The verification of EPR steering in a NOON state automatically implies the presence of quantum entanglement. Based on the idea from the previous chapter, we consider steering criteria in the form of inequalities. In the following, we introduce steering inequalities involving the mode number and quadrature measurements. These inequalities are

$$E_N^{(p)} = \frac{\Delta_{inf} n_b \Delta_{inf} P_b^N}{\frac{1}{2}|\langle [n_b, P_b^N] \rangle|_{inf}} < 1 \tag{2.2}$$

and

$$E_N^{(x)} = \frac{\Delta_{inf} n_b \Delta_{inf} X_b^N}{\frac{1}{2}|\langle [n_b, X_b^N] \rangle|_{inf}} < 1\,. \tag{2.3}$$

Here, $\Delta_{inf} n_b$, $\Delta_{inf} P_b^N$ and $\Delta_{inf} X_b^N$ are the uncertainties in the inference of $\hat{n}_b$, $\hat{P}_b^N$ and $\hat{X}_b^N$, given measurement of $\hat{n}_a$, $\hat{X}_a$ and $\hat{X}_a$, respectively. To be precise,

$$\begin{aligned}\Delta_{inf}^2 n_b &= \sum_{n_a} P(n_a) \sum_{n_b} P(n_b|n_a) \left[n_b - \langle n_b \rangle_{n_a}\right]^2 \\ &= \sum_{n_a} P(n_a)\, \Delta_{inf}^2 (n_b|n_a)\,,\end{aligned} \tag{2.4}$$

where $\langle n_b \rangle_{n_a}$ is the average value of $n_b$ given the measurement $\hat{n}_a$ with a specific outcome $n_a$ and $\Delta_{inf}^2 (n_b|n_a) = \sum_{n_b} P(n_b|n_a) \left[n_b - \langle n_b \rangle_{n_a}\right]^2$. Similarly,

$$\begin{aligned}\Delta_{inf} P_b^N &= \int\int P(x_a)\, P\left(p_b^N|x_a\right) \left[p_b^N - \langle p_b^N \rangle_{x_a}\right]^2 dp_b^N dx_a \\ &= \int P(x_a)\, \Delta_{inf}^2 \left(p_b^N|x_a\right) dx_a\,,\end{aligned} \tag{2.5}$$

where $\Delta_{inf}^2 \left(p_b^N|x_a\right) = \int P\left(p_b^N|x_a\right) \left[p_b^N - \langle p_b^N \rangle_{x_a}\right]^2 dp_b^N$. We note that the criteria (2.2) and (2.3) hold for any measurements on mode $a$, but they are chosen to optimise the violation of these criteria. If either one of the inequalities in Eq. (2.2) and Eq. (2.3) holds, the quantum state contains EPR-steering, where mode $B$ can be steered by mode $A$. We should mention that criteria involving additive or multiplicative variances, which include all criteria in this thesis, are not suitable for certifying Bell nonlocality. However, NOON states do contain Bell nonlocality, as certified by Bell inequalities [109].

We compute analytically both $E_N^{(p)}$ and $E_N^{(x)}$ for the ideal NOON state with arbitrary mode number $N$ as given by Eq. (2.1). The calculations can be carried out straightforwardly but are lengthy and hence will not be included here. All details can be found in Appendix C. It should be pointed out, however, that the inequality (2.2) is useful when $\cos\phi \neq 0$ for odd $N$ and $\sin\phi \neq 0$ for even $N$; while the inequality (2.3) is useful when $\sin\phi \neq 0$. When these conditions are not satisfied, it turns out that the commutators in the corresponding inequalities are zero.

We also model losses using beam splitter operations, identical to the loss model described in Section 1.5. The effect of losses is especially important in the study of NOON states. This is because a

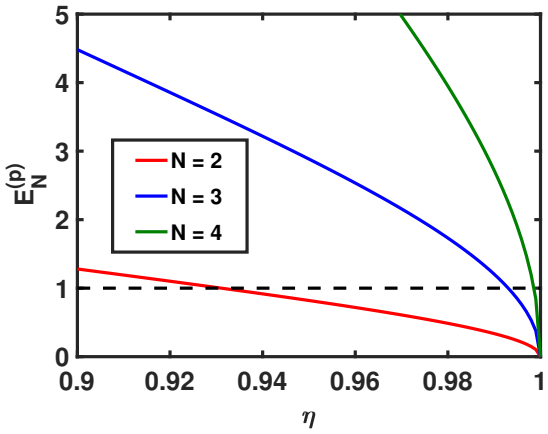


Figure 2.1: EPR steering in NOON states subjected to losses.

mesoscopic/macroscopic quantum state such as a NOON state is very sensitive to interaction with its environment and losses. In order to compute the steering parameters $E_N^{(p)}$ and $E_N^{(x)}$ for the lossy case, it is more convenient to use the density operator formalism. Using the beam splitter operation to model losses, the detected mode operators $a_{det}$, $b_{det}$ for modes $A$ and $B$ in terms of their corresponding initial mode operators $a$ and $b$ are:

$$\begin{aligned} a_{det} &= \sqrt{\eta_a}a + \sqrt{1-\eta_a}a_v \\ b_{det} &= \sqrt{\eta_b}b + \sqrt{1-\eta_b}b_v\,, \end{aligned} \tag{2.6}$$

where $\eta_a$ and $\eta_b$ are the transmission efficiencies for modes $A$ and $B$ respectively. Now, starting from the ideal NOON state

$$\begin{aligned} |\psi_{NOON}\rangle &= \frac{1}{\sqrt{2}}\left(|N0\rangle_{AB} + e^{i\phi}|0N\rangle_{AB}\right) \\ &= \frac{1}{\sqrt{2}}\left[\frac{\left(a^\dagger\right)^N}{\sqrt{N!}} + e^{i\phi}\frac{\left(b^\dagger\right)^N}{\sqrt{N!}}\right]|00\rangle\,, \end{aligned} \tag{2.7}$$

we express the mode operators $a$ and $b$ in terms of their respective detected mode operators $a_{det}$, $b_{det}$.

This leads to an expression of a lossy NOON state. The corresponding density operator has the form:

$$\rho_{lossy} = \frac{1}{2}\left[\sum_s \binom{N}{N-s} (\eta_a)^{N-s}(1-\eta_a)^s \,|N-s,0\rangle\langle N-s,0| + (\sqrt{\eta_a\eta_b})^N e^{-i\phi}\,|N,0\rangle\langle 0,N| \right.$$
$$\left. + (\sqrt{\eta_a\eta_b})^N e^{i\phi}\,|0,N\rangle\langle N,0| + \sum_s \binom{N}{N-s} (\eta_b)^{N-s}(1-\eta_b)^s \,|0,N-s\rangle\langle 0,N-s|\right]. \quad (2.8)$$

Any expectation value of an observable $O$ is then obtained by evaluating $\mathrm{Tr}\left(\rho_{lossy}O\right)$. Here, we consider the NOON state with $\phi = 0$ and so we present the results of $E_N^{(p)}$. The values of $E_N^{(p)}$ for different loss rates, characterised by $1-\eta$, where $\eta_a = \eta_b = \eta$ is the transmission efficiency, and different mode number $N$ are plotted in Fig. 2.1. We see from this figure that EPR steering is extremely sensitive to losses and this is especially so for larger $N$. Of course, this is just the standard explanation for why we do not observe a macroscopic Schrodinger's cat: they are destroyed by the slightest of noise and losses.

In practice, ideal NOON states are very hard to prepare and one is more likely to produce NOON-like states instead. They consist of superpositions of states other than $|N0\rangle$ and $|0N\rangle$, with the other states still having a number difference of $N$ between modes. They have the form [101, 110, 111]

$$|\psi\rangle = \sum_{m=0}^{N} d_m |N-m\rangle_a |m\rangle_b \,. \quad (2.9)$$

What cannot be answered by these inequalities, though, is what provides quantum correlations in the first place? For ideal NOON states, the answer lies, of course, on the fact that we have a quantum superposition or quantum coherence of two macroscopically distinguishable states. Surely there must also be some degree of quantum coherence in a nonideal NOON state for it to have quantum correlations. This naturally leads to the question: How can we quantify the quantum coherence of a quantum state? The characterisation of the quantum coherence of a NOON state is nontrivial and we propose a practical measure for this in the next section.

## 2.2 Quantifying the two-mode quantum coherence of nonideal NOON-type states

Let's first analyse the quantum coherence in an ideal NOON state as given in Eq. (2.1)

$$|\psi_{NOON}\rangle = \frac{1}{\sqrt{2}}\left(|N0\rangle_{AB} + e^{i\phi}|0N\rangle_{AB}\right).$$

Consider a measurement of quantum number difference between the modes $A$ and $B$, $2\hat{J}_z \equiv \hat{n}_A - \hat{n}_B$. The outcomes of measurements on $|\psi_{NOON}\rangle$ are labeled as alive and dead, for $\langle 2\hat{J}_z\rangle = N$ and $\langle 2\hat{J}_z\rangle = -N$, respectively. We also define the alive and dead states as $\rho_A = |0N\rangle_{AB}\langle 0N|$ and $\rho_D = |N0\rangle_{AB}\langle N0|$, respectively. It is clear from the density operator $\rho_{NOON}$ for an ideal NOON state that it cannot be expressed as statistical mixture of $\rho_A$ and $\rho_D$. The ideal NOON state contains quantum coherence as evident from the presence of off-diagonal terms in the density operator $\rho_{NOON}$. In fact, we say that an ideal NOON state has $N$-th order quantum coherence from the fact that off-diagonal terms in $\rho_{NOON}$ have the form $|N\rangle\langle 0|$ and $|0\rangle\langle N|$. In other words, in order to confirm $N$-th order quantum coherence, all statistical mixtures of the form

$$\rho_{mix} = P_A\rho_A + P_D\rho_D \tag{2.10}$$

have to be negated. Here $P_A$, $P_D$ are the probabilities of being in the states $\rho_A$, $\rho_D$ respectively, and $P_A + P_D = 1$.

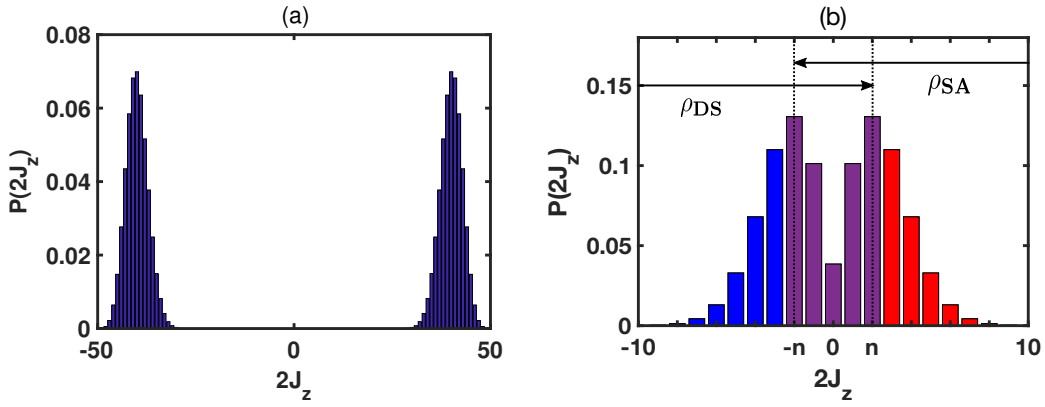


Figure 2.2: Probability $P(2j_z)$ of an outcome of $2\hat{J}_z$ for the lossy NOON state with particle number $N = 50$. Plot (a,b) correspond to $\eta = 0.8$ and $\eta = 0.05$ respectively.

We now turn to nonideal NOON-type states by considering the example of the state characterised by the density operator $\rho_{lossy}$ with total mode number $N$, as in Eq. (2.8). The order of coherence for this state is not as trivial as the ideal NOON state. To see that, we compute the expectation value of the mode number difference between modes $A$ and $B$, $\langle 2\hat{J}_z \rangle$ by evaluating $\mathrm{Tr}\left(2\rho_{lossy}\hat{J}_z\right)$. Taking $\eta_a = \eta_b = \eta$, we get the probability distribution $P(2J_z = m) = \frac{1}{2}\sum_{m=1}^{N} \binom{N}{N-m} \eta^{N-m}(1-\eta)^m$, for both $m < 0$ and $m > 0$, while $P(2J_z = 0) = (1-\eta)^N$. We plot these probability distributions of detecting different number difference $P(2J_z)$ with $\eta = 0.8$ and $\eta = 0.05$ in Fig. 2.2(a) and (b) respectively. Recall in the case of ideal NOON states, all measurement outcomes are identified as either belonging to the dead or alive state, with their corresponding outcome $-N$ and $N$ respectively, giving them an $N$-th order coherence. Fig. 2.2(a) show measurement outcomes that can be binned into two distinguishable groups: they are either dead or alive. However, there is a spread of measurement outcomes in both the dead and alive groups and it is not clear as to how we should quantify its order of coherence. To complicate the issue further, in Fig. 2.2(b), there is a range of measurement outcomes that cannot even be distinguished as either dead or alive, which we labelled as sleepy. It is possible that there are states $\rho_{DS}$ and $\rho_{SA}$ that give the outcome in the combined "dead and/or sleepy" and "sleepy and/or alive" regions, respectively. An unambiguous, operational definition of $n$-th order quantum coherence is hence required. Following Refs. [112, 113], we define the notion of quantum coherence and $n$-th order quantum coherence as below:

**Definition 1** [113]: The state of a physical system displays **quantum coherence** between two outcomes $n_1$ and $n_2$ of an observable $\hat{n}$ if and only if the state $\rho$ of the system cannot be considered as a statistical mixture of some underlying states $\rho_1$ and $\rho_2$, where $\rho_1$ assigns probability zero for $n_2$ and $\rho_2$ assigns probability zero for $n_1$.

**Definition 2** [113]: If $\rho$ displays coherence between some outcomes $2J_z \leq n_1$ and $2J_z \geq n_2$ (for $n_2 > n_1$) such that $n_2 - n_1 \geq n$, then that state has the generalised ***n*-scopic quantum coherence**. This coherence is said to be macroscopic when $n$ is macroscopic.

Using these definitions, let's analyse the measurement outcomes in Fig. 2.2(b) more carefully. From that figure, we see that outcomes $2J_Z \geq n$ correspond to the alive state $\rho_A$ while outcomes $2J_Z \leq -n$ correspond to the dead state $\rho_D$. In the intermediate region, there are outcomes that cannot be binned into either dead or alive. Let $\rho_{DS}$ be a (quantum) state with possible outcomes of $2J_z$ that are smaller than $n$; while $\rho_{SA}$ is a (quantum) state with possible outcomes of $2J_z$ that are larger than $-n$. It is possible that the state of the system can be expressed as a mixture such that

$$\rho_{mix} = P_- \rho_{DS} + P_+ \rho_{SA}\,, \tag{2.11}$$

where $P_-$ and $P_+$ are probabilities for the system to be in the states $\rho_{DS}$ and $\rho_{SA}$, respectively, with $P_- + P_+ = 1$. If the state of the system cannot be expressed in the form given in Eq. (2.11), then it has $n$-scopic quantum coherence. However, we cannot determine this from the measurement outcomes plotted in Fig. 2.2. In other words, we are yet to determine the value $n$ in that figure. We need criteria to certify the presence of $n$-scopic quantum coherence. A particular criterion is presented next.

### 2.2.1 Existence of quantum coherence and correlation test

Having defined and discussed the notion of $n$-scopic quantum coherence, we look at a particular observable and what criterion it should satisfy to certify the presence of $n$-scopic quantum coherence in a nonideal NOON state. Here, we show that

$$\langle \hat{a}^{\dagger n} \hat{b}^n \rangle \neq 0 \tag{2.12}$$

implies the existence of $n$-scopic quantum coherence. It is straightforward to show that a nonzero $\langle \hat{a}^{\dagger n}\hat{b}^{n}\rangle$ implies the existence of the quantum state of the form

$$|\psi_n\rangle = a^{(n)}_{n'm'}|n'\rangle|m'+n\rangle + b^{(n)}_{n'm'}|n'+n\rangle|m'\rangle + d|\psi_0\rangle\,, \tag{2.13}$$

where $a^{(n)}_{n'm'}, b^{(n)}_{n'm'}, d$ are probability amplitudes satisfying $a^{(n)}_{n'm'}, b^{(n)}_{n'm'} \neq 0$ and $d$ corresponds to a quantum state orthogonal to the states $|n'\rangle|m'+n\rangle$ and $|n'+n\rangle|m'\rangle$. Note that this state in Eq. (2.13) satisfies

$${}_b\langle n+m'|_a\langle n'|\rho|n+n'\rangle_a|m'\rangle_b \neq 0\,, \tag{2.14}$$

which implies the existence of $n$-scopic quantum coherence as described in Section 2.2. This inference is based on the fact that nonzero off-diagonal terms in a density operator imply the presence of quantum coherence in a physical state. Hence, the observable $\langle \hat{a}^{\dagger n}\hat{b}^{n}\rangle$ is a measure of $n$-scopic quantum coherence.

We discuss how $\langle \hat{a}^{\dagger n}\hat{b}^{n}\rangle$, which is not Hermitian, can be inferred in an experiment. Let's first consider the case for $n = 1$. We carry out optical operations on the two modes $\hat{a}$ and $\hat{b}$. In particular, we include a phase shifter which shifts the phase of mode $\hat{b}$ by $\phi$. These two modes $\hat{a}$ and $\hat{b}$ are then sent into a $50:50$ beam splitter, with the corresponding output modes $\hat{c}$ and $\hat{d}$ as follows:

$$\begin{aligned}\hat{c} &= \frac{1}{\sqrt{2}}\left(\hat{a}+\hat{b}e^{i\phi}\right)\\ \hat{d} &= \frac{1}{\sqrt{2}}\left(\hat{a}-\hat{b}e^{i\phi}\right).\end{aligned} \tag{2.15}$$

Finally, we measure the output number/intensity difference $I_D$:

$$\begin{aligned}I_D &= \hat{c}^{\dagger}\hat{c} - \hat{d}^{\dagger}\hat{d}\\ &= \hat{a}^{\dagger}\hat{b}e^{i\phi} + \hat{a}\hat{b}^{\dagger}e^{-i\phi}\\ &= 2\hat{J}_X\cos\phi - 2\hat{J}_Y\sin\phi\,,\end{aligned} \tag{2.16}$$

where $\hat{J}_X = \left(\hat{a}^{\dagger}\hat{b}+\hat{a}\hat{b}^{\dagger}\right)/2$ and $\hat{J}_Y = \left(\hat{a}^{\dagger}\hat{b}-\hat{a}\hat{b}^{\dagger}\right)/2i$ are the Schwinger operators and they can be measured in experiments. By choosing $\phi$, we can choose to measure $\hat{J}_X$ or $\hat{J}_Y$. For $\phi = 0$, $\hat{J}_X$ is measured while for $\phi = -\frac{\pi}{2}$, $\hat{J}_Y$ is measured. Measurements with two values of the phase $\phi = 0, -\frac{\pi}{2}$ can then be used to deduce $\langle \hat{a}^{\dagger}\hat{b}\rangle$, where $\langle \hat{a}^{\dagger}\hat{b}\rangle = \langle \hat{J}_X\rangle + i\langle \hat{J}_Y\rangle$.

Next, for $n = 2$, we carry out the same optical operations, except that we measure the second order intensity moments of the output modes, rather than the first order intensity moments. In this case, we take the sum of the normally ordered, second order output intensities $I_S^{(2)}$:

$$\begin{aligned} I_S^{(2)} &= \hat{c}^{\dagger 2}\hat{c}^2 + \hat{d}^{\dagger 2}\hat{d}^2 \\ &= \hat{a}^{\dagger 2}\hat{a}^2 + 4\hat{a}^\dagger\hat{b}^\dagger\hat{a}\hat{b} + \hat{b}^{\dagger 2}\hat{b}^2 + \hat{a}^{\dagger 2}\hat{b}^2 e^{2i\phi} + \hat{a}^2\hat{b}^{\dagger 2}e^{-2i\phi}\,. \end{aligned} \tag{2.17}$$

The first three terms are second-order intensity moments that are accessible in experiments. Again, we can choose the phase $\phi$ and subsequently deduce $\langle \hat{a}^{\dagger 2}\hat{b}^2 \rangle$. Another possible approach is to measure the normally ordered, second order output intensity of one of the output modes, say $c^{\dagger 2}c^2$. This quantity has the term $a^{\dagger 2}b^2$ which oscillates with $e^{2i\phi}$. By measuring $c^{\dagger 2}c^2$ for a set of many different $\phi$ values, an observation of oscillation in $c^{\dagger 2}c^2$ with frequency $\frac{2}{2\pi} = \frac{1}{\pi}$ implies the presence of second order quantum coherence.

Hence, in order to measure $\langle \hat{a}^{\dagger n}\hat{b}^n \rangle$, first apply a phase shift to one of the modes and send both modes into a beam splitter, before measuring the sum or difference of the corresponding $n$-th order intensity moments of the output modes from the beam splitter. Another approach would be to measure the normally ordered, $n$-th order output intensity for a set of many different phase $\phi$ and infer from the oscillating frequency the order of quantum coherence.

In this subsection, we consider a test that demonstrates the existence of quantum coherence. Next, we take a step further in our investigation of quantum coherence by attempting to quantify the quantum coherence in a given quantum state.

### 2.2.2 Quantification of quantum coherence and catness fidelity

The correlation test presented in the previous section demonstrates whether quantum coherence exists or not. As described in that section, nonzero $\langle \hat{a}^{\dagger n}\hat{b}^n \rangle$ implies the existence of quantum coherence in a quantum state in Eq. (2.13) of the form

$$|\psi_n\rangle = a^{(n)}_{n'm'}|n'\rangle|m'+n\rangle + b^{(n)}_{n'm'}|n'+n\rangle|m'\rangle + d|\psi_0\rangle\,.$$

The correlation test, however, does not quantify the magnitude of the quantum coherence and does not provide the information on the probability amplitudes $a^{(n)}_{n'm'}$ and $b^{(n)}_{n'm'}$ for specific $n'$ and $m'$. These probability amplitudes are needed if we want to know the fidelity, i.e. how close is a given quantum

state to a reference state such as the NOON state. To this end, we analyse the fidelity and determine from the analysis how quantum coherence is defined. In the following, we consider the fidelity of the state $|\psi_n\rangle$ with respect to a specific $n$-scopic superposition quantum state

$$|\psi_{\text{sup}}\rangle = \frac{1}{\sqrt{2}}(|n'\rangle|m'+n\rangle + e^{i\phi}|n'+n\rangle|m'\rangle)\,. \tag{2.18}$$

The fidelity $F$ is given by

$$\begin{aligned} F &= \left|\langle\psi_{\text{sup}}|\psi_n\rangle\right|^2 \\ &= \frac{1}{2}\left(|a^{(n)}_{n'm'}|^2 + |b^{(n)}_{n'm'}|^2 + 2|a^{(n)}_{n'm'}b^{(n)*}_{n'm'}|\right) \end{aligned} \tag{2.19}$$

and it is one if and only if $|\psi_n\rangle$ is identical to $|\psi_{sup}\rangle$. We know that the $n$-scopic quantum coherence manifests itself in the off-diagonal elements of the corresponding density operator. For the state $|\psi_n\rangle$, we have the off-diagonal element

$$\langle n+m'|\langle n'|\rho|n+n'\rangle|m'\rangle = a^{(n)}_{n'm'}b^{(n)*}_{n'm'}\,. \tag{2.20}$$

We can then define the magnitude of $n$-scopic quantum coherence $C_n^{(n',m')}$ as

$$\begin{aligned} C_n^{(n',m')} &= 2|\langle m'+n|\langle n'|\rho|n+n'\rangle|m'\rangle| \\ &= 2|a^{(n)}_{n'm'}b^{(n)*}_{n'm'}|\,, \end{aligned} \tag{2.21}$$

which is exactly the third term in Eq. (2.19). In other words, the third term in the last line in Eq. (2.19) is related to the $n$-scopic quantum coherence of a quantum state. We see that the fidelity $F$ in Eq. (2.19) is 1 if and only if $a^{(n)}_{n'm'}b^{(n)*}_{n'm'} = 1/2$, which implies that $C_n^{(n',m')} = 1$. Also, $C_n^{(n',m')} = 1$ implies $F = 1$. Not surprisingly, this tells us that the fidelity of a given quantum state with respect to a reference quantum state with $n$-scsopic quantum coherence is related to the magnitude of $n$-scopic quantum coherence of the given quantum state. All these suggest that we may identify $n$-scopic quantum coherence with fidelity. We take this approach for the rest of this chapter. Note, however, that $n$-scopic quantum coherence is a property of a given physical state, while the fidelity is a property of that given state with respect to a reference state. To avoid confusion, the reference state always has to be explicitly stated.

What is less trivial is how the fidelity of a given quantum state with respect to a reference quantum

state, that contains $n$-scopic quantum coherence from superposition of states over different $n'$ and $m'$, is related to the $n$-scopic quantum coherence $C_n^{(n',m')}$. These are the states where different values of $n'$ and $m'$ each contributes to the total $n$-scopic quantum coherence. One may define the total $n$-scopic quantum coherence/total "$n$-scopic fidelity" as the sum of the magnitudes of each of the $n$-scopic quantum coherences i.e.

$$C_n = \mathscr{N} \sum_{n',m'} C_n^{(n',m')} = 2\mathscr{N} \sum_{n',m'} |a_{n'm'}^{(n)} b_{n'm'}^{(n)*}|\,, \tag{2.22}$$

where $\mathscr{N}$ is a normalisation factor that ensures the maximum value of $C_n$ is 1. If we can infer the probability amplitudes $a_{n'm'}^{(n)}$ and $b_{n'm'}^{(n)}$ for specific $n'$ and $m'$ from probabilities of measuring the mode number $n'$ and $m'$ for modes $a$ and $b$, respectively, then we can deduce the fidelity. We will look at a few quantum states and compute their $n$-scopic fidelity $C_n$. We should mention that the second equality in Eq. (2.22) holds true only for a pure quantum state, which is almost always not the case in practice. For a mixed state with density operator $\rho$, the $n$-scopic catness fidelity

$$\begin{aligned} C_n &= \mathscr{N} \sum_{n',m'} C_n^{(n',m')} \\ &= 2\mathscr{N} \sum_{n',m'} |\langle m'+n|\langle n'|\rho|n+n'\rangle|m'\rangle| \end{aligned} \tag{2.23}$$

has to be computed.

Before computing $C_n$ for a few quantum states, we would like to find out more about $C_n$. In particular, we try to relate $C_n$ to the quantity $\langle \hat{a}^{\dagger n}\hat{b}^n\rangle$, which we described in Section 2.2.1. There are two reasons for this. Firstly, $\langle \hat{a}^{\dagger n}\hat{b}^n\rangle$ is measurable in experiments. Also, this gives a lower bound to the $n$-scopic catness fidelity $C_n$. This provides important insight as many quantum information protocols require the fidelity to be above certain value to work. In the following, we establish the fact that $\langle \hat{a}^{\dagger n}\hat{b}^n\rangle$ is the lower bound of the $n$-scopic catness fidelity $C_n$. To do that, we derive the expressions for $\langle \hat{a}^{\dagger n}\hat{b}^n\rangle$ for both the pure and mixed states, and relate this to the $n$-scopic catness fidelity $C_n$.

For an $n$-scopic quantum state of the form

$$|\psi\rangle = \sum_{n',m'} a_{n'm'}^{(n)} |n'\rangle|m'+n\rangle + b_{n'm'}^{(n)} |n'+n\rangle|m'\rangle\,, \tag{2.24}$$

the quantity $\langle \hat{a}^{\dagger n}\hat{b}^{n}\rangle$ has the expression

$$\langle \hat{a}^{\dagger n}\hat{b}^{n}\rangle = \sum_{n',m'\geq 0} a^{(n)}_{n'm'} b^{(n)*}_{n'm'} \sqrt{\frac{(m'+n)!}{m'!}} \sqrt{\frac{(n'+n)!}{n'!}}. \tag{2.25}$$

Note the presence of $a^{(n)}_{n'm'} b^{(n)*}_{n'm'}$, which is related to the magnitude of $n$-scopic quantum coherence $C_n^{(n',m')}$ in Eq. (2.21) for a specific $n'$ and $m'$.

For a general two-mode mixed state, the quantity $\langle \hat{a}^{\dagger n}\hat{b}^{n}\rangle$ is calculated with the corresponding density operator as follows:

$$\begin{aligned}
\langle \hat{a}^{\dagger n}\hat{b}^{n}\rangle &= \mathrm{Tr}(\rho a^{\dagger n} b^{n}) \\
&= \sum_{n',m'\geq 0} \langle n'|\langle m'+n|\rho a^{\dagger n} b^{n}|n'+n\rangle|m'\rangle \\
&= \sum_{n',m'\geq 0} \sqrt{\frac{(n'+n)!}{n'!}} \sqrt{\frac{(m'+n)!}{m'!}} \langle n'|\langle m'+n|\rho|n'+n\rangle|m'\rangle .
\end{aligned} \tag{2.26}$$

Recall that $C_n^{(n',m')} = 2|\langle n'|\langle m'+n|\rho|n'+n\rangle|m'\rangle|$. We now relate $\langle \hat{a}^{\dagger n}\hat{b}^{n}\rangle$ and the $n$-scopic quantum coherence $C_n$. Using Eq. (2.26), the lower bound for $n$-scopic catness fidelity $C_n$ can be found easily, as derived below:

$$\begin{aligned}
\langle \hat{a}^{\dagger n}\hat{b}^{n}\rangle &= \sum_{n',m'\geq 0} \sqrt{\frac{(n'+n)!}{n'!}} \sqrt{\frac{(m'+n)!}{m'!}} \langle n'|\langle m'+n|\rho|n'+n\rangle|m'\rangle \\
&\leq S \sum_{n',m'\geq 0} \langle n'|\langle m'+n|\rho|n'+n\rangle|m'\rangle \\
&= S\frac{C_n}{2},
\end{aligned} \tag{2.27}$$

where $S = sup_{n',m'}\{\sqrt{\frac{(m'+n)!}{m'!}}\sqrt{\frac{(n'+n)!}{n'!}}\}$ is the largest value of $\sqrt{\frac{(m'+n)!}{m'!}}\sqrt{\frac{(n'+n)!}{n'!}}$ over values of $n'$, $m'$. Hence, the lower bound for $C_n$ is given by

$$C_n \geq \frac{2\left|\langle \hat{a}^{\dagger n}\hat{b}^{n}\rangle\right|}{S} \equiv c_n . \tag{2.28}$$

To this end, the quantity $\langle \hat{a}^{\dagger n}\hat{b}^{n}\rangle$ not only allows us to certify $n$-scopic quantum coherence, but also quantifies it, as shown in Eq. (2.28). Next, we consider a few examples of quantum states and compute

their corresponding catness fidelities $C_n$ and lower bounds $c_n$.

#### 2.2.2.1 Ideal NOON state

Suppose one finds in an experiment that measurement outcomes are either $N$ particles in mode $a$ or $N$ particles in mode $b$. Then, the best guess of the corresponding density operator has the form

$$\rho = P_N \rho_N + P_{alt} \rho_{alt} \,, \tag{2.29}$$

where $\rho_N$ is the density operator of a NOON state given in Eq. (2.24) with $n', m' = 0$, and $\rho_{alt}$ is the density operator of a statistical mixture of $|N0\rangle$ and $|0N\rangle$ states. $P_N$ and $P_{alt}$ are the probabilities of the density operators $\rho_N$ and $\rho_{alt}$, respectively. In other words, the system could be in an ideal NOON state, a statistical mixture of $|N0\rangle$ and $|0N\rangle$ states or both, with probabilities $P_N$ and $P_{alt}$.

Let's begin with the $N$-scopic quantum coherence, $C_N$, which is also identified as the catness fidelity as described in the previous section.

$$\begin{aligned} C_N &= 2\left|\langle N0|\rho|0N\rangle\right| \\ &= 2P_N \left| a_{00}^{(N)} b_{00}^{(N)*} \right| . \end{aligned} \tag{2.30}$$

This picks up the NOON superposition state with probability $P_N$. $C_N$ would be zero if the density operator is just the statistical mixture of $|N0\rangle$ and $|0N\rangle$ states.

Recall also that the quantity $\langle \hat{a}^{\dagger N} \hat{b}^N \rangle \neq 0$ certifies $N$-scopic quantum coherence. We compute this below:

$$\begin{aligned} \langle \hat{a}^{\dagger N} \hat{b}^N \rangle &= \mathrm{Tr}\left(\rho \hat{a}^{\dagger N} \hat{b}^N\right) \\ &= P_N N! a_{00}^{(N)} b_{00}^{(N)*} . \end{aligned} \tag{2.31}$$

Again, we see that there is no $N$-scopic quantum coherence if $P_N = 0$. Using Eq. (2.31), we can compute the lower bound of $C_N$ as described in Eq. (2.28).

$$\begin{aligned} c_n &= \frac{2\left|\langle \hat{a}^{\dagger n} \hat{b}^n \rangle\right|}{S} \\ &= 2P_N \left| a_{00}^{(N)} b_{00}^{(N)*} \right| , \end{aligned} \tag{2.32}$$

where $S = N!$. The lower bound of $C_N$ coincides with $C_N$ in the case of ideal NOON state. For a pure ideal NOON state, $C_N = 1$. This will obviously not be the case when we take into account losses in the system. In the next example, we consider an attenuated NOON state due to losses and we shall see how the catness fidelity $C_N$ changes with the degree of losses and also how the particle number plays a role.

#### 2.2.2.2 Attenuated NOON state

We model the losses with beam splitter, as described in Section 1.5. The detected output modes $\hat{a}_{det}$ and $\hat{b}_{det}$ are expressed in terms of the non-attenuated modes $\hat{a}$ and $\hat{b}$. In other words, the losses are modeled as inefficiency in the detection process. These detected output modes are

$$\begin{aligned} \hat{a}_{det} &= \sqrt{\eta}\hat{a} + \sqrt{1-\eta}\hat{a}_v \\ \hat{b}_{det} &= \sqrt{\eta}\hat{b} + \sqrt{1-\eta}\hat{b}_v\,, \end{aligned} \tag{2.33}$$

where $\hat{a}_v$ and $\hat{b}_v$ are vacuum modes entering into the beam splitter, and $\eta$ is the transmissivity of the beam splitter and it represents the probability of detection of particle/photon in a specific mode. To demonstrate the effect of losses on an ideal NOON state, we assume the density operator before the detection to be $\rho_N$, i.e. $P_N = 1$ and $P_{alt} = 0$ in Eq. (2.29). The quantity $\langle \hat{a}_{det}^{\dagger n} \hat{b}_{det}^{n} \rangle$ is found to be

$$\langle \hat{a}_{det}^{\dagger n} \hat{b}_{det}^{n} \rangle = \eta^n \langle \hat{a}^{\dagger n} \hat{b}^n \rangle = \eta^n \delta_{nN} N!/2\,, \tag{2.34}$$

giving the lower bound of catness fidelity

$$c_N = \eta^N\,. \tag{2.35}$$

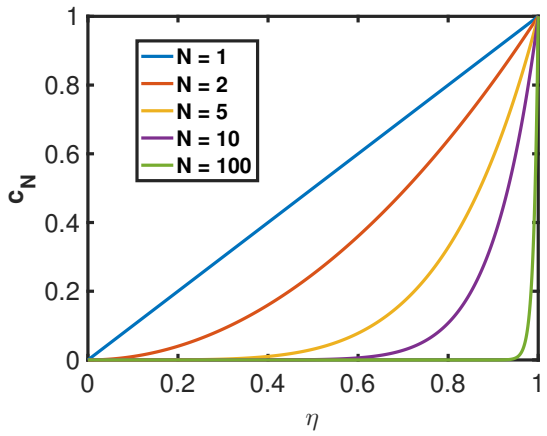


Figure 2.3: $N$-th order catness fidelity for attenuated NOON states as a function of detection efficiency $\eta$.

The catness fidelity is plotted as a function of the probability of detecting the modes $\hat{a}$ and $\hat{b}$, for different particle numbers, in Fig. 2.3. As expected, the fidelity reduces with losses and the reduction is much more dramatic for high particle number. Recall that for high particle number $N$, a NOON state is a Schrodinger's cat state, and it is known that a cat state (and its quantum superposition and coherence) is more susceptible to noise and loss. In fact, this is the best explanation we have so far in explaining the absence of a cat that is in a superposition of being dead and alive: they are just too delicate to exist.

#### 2.2.2.3 Experimentally Realisable States

In the previous two examples, the lower bound of $c_n$ coincides with the catness fidelity $C_n$. This is because the state contains superposition of just two states, $|N0\rangle$ and $|0N\rangle$. Also, the fidelities are computed with respect to a NOON state with $N$-scopic quantum coherence, which has a normalisation factor $\mathscr{N}$ of 2. In this example, we will consider pure quantum states with $n$-scopic quantum coherence as the reference states for the fidelity computations. This means that the normalisation factor in the catness fidelity lower bound will be different from the normalisation factor where we assume ideal NOON state as the reference state. But first, we describe the quantum state of our example:

$$|out\rangle = \sum_{m=0}^{N} d_m |m\rangle_a |N-m\rangle_b \,, \tag{2.36}$$

where $d_m = \sqrt{N!}/\sqrt{2^N m!(N-m)!}$ is the probability amplitude of $m$ mode number in mode $a$ and it is a binomial coefficient. The state $|out\rangle$ can be generated by sending a two-mode number state $|N0\rangle_{ab}$ into two input ports of a beam splitter.

Unlike the ideal and attenuated NOON states, the quantity $\langle \hat{a}^{\dagger m}\hat{b}^m\rangle$ is not zero for $m \neq N$. This complicates the calculation of catness fidelity slightly. The total $n$-scopic catness fidelity for the quantum state $|out\rangle$ is

$$C_n = \mathscr{N}_{n,N} \sum_{m=0}^{N-n} |d_m d_{m+n}^*|\,, \tag{2.37}$$

where $\mathscr{N}_{n,N}$ is a normalisation constant to ensure the maximum value of $C_n$ is 1. To ensure that, we choose quantum states that has the corresponding maximum $n$-scopic quantum coherence. This also implies that the corresponding fidelity is computed with respect to that quantum state with the maximum $n$-scopic quantum coherence. For this system, the normalisation $\mathscr{N}_{n,N}$ is determined by the bounds on the coherences of the density matrix for a pure state. For example, where $n = N$, $d_0 d_N^* \leq 1/2$ and hence $\mathscr{N}_{N,N} = 2$. The general result for the normalisation $\mathscr{N}_{n,N}$ can be obtained numerically and is not provided here. The purpose of the discussion on the normalisation factor is to make clear the fact that we are comparing quantum states of the form given in Eq. (2.36) with a pure quantum state with the corresponding $n$-scopic quantum coherence. The lower bound to the catness-fidelity is

$$c_n = \frac{\mathscr{N}_{n,N}|\langle a^{\dagger n} b^n\rangle|}{S}\,, \tag{2.38}$$

where $S = \max\{B_m^{(N,n)}\}$ is given by Eq. (2.27) with $m' = m$ and $n' = N-m-n$ and

$$B_m^{(N,n)} = \sqrt{\frac{(m+n)!\,(N-m)!}{m!\,(N-m-n)!}}\,. \tag{2.39}$$

The value of $m$ that gives the maximum value of $B_m^{(N,n)}$ is given by: $m = (N-n)/2$ if $N$ and $n$ have the same parity, i.e. $N$ and $n$ are either even or odd numbers, and $m = (N-n\pm 1)/2$ if $n$ and $N$ does not have the same parity.

## 2.3 Summary and outlook

We considered the NOON state, which is a Schrodinger's cat state for large $N$. In Section 2.1, we derived steering inequalities that certify the existence of EPR steering in NOON states. These inequalities were also applied to attenuated NOON states to study the effect of losses on EPR-steering on NOON states. These steering inequalities for $N > 1$ extend the proposals of Jones et al. [114] and the experiment of Fuwa et al. [115] that investigate steering and collapse of the wavefunction for the state given by $N = 1$.

Even though steering inequalities are useful in certifying the quantum correlations in NOON states, they do not provide information on how these quantum correlations arose. The quantum correlations in NOON states come from the fact that it is a quantum superposition of states and not just classical, statistical mixture of these states. In other words, the quantum coherence of a quantum state is the source of its quantum correlations. In Section 2.2, we defined the notion of quantum coherence and more generally, the $n$-scopic quantum coherence. With these definitions, we looked at a specific correlation test to verify the presence of $n$-scopic quantum coherence in a given state. The correlation test involves the observable $\langle \hat{a}^{\dagger n} \hat{b}^n \rangle$ that can be and has been measured in experiments [116–123].

In a typical quantum information protocol involving quantum states with quantum correlations, it is inevitable that the quantum states will be affected by losses and noises from the environment. This might destroy the quantum coherence of the quantum state and hence its quantum correlations. It is then essential to be able to tell how "close" a quantum state is with respect to another quantum state. One of the possible measures is the fidelity. In Section 2.2.2, we demonstrated the connection between quantum coherence of a NOON state and the catness fidelity. We also showed that the lower bound of the catness fidelity can be estimated using the observable $\langle \hat{a}^{\dagger n} \hat{b}^n \rangle$. It is useful to compute the lower bound of the fidelity. For instance, in order to have a quantum memory, there is a minimal fidelity that the system has to achieve.

Finally, we considered a few examples of quantum states and computed their corresponding catness fidelity and their lower bound. The quantum state in Eq. (2.36) can be generated by sending a number state into a beam splitter. This is a good model for realistic physical systems, for example, a photonic number state can be prepared from the twin beams of a parametric down conversion. NOON states have been created in the experiments of [118, 119, 121–124].

The relevant publications to this chapter are:

- R. Y. Teh, L. Rosales-Zárate, B. Opanchuk, and M. D. Reid, *Signifying the nonlocality of NOON states using Einstein-Podolsky-Rosen steering inequalities*, Phys. Rev. A **94**, 042119 (2016).

- B. Opanchuk, L. Rosales-Zárate, R. Y. Teh, and M. D. Reid, *Quantifying the mesoscopic quantum coherence of approximate NOON states and spin-squeezed two-mode Bose-Einstein condensates*, Phys. Rev. A **94**, 062125 (2016).

# Part III

# Quantum correlations in mesoscopic systems: optomechanics

We investigated quantum correlations such as the quantum entanglement and EPR steering in the continuous variables of quantum optical systems. The effects of decoherence on quantum correlations, treated using beam splitter operations, are also studied in previous chapters. In the second part of the thesis, we study quantum mechanics in mesoscopic or macroscopic systems. In particular, we consider optomechanical systems where recent experiments in the field of optomechanics have demonstrated quantum effects including ground state cooling of the mechanical mode, coherent state transfer and quantum entanglement generations. As is well-known, any quantum features in a macroscopic system are extremely sensitive to the interaction with its environment. This interaction manifests itself in the fluctuation and dissipation of the macroscopic system under study. We treat them with the standard open system formalism in the form of a master equation.

In this part of the thesis, we first describe a typical quantum optomechanical system and consider its dynamics using the linearisation approximation which simplifies the analyses. The purpose of this is to gain some understanding on how a quantum optomechanical system behaves. The full, nonlinear quantum optomechanical system and its dynamics are studied in detail in later chapters. Operators are needed to characterise a quantum optomechanical system, and its dynamics inevitably involves solving operator equations with nonlinearity. These operator equations are impossible to solve in general. Phase space methods map these operator equations into complex number equations, which can be solved numerically.

Approximations such as linearisation and adiabaticity are often employed in both the experimental and theoretical analyses in the literature. The validity of these approximations will be discussed. Using phase space methods, these approximations are not needed and the full, nonlinear dynamics of the optomechanics can be simulated. These simulations are also extensible, allowing us to study more complex quantum optomechanical systems involving more subsystems. Hence, we take a detour to present the phase space methods that will be used to simulate the dynamics of optomechanical systems. All these are to be found in Chapter 3. We then analyse two specific quantum protocols: optomechanical quantum memory and entanglement between two optomechanical systems. In Chapter 4, we look at the optomechanical quantum memory of coherent states. Finally, we investigate the feasibility of quantum entanglement between two optomechanical systems in Chapter 5.

# Chapter 3

# Quantum mechanics of optomechanical systems

The quantum optomechanical system is first described in Section 3.1; the optical and mechanical systems, with the interaction between them. The Hamiltonian describing the quantum optomechanical system, including external coherent fields, thermal noises and losses are given. The fluctuations and dissipations in the system are dealt with in the master equation formalism. In Section 3.2, we introduce the linearisation approximation that simplifies the optomechanical Hamiltonian and the corresponding linearised dynamics. We explicitly derive this simplified Hamiltonian to demonstrate the quantum protocols that can be carried out in an optomechanical system. We then return to the master equation and motivate the use of phase space methods as a way to solve for the dynamics of the optomechanical system. This is discussed in Section 3.3.

## 3.1 Quantum optomechanical system

A prototypical quantum optomechanical system consists of a Fabry-Perot cavity which allows certain optical modes to exist in it. One of the mirrors is movable and is treated as the mechanical mode. The interactions between the optical mode and the mechanical mode are due to the radiation pressure force, where photons in the cavity impart momentum on the mechanical mode. The mechanical mode will, in turn, change the resonance frequency of the cavity and hence the amplitude of the optical mode.

Both the optical and mechanical modes are modelled by quantum harmonic oscillators and are described by bosonic operators satisfying the canonical bosonic commutation relations. Excitations of

the optical and mechanical modes are the photons and phonons respectively. The Hamiltonian for a quantum optomechanical system is given by

$$H = \hbar\omega_c a^\dagger a + \hbar\omega_m b^\dagger b + \hbar g_0 a^\dagger a \left(b + b^\dagger\right), \tag{3.1}$$

where the first two terms are the free Hamiltonian for the optical and mechanical modes respectively and the last term describes the interaction between these modes due to radiation pressure. Here, $g_0$ is known as the single photon optomechanical coupling strength and has the dimension of frequency. It quantifies the interaction strength between a single photon and a single phonon [68]. Even though we consider an optomechanical system using a Fabry-Perot cavity, there are many implementations employing different systems that share the same Hamiltonian (3.1).

Under what conditions do we need the quantum mechanical description of the optomechanical systems? For one thing, quantum description is required if we are able to put the optomechanical system in its ground state. This has practical usage too, for instance, in the initialisation of the system for any quantum protocol. The quantum ground state of an optomechanical system has been achieved [50, 53, 125, 126]. Secondly, the system has to allow quantum states. This is routinely achieved in quantum optics. It is much harder for a mechanical quantum state as it is interacting with its environment, introducing noises that destroy any quantum superposition and quantum coherence in the mechanical quantum state. The decoherence of a mechanical quantum state is determined by the decoherence rate, which is typically defined as the rate for an excitation to enter from the environment [68]. This quantity depends on the decay rate of the mechanical system and also the mean occupation number due to its interaction with the environment at a fixed temperature. Experiments have achieved both low mechanical dissipation rate and cool environment temperature for the mechanical oscillator to behave quantum mechanically.

It is instructive to look at the eigenvalues and eigenstates for the Hamiltonian in Eq. (3.1). They are obtained in the theoretical work by Liao et. al [127] and are given by

$$H|m\rangle_a|\tilde{n}(m)\rangle_b = \hbar\left(m\omega_c + n\omega_m + m^2 g_0^2/\omega_m\right)|m\rangle_a|\tilde{n}(m)\rangle_b, \tag{3.2}$$

where $m$ and $n$ are the photon and phonon numbers respectively and $|\tilde{n}(m)\rangle = exp\left[\frac{mg_0}{\omega_m}\left(b^\dagger - b\right)\right]|n\rangle$ is a displaced number state of the mechanical mode by $m$ photons. The energy levels of the total optomechanical system still resemble that of a quantum harmonic oscillator. For weak coupling strength where

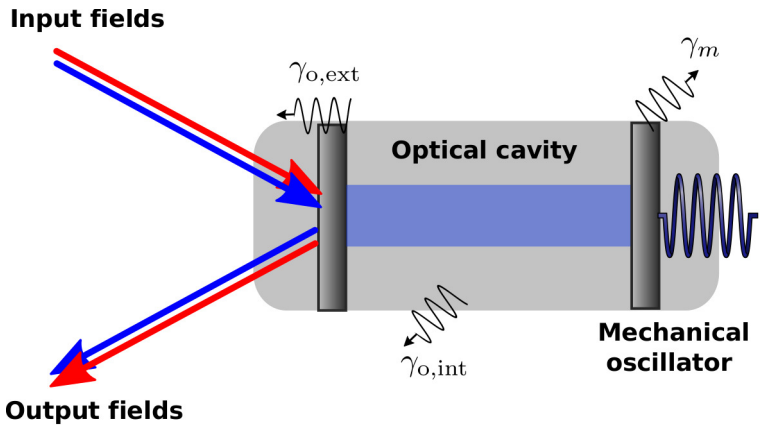


Figure 3.1: The prototypical quantum optomechanical setup.

$g_0$ is small, the energy levels of the optomechanical system are essentially the sum of two independent quantum harmonic oscillators. The Hamiltonian (3.1), however, is incomplete for a practical reason. In most experimental implementations of the quantum optomechanical system, the optomechanical coupling strength $g_0$ is weak. One or more intense, coherent external fields are typically used to enhance the coupling strength. This introduces extra terms in the Hamiltonian and the eigenstates of this new Hamiltonian will not be those given in Eq. (3.2).

Besides, there are always interactions with the environment that give rise to dissipations and fluctuations in the quantum optomechanical systems. Also, external driving fields can be applied to generate certain desired quantum states of the optical mode and carry out certain quantum protocols, further complicating the Hamiltonian needed to describe the system. A more general Hamiltonian is then

$$H = \hbar\omega_c a^\dagger a + \hbar\omega_m b^\dagger b + \hbar g_0 a^\dagger a\left(b + b^\dagger\right) + i\hbar E(t)\left[-ae^{i\omega_d t} + a^\dagger e^{-i\omega_d t}\right] + H_R\,, \tag{3.3}$$

where the fourth term includes all external driving fields and the last term describes the coupling between the optomechanical system and its environment. The coupling between the optomechanical system to its environment introduces decay channels with their corresponding decay rates. We denote $\gamma_o$ and $\gamma_m$ to be the cavity decay rate and mechanical dissipation rate respectively. We further distinguish two contributions to the cavity decay rate that corresponds to different sources of losses, $\gamma_o = \gamma_{o,ext} + \gamma_{o,int}$. The external cavity decay rate $\gamma_{o,ext}$ comes from the cavity field leaking out of the cavity while the internal cavity decay rate $\gamma_{o,int}$ includes all sources of dissipation in the cavity. This

distinction is important as it is the external cavity decay that allows the photons that contain information about the physical state of the optical mode to be detected. The internal cavity losses are undetected.

A quantum system that interacts with its environment is an open quantum system and one of the standard methods in describing an open quantum system is the master equation formalism. The master equation dictates the time evolution of a density operator and this is a Schrodinger picture formalism. We will not delve into the details of the master equation approach but rather refer readers to literature with extensive analyses and discussions [77, 78, 128]. Assuming interactions with the environment to be Markovian, the master equation for an open quantum system is [128]

$$\frac{d}{dt}\rho = -\frac{i}{\hbar}[H,\rho] + \sum_j \gamma_j \bar{n}_j \left(2a_j^\dagger \rho a_j - a_j \rho a_j^\dagger - \rho a_j a_j^\dagger\right) + \sum_j \gamma_j (\bar{n}_j + 1)\left(2a_j \rho a_j^\dagger - a_j^\dagger a_j \rho - \rho a_j^\dagger a_j\right). \tag{3.4}$$

Here, $\rho$ is the density operator of the system. The index $j = 1, 2 \sim o, m$ refer to the cavity and mechanical modes respectively, and $\bar{n}_j$ are the average thermal occupation numbers from interactions with their corresponding reservoirs.

One can also approach the problem in the Heisenberg picture. An equivalent set of quantum Langevin equations can be derived from the master equation in Eq. (3.4). They dictate the time evolution of the cavity and mechanical mode amplitudes. In general, both the master equation and quantum Langevin equations cannot be solved analytically and numerical solutions are required. Before attempting to tackle these equations, we first consider the linearised quantum optomechanical Hamiltonian, which is an approximation widely used in the literature. This simplifies the analysis which permits the understanding of different physics in an optomechanical system. The origin and validity of the linearisation approximation are discussed in the next section.

## 3.2 Linearised quantum optomechanical Hamiltonian and its dynamics

In this section, we analyse and discuss the optomechanical system within the linearisation approximation. This approximation is often used in the literature, so it is worth going through the analysis carefully, to check for the validity of the approximation. The linearised scheme is also instructive in providing physical pictures on how quantum protocols work in optomechanics.

We start from the Hamiltonian (3.3) which includes the coupling between a single external driv-

ing field and the optical mode. For simplicity, we will neglect the interactions between the quantum optomechanical system and its environment. The Hamiltonian is then given by:

$$H = \hbar\omega_c a^\dagger a + \hbar\omega_m b^\dagger b + \hbar g_0 a^\dagger a \left(b + b^\dagger\right) + i\hbar E(t)\left[-ae^{i\omega_d t} + a^\dagger e^{-i\omega_d t}\right]. \tag{3.5}$$

It is convenient to transform the Hamiltonian into the rotating frame of the driving field as this eliminates the driving field time dependence. In the rotated frame, an important free parameter is the detuning between the driving field and the cavity optical field $\Delta \equiv \omega_c - \omega_d$. Different detuning $\Delta$ gives rise to different optomechanical dynamics. As we will see in the next section, this determines the nature of quantum protocols using quantum optomechanical systems. Also, from a practical point of view, transforming into the fast rotating frame allows better performance in numerical simulations. This removes the high frequency that would otherwise require much smaller step size in time in our simulations. We obtain the rotated frame Hamiltonian by applying the transformation

$$\tilde{H} = U^\dagger H U - A, \tag{3.6}$$

where $A = \hbar\omega_d a^\dagger a$ and $U = exp\left(-i\frac{t}{\hbar}A\right)$. This gives

$$\widetilde{H} = \hbar\Delta a^\dagger a + \hbar\omega_m b^\dagger b + \hbar g_0 a^\dagger a \left(b + b^\dagger\right) + i\hbar E(t)\left(-a + a^\dagger\right). \tag{3.7}$$

Here, $\Delta = \omega_c - \omega_d$ is the detuning between the cavity resonance frequency and the frequency of the driving field.

Next, we introduce the linearisation approximation. There are two ways to do this. One could invoke the approximation right away at the level of the Hamiltonian (3.7). Or one could obtain the equations of motion from the Hamiltonian (3.7) and only introduce the linearisation approximation in these dynamical equations. Both approaches are equivalent. Most literature pick the first approach as it makes clear an essential feature that allows different quantum protocols to be carried out. We will present both approaches, starting with the second approach because it is less tedious and provides a physical picture as to why this approximation is a good one. We then take the second approach, linearising the optomechanical Hamiltonian to demonstrate how different quantum protocols can be achieved.

### 3.2.1 Heisenberg equations of motion and their dynamics

Using the rotated frame Hamiltonian in Eq. (3.7) and the Heisenberg picture, the time evolution equations for both the optical $\hat{a}$ and mechanical $\hat{b}$ modes are given by

$$\dot{\hat{a}} = \frac{i}{\hbar}\left[\widetilde{H}, \hat{a}\right] = -i\Delta\hat{a} - ig_0\hat{a}\left(\hat{b} + \hat{b}^\dagger\right) + E(t) \tag{3.8}$$

$$\dot{\hat{b}} = \frac{i}{\hbar}\left[\widetilde{H}, \hat{b}\right] = -i\omega_m\hat{b} - ig_0\hat{a}^\dagger\hat{a}\,. \tag{3.9}$$

To this end, we introduce the linearisation approximation. It is based on the fact that an intense external field will dominate the amplitude of the optical mode, reaching a steady state amplitude in equilibrium. Any fluctuations around the steady state amplitude has a quantum nature and are described by quantum operators. We proceed to express both the optical and mechanical modes as a sum of classical steady state amplitude and fluctuations around this amplitude as follows:

$$\hat{a} = \alpha_{ss} + \hat{\delta a}(t) \tag{3.10}$$

$$\hat{b} = \beta_{ss} + \hat{\delta b}(t) \tag{3.11}$$

with the properties $\langle\hat{a}\rangle = \alpha_{ss}$ and $\langle\hat{b}\rangle = b_{ss}$. Replacing $\hat{a}$ and $\hat{b}$ in Eqs. (3.10) and (3.11) into Eqs. (3.8) and (3.9), we obtain

$$\begin{aligned}\frac{d}{dt}\hat{\delta a} &= E - i\Delta\left(\alpha_{ss} + \hat{\delta a}\right) - ig_0\left(\alpha_{ss} + \hat{\delta a}\right)\left(\beta_{ss} + \beta_{ss}^* + \hat{\delta b} + \hat{\delta b}^\dagger\right) \\ &= -i\left[\Delta + g_0 x_{ss}\right]\hat{\delta a} - ig_0\alpha_{ss}\hat{\delta x}\end{aligned} \tag{3.12}$$

and

$$\begin{aligned}\frac{d}{dt}\hat{\delta b} &= -i\omega_m\left(\beta_{ss} + \hat{\delta b}\right) - ig_0\left(\alpha_{ss}^* + \hat{\delta a}^\dagger\right)\left(\alpha_{ss} + \hat{\delta a}\right) \\ &= -i\omega_m\hat{\delta b} - ig_0\alpha_{ss}^*\hat{\delta a} - ig_0\alpha_{ss}\hat{\delta a}^\dagger\,.\end{aligned} \tag{3.13}$$

Expressing the optical and mechanical modes in the forms in Eqs. (3.10) and (3.11) amounts to using the linearisation approximation. Note that the time evolution equations in Eqs. (3.12) and (3.13) are now linear.

In going from the second to the third line in Eqs. (3.12) and (3.13), we neglect terms that are second

order in the fluctuating operators. Also, the steady state solutions are

$$\alpha_{ss} = \frac{E}{i\Delta + ig_0\left(\beta_{ss} + \beta_{ss}^*\right)} \tag{3.14}$$

$$\beta_{ss} = -\frac{ig_0\left|\alpha_{ss}\right|^2}{i\omega_m} = -\frac{g_0 N_d}{\omega_m}, \tag{3.15}$$

where $N_d = |\alpha_{ss}|^2$ is the mean intracavity photon number. From the solution in Eq. (3.14), we see that the cavity steady state amplitude is due to the external pump field $E$ as described previously. The external pump field is present in most of the experiments to date. This is because the single optomechanical coupling strength $g_0$ is weak and the pump enhances the coupling strength by a factor of $\alpha_{ss}$. Hence, the linearisation approximation appears to be a good one when an intense field is required to enhance the optomechanical coupling strength. We also see that the equilibrium displacement of the mechanical mode depends on the mean intracavity photon number and it is given by

$$\begin{aligned} x_{ss} &= \beta_{ss} + \beta_{ss}^* \\ &= -2\frac{g_0 N_d}{\omega_m}. \end{aligned} \tag{3.16}$$

Note, however, that the steady state solution of optical mode $\alpha_{ss}$ depends on $x_{ss}$. This leads to a cubic equation for $x_{ss}$ as a function of the intensity of the pump field $E$ [129], demonstrating bistability in the system [129, 130].

The linearisation approximation is used in most of the experiments carried out thus far as the single photon coupling strength $g_0$ is weak and an intense, coherent driving field is required to enhance the coupling strength. In the next section, we linearise the optomechanical Hamiltonian as this will make clear the quantum protocols such as quantum state transfer and quantum entanglement generation.

### 3.2.2 Linearised quantum optomechanical Hamiltonian

We linearise the Hamiltonian in Eq. (3.7) and show that quantum optomechanical interactions allow quantum state transfer and generation of quantum entanglement. As mentioned previously, the bare optomechanical coupling strength $g_0$ is usually very weak and a strong driving field is applied to enhance the coupling strength. This allows optical mode amplitude to be decomposed into two parts, the steady state amplitude and fluctuations around that amplitude. This decomposition is possible because

the cavity mode is dominated by the intense driving field as shown in Eq. (3.14). The mechanical mode is also decomposed similarly. Substituting $a = \alpha_{ss} + \delta a$ and $b = \beta_{ss} + \delta b$ into Eq. (3.7) gives

$$\begin{aligned} H &= \hbar\Delta\delta a^\dagger \delta a + \hbar\omega_m \delta b^\dagger \delta b + \hbar\Delta |\alpha_{ss}|^2 + \hbar\omega_m |\beta_{ss}|^2 \\ &+ \hbar g_0 |\alpha_{ss}|^2 (\beta_{ss} + \beta_{ss}^*) + \hbar g_0 \delta a^\dagger \delta a (\beta_{ss} + \beta_{ss}^*) + \hbar g_0 \delta a^\dagger \delta a \left(\delta b + \delta b^\dagger\right) \\ &+ \hbar g_0 \alpha_{ss} \delta a^\dagger \left(\delta b + \delta b^\dagger\right) + \hbar g_0 \alpha_{ss}^* \delta a \left(\delta b + \delta b^\dagger\right) \\ &+ \left[\hbar\Delta\alpha_{ss}^* + \hbar g_0 \alpha_{ss}^* (\beta_{ss} + \beta_{ss}^*) - i\hbar E\right] \delta a + \left[\hbar\Delta\alpha_{ss} + \hbar g_0 \alpha_{ss} (\beta_{ss} + \beta_{ss}^*) + i\hbar E\right] \delta a^\dagger \\ &+ \left[\hbar\omega_m \beta_{ss}^* + \hbar g_0 |\alpha_{ss}|^2\right] \delta b + \left[\hbar\omega_m \beta_{ss} + \hbar g_0 |\alpha_{ss}|^2\right] \delta b^\dagger . \end{aligned} \tag{3.17}$$

We choose to transform the optical and mechanical modes such that the steady state solutions are zero and hence obtaining a Hamiltonian that only consists of fluctuating terms. This is done by choosing

$$\begin{aligned} \alpha_{ss} &= -\frac{iE}{\Delta + g_0 (\beta_{ss} + \beta_{ss}^*)} \\ \beta_{ss} &= -\frac{g_0 |\alpha_{ss}|^2}{\omega_m} . \end{aligned} \tag{3.18}$$

The resulting Hamiltonian is then

$$\begin{aligned} H &= \hbar\Delta\delta a^\dagger \delta a + \hbar\omega_m \delta b^\dagger \delta b + \hbar\Delta |\alpha_{ss}|^2 + \hbar\omega_m |\beta_{ss}|^2 \\ &+ \hbar g_0 |\alpha_{ss}|^2 (\beta_{ss} + \beta_{ss}^*) + \hbar g_0 \delta a^\dagger \delta a (\beta_{ss} + \beta_{ss}^*) + \hbar g_0 \delta a^\dagger \delta a \left(\delta b + \delta b^\dagger\right) \\ &+ \hbar g_0 \alpha_{ss} \delta a^\dagger \left(\delta b + \delta b^\dagger\right) + \hbar g_0 \alpha_{ss}^* \delta a \left(\delta b + \delta b^\dagger\right) . \end{aligned} \tag{3.19}$$

We further neglect terms that do not depend on $\delta a$, $\delta a^\dagger$, $\delta b$ and $\delta b^\dagger$ since they do not contribute to the dynamics, and also neglect terms involving third order fluctuation operators.

$$H^{(2)} = \hbar \left[\Delta + g_0 (\beta_{ss} + \beta_{ss}^*)\right] \delta a^\dagger \delta a + \hbar\omega_m \delta b^\dagger \delta b + \hbar g_0 \left(\alpha_{ss}^* \delta a + \alpha_{ss} \delta a^\dagger\right) \left(\delta b + \delta b^\dagger\right) . \tag{3.20}$$

Redefining our detuning by introducing $\Delta' = \Delta + 2g_0\beta_{ss}$, the final form of linearised Hamiltonian is

given by

$$\begin{aligned} H^{(2)} &= \hbar\Delta'\delta a^\dagger\delta a + \hbar\omega_m\delta b^\dagger\delta b + \hbar g_0\left(\alpha_{ss}^*\delta a + \alpha_{ss}\delta a^\dagger\right)\left(\delta b + \delta b^\dagger\right) \\ &= \hbar\Delta'\delta a^\dagger\delta a + \hbar\omega_m\delta b^\dagger\delta b + \hbar\left(g^*\delta a\delta b + g^*\delta a\delta b^\dagger + g\delta a^\dagger\delta b + g\delta a^\dagger\delta b^\dagger\right). \end{aligned} \tag{3.21}$$

Here, $H_0 \equiv \hbar\Delta'\delta a^\dagger\delta a + \hbar\omega_m\delta b^\dagger\delta b$ is the free evolving part of the Hamiltonian and $H_1$ includes the rest of the terms in Eq. (3.20) which describe the interaction between the optical and mechanical modes. We are really interested in the dynamics due to interactions between these different modes and so, we transform into the interaction frame. The full derivation is included in Appendix D and we show the resulting interaction Hamiltonian below:

$$H_{int} = \hbar\left[e^{i(\Delta+\omega_m)t}g^*\delta a\delta b + e^{i(\Delta-\omega_m)t}g^*\delta a\delta b^\dagger + e^{-i(\Delta-\omega_m)t}g\delta a^\dagger\delta b + e^{-i(\Delta+\omega_m)t}g\delta a^\dagger\delta b^\dagger\right]. \tag{3.22}$$

For $\Delta = \omega_m$,

$$\begin{aligned} H_{int} &= \hbar\left(e^{2i\omega_m t}g^*\delta a\delta b + g^*\delta a\delta b^\dagger + g\delta a^\dagger\delta b + e^{-2i\omega_m t}g\delta a^\dagger\delta b^\dagger\right) \\ &\simeq \hbar\left(g^*\delta a\delta b^\dagger + g\delta a^\dagger\delta b\right). \end{aligned} \tag{3.23}$$

In Eq. (3.23), the rotating wave approximation is used where the fast oscillating terms are neglected. This is a valid approximation in this thesis as $\omega_m$ used in our numerical simulations are large. For instance, the electromechanical experiment of Palomaki et. al [59] is of the order of 10 MHz and the optomechanical experiment of Chan et. al [50] is of the order of 10 GHz. The interaction Hamiltonian in Eq. (3.23) resembles the beam splitter interaction in quantum optics where quantum state transfer can be achieved. Similarly, for $\Delta = -\omega_m$,

$$\begin{aligned} H_{int} &= \hbar\left(g^*\delta a\delta b + e^{-2i\omega_m t}g^*\delta a\delta b^\dagger + e^{2i\omega_m t}g\delta a^\dagger\delta b + g\delta a^\dagger\delta b^\dagger\right) \\ &\simeq \hbar\left(g^*\delta a\delta b + g\delta a^\dagger\delta b^\dagger\right). \end{aligned} \tag{3.24}$$

This interaction Hamiltonian (3.24), on the other hand, has the form of two mode squeezed state generation interaction in quantum optics [17, 81, 83, 85, 89, 131]. As discussed in Section 1.1, this form of interaction generates quantum entangled states.

We see that by choosing the detuning in the linearised, optomechanical interaction Hamiltonian

(3.22), we could carry out different quantum protocols. The analyses within the linearisation approximation show us that different dynamics and quantum protocols can be chosen by simply changing the detuning of the optomechanical system. From the interaction Hamiltonians in Eqs. (3.23) and (3.24), we also see that the linearisation scheme changes the nature of the nonlinear optomechanical interaction due to the radiation pressure. The corresponding time evolution equations of the optical and mechanical modes are linear, as discussed in Section 3.2.1.

## 3.3 Nonlinear quantum optomechanical Hamiltonian and phase space methods

In the previous section, the linearisation approximation was used to show that certain quantum protocols can be carried out in an optomechanical system. For most of the experiments carried out so far, the bare optomechanical coupling strength is weak, and the linearisation approximation does work well. However, as mentioned in Section 0.2, the full nonlinear quantum optomechanical Hamiltonian allows nonlinear quantum dynamics and effects to be observed. However, nonlinear quantum systems are hard to solve and analytical solutions are almost always impossible. This is where the phase space methods are useful. These methods work for both the linearised and nonlinear Hamiltonians. We discuss the phase space methods in the following.

Both the master equation and quantum Langevin equations described in Section 3.1 are nonlinear operator equations. Solutions can be obtained in the single mode optomechanical model with the linearization approximation [127]. However, analytical solutions without any approximations does not appear to exist. In addition to the nonlinear terms in the operator equations, the Hilbert space grows exponentially with the number of modes in the quantum system, making these equations intractable.

There are different methods in tackling these operator equations such as quantum trajectories and phase space methods. In this thesis, we use the phase space methods, which transform the master equation in Eq. (3.4) into a set of corresponding $c$-number stochastic differential equations. These stochastic differential equations can then be simulated numerically on a computer. The techniques and algorithms required to solve these stochastic differential equations numerically are well established [132–136]. In particular, we use the truncated Wigner and positive-P representations. These different representations are different ways of mapping operator equations into their corresponding c-number equations. Both the truncated Wigner [71, 72] and positive-P representations [73] have been employed in the previ-

ous work on the pulsed entanglement and Einstein-Podolsky-Rosen steering in optomechanics [137]. We devote this section to setting up stochastic differential equations based on phase space methods. It is intended as a quick guide to turn operator equations into c-number equations. For more details on phase space methods, we refer the readers to literature with extensive discussions on this method [71–73, 77, 78, 128].

### 3.3.1 Master equation to stochastic differential equations

The master equation dictates the time evolution of an optomechanical density operator, which characterise the probability amplitudes of the optical and mechanical modes in certain physical states. In phase space methods, operator identities map all operators in the master equation in Eq. (3.4) into complex numbers. The resulting equation is a time evolution equation of the probability distribution $P(\alpha,\alpha^+,\beta,\beta^+,t)$, where $\alpha$, $\alpha^+$, $\beta$ and $\beta^+$ are complex amplitudes of optical and mechanical modes. This is the Fokker-Planck equation. However, the Fokker-Planck equation cannot always be easily solved. Also, we are interested in the moments/statistics of certain observables. It is thus more useful to obtain time evolution equations of these complex optical and mechanical amplitudes. These time evolution equations constitute a set of stochastic differential equations and they can be obtained from the Fokker-Planck equation. Here, we just present the result without going through the derivations. Interested readers are referred to textbooks in Refs. [77, 78, 128]. A Fokker-Planck equation has the form

$$\frac{\partial}{\partial t}P(\vec{\alpha},t) = -\sum_i \frac{\partial}{\partial \alpha_i}A_i(\vec{\alpha},t)P(\vec{\alpha},t) + \frac{1}{2}\sum_{i,j}\frac{\partial^2}{\partial\alpha_i\partial\alpha_j}\left[\mathbf{D}(\vec{\alpha},t)\right]_{ij}P(\vec{\alpha},t)\,, \tag{3.25}$$

where $\vec{\alpha} = (\alpha_1,\alpha_2,...)$ is a vector containing all the complex amplitudes of the modes of a physical system, $\vec{A}(\vec{\alpha},t)$ is a vector called the drift and $\mathbf{D}(\vec{\alpha},t)$ is a positive matrix with real entries that is known as the diffusion matrix. The corresponding stochastic differential equations of the Fokker-Planck equation (3.25) is given by:

$$d\alpha_i = A_i(\vec{\alpha},t)\,dt + \sum_j B_{ij}dw_j\,. \tag{3.26}$$

Here $\mathbf{B}$ is a noise matrix, defined as $\mathbf{D} = \mathbf{B}\mathbf{B}^{\mathbf{T}}$ and $dw_j$ is a real, random number with Gaussian distribution such that $\langle dw_i dw_j \rangle = \delta_{ij}$.

The part that is less trivial in obtaining the corresponding stochastic differential equations from a Fokker-Planck equation is the decomposition of the diffusion matrix $\mathbf{D}$. In certain cases, the diffusion matrix can be easily diagonalised. If this is the case, the decomposition is just the square root of the diagonalised diffusion matrix. In general, there is a mathematical decomposition called the Takagi factorisation which always exists [138]. This factorisation is a special case of singular value decomposition. More often than not, one is fortunate enough to have a diffusion matrix that can be expressed as a set of diffusion matrices, each with known decomposition. When this is the case, there is an easy way to find the corresponding decomposition of the diffusion matrix. To be concrete, assume a diffusion matrix $\mathbf{D}$ that can be expressed as $\mathbf{D} = \mathbf{D_1} + \mathbf{D_2} + ...$, where the decomposition of each $\mathbf{D_i}$ is known, i.e. $\mathbf{D_i} = \mathbf{B_i}\mathbf{B_i^T}$. The decomposition of the diffusion matrix $\mathbf{D}$ then has the following form:

$$\mathbf{B} = \begin{pmatrix} \mathbf{B_1} & \mathbf{B_2} & ... \end{pmatrix}$$
$$\mathbf{B^T} = \begin{pmatrix} \mathbf{B_1^T} \\ \mathbf{B_2^T} \\ \vdots \end{pmatrix}. \tag{3.27}$$

It is straightforward to see that $\mathbf{D} = \mathbf{B}\mathbf{B}^{\mathbf{T}}$.

Given the expressions of the corresponding stochastic differential equations in Eq. (3.26) from a Fokker-Planck equation (3.25), we next present the stochastic differential equations satisfied by the master equation (3.4)

$$\frac{d}{dt}\rho = -\frac{i}{\hbar}[H,\rho] + \sum_j \gamma_j \bar{n}_j \left(2a_j^\dagger \rho a_j - a_j \rho a_j^\dagger - \rho a_j a_j^\dagger\right) + \sum_j \gamma_j (\bar{n}_j + 1)\left(2a_j \rho a_j^\dagger - a_j^\dagger a_j \rho - \rho a_j^\dagger a_j\right),$$

where $H$ is the optomechanical Hamiltonian given in Eq. (3.1):

$$H = \hbar\omega_c a^\dagger a + \hbar\omega_m b^\dagger b + \hbar g_0 a^\dagger a \left(b + b^\dagger\right) + i\hbar E(t)\left[-ae^{i\omega_d t} + a^\dagger e^{-i\omega_d t}\right].$$

In this thesis, we consider two possible phase space representations, namely the Wigner and positive-P representations to map the master equation (3.4) into the corresponding Fokker-Planck equation.

### 3.3.2 Truncated Wigner representation

The master equation (3.4) in the Wigner representation contains terms which have derivatives larger than the second order. The corresponding complex number equation is thus not a Fokker-Planck equation and the stochastic differential equations of the form (3.26) cannot be established. To circumvent this problem, we neglect terms with third order or higher derivatives. This is the truncation approximation.

There is a mathematically formal way to truncate higher order derivative terms. Roughly, one chooses a "system size" parameter, which in our case could be the cavity photon number $N$. Re-expressing cavity mode amplitude in terms of the scaled amplitude, the complex number equation is $1/\sqrt{N}$ expansion. Terms that are of the order $1/N^{3/2}$ are truncated. Obviously, this truncation is a good approximation for large cavity photon number. We note, however, that the argument provided is for the cavity mode amplitude. In principle, this expansion also has to be carried out for the mechanical mode amplitude. This can be done, but was not carried out. Instead, we run the truncated Wigner phase space simulation and compare the results with those using positive P representation, which has no truncation. All results agree within sampling errors justifying the validity of truncation approximation in the Wigner representation in our case. For a mathematically detailed treatment of the truncation, refer to Chapter in Carmichael's book [128]. A shorter explanation can be found in Chapter 5 of the thesis of Opanchuk [139].

The stochastic differential equations that dictate the time evolutions of the optical mode $\alpha$ and mechanical mode $\beta$ amplitudes are then given respectively by

$$\begin{aligned} d\alpha &= \left\{ -\left[ i\Delta + ig_0\left(\beta+\beta^*\right) + \frac{\gamma_o}{2}\right]\alpha \right\} d\tau + d\alpha_{in} \\ d\beta &= \left\{ -\left[ i\Delta + \frac{\gamma_m}{2}\right]\beta - ig_0|\alpha|^2 \right\} d\tau + d\beta_{in}\,, \end{aligned} \tag{3.28}$$

where $\Delta$ is the detuning between the external laser and cavity fields, $g_0$ is the optomechanical coupling strength, $\gamma_o$, $\gamma_m$ are the cavity and mechanical decay rates respectively and

$$\begin{aligned} d\alpha_{in} &= \sqrt{\gamma_{o,ext}}E\left(\tau\right) + \sqrt{\gamma_{o,ext}}d\alpha^{in}_{ext} + \sqrt{\gamma_{o,int}}d\alpha^{in}_{int} \\ &\equiv \sqrt{\gamma_{o,ext}}d\alpha^{in}_{ext,total} + \sqrt{\gamma_{o,int}}d\alpha^{in}_{int} \\ d\beta_{in} &= \sqrt{\gamma_m}d\beta^{in}\,. \end{aligned} \tag{3.29}$$

$d\alpha_{in}$ consists of the coherent input field, external and internal cavity losses. The thermal Gaussian noises satisfy

$$\langle d\alpha_i^{in} d\alpha_j^{in*} \rangle = \left( \bar{n}_{i,th} + \frac{1}{2} \right) \delta_{ij} d\tau \,. \tag{3.30}$$

The input mode into the cavity and the output mode from the cavity are related by the input-output relation [140–143]

$$\alpha_{out}(\tau) = \sqrt{\gamma_{o,ext}}\,\alpha(\tau) - \alpha_{ext,total}^{in}(\tau) \,. \tag{3.31}$$

Note that $\alpha_{ext,total}^{in}(\tau)$ in the input-output relation only includes the coherent input field $E(\tau)$ and noises entering the cavity $\alpha_{ext}^{in}$ but not noises due to internal cavity losses. The integrated input and output mode amplitudes are then obtained by integrating these modes with their corresponding temporal mode functions $u_{in}(\tau)$ and $u_{out}(\tau)$ as given below

$$\begin{aligned} A_{in} &= \int_{-\infty}^{0} u_{in}(\tau)\, \alpha_{ex,total}^{in}(\tau)\, d\tau \\ A_{out} &= \int_{0}^{\infty} u_{out}^{*}(\tau)\, \alpha_{out}(\tau)\, d\tau \,. \end{aligned} \tag{3.32}$$

These integrated input and output mode amplitudes will play important roles in the optomechanical quantum protocols in Chapters 4 and 5.

Next, we present the stochastic differential equations in the positive P representation. The process is identical to the one in the truncated Wigner representation and the only difference is the use of operator identities in the positive P representation.

### 3.3.3 Positive-P representation

The positive-P representation has no truncation approximation used in the truncated Wigner representation and hence it is exact in the absence of boundary terms [144, 145], apart from a controllable sampling error. The number of independent complex phase space variables are, however, doubled due to the dimension doubling approach for positive-P representation. The corresponding stochastic

differential equations are

$$\begin{aligned} d\alpha &= \left\{ -\left[ i\Delta + \frac{\gamma_o}{2} + ig_0\left(\beta+\beta^+\right)\right]\alpha \right\} dt + d\alpha_{in} \\ d\beta &= \left\{ -\left[ i\Delta + \frac{\gamma_m}{2}\right]\beta - ig_0\alpha^+\alpha \right\} dt + d\beta_{in} \\ d\alpha^+ &= \left\{ \left[ i\Delta - \frac{\gamma_o}{2} + ig_0\left(\beta+\beta^+\right)\right]\alpha^+ \right\} dt + d\alpha_{in}^+ \\ d\beta^+ &= \left\{ \left[ i\Delta - \frac{\gamma_m}{2}\right]\beta^+ + ig_0\alpha^+\alpha \right\} dt + d\beta_{in}^+ , \end{aligned} \tag{3.33}$$

where

$$\begin{aligned} d\alpha_{in} &= \sqrt{\gamma_{o,ext}}E\left(\tau\right) + \sqrt{\gamma_{o,ext}}d\alpha_{ext}^{in} + \sqrt{\gamma_{o,int}}d\alpha_{int}^{in} + d\alpha_{g_0}^{in} \\ d\beta_{in} &= \sqrt{\gamma_m}d\beta^{in} + d\beta_{g_0}^{in} \\ d\alpha_{in}^+ &= \sqrt{\gamma_{o,ext}}E^*\left(\tau\right) + \sqrt{\gamma_{o,ext}}d\left(\alpha_{ext}^{in}\right)^+ + \sqrt{\gamma_{o,int}}d\left(\alpha_{int}^{in}\right)^+ + d\left(\alpha_{g_0}^{in}\right)^+ \\ d\beta_{in}^+ &= \sqrt{\gamma_m}d\left(\beta^{in}\right)^+ + d\left(\beta_{g_0}^{in}\right)^+ . \end{aligned} \tag{3.34}$$

In the positive-P representation, there are noise terms due to the nonlinear interaction between the different modes. These are given by $d\alpha_{g_0}^{in}$, $d\left(\alpha_{g_0}^{in}\right)^+$, $d\beta_{g_0}^{in}$ and $d\left(\beta_{g_0}^{in}\right)^+$ and the only nonzero correlations between them are

$$\begin{aligned} \langle d\alpha_{g_0}^{in} d\beta_{g_0}^{in}\rangle &= -ig_0\alpha d\tau \\ \langle d\left(\alpha_{g_0}^{in}\right)^+ d\left(\beta_{g_0}^{in}\right)^+\rangle &= ig_0\alpha^+ d\tau . \end{aligned} \tag{3.35}$$

The thermal Gaussian noises are similar to those in the truncated Wigner representation.

$$\langle d\alpha_i^{in} d\left(\alpha_j^{in}\right)^+\rangle = \left(\bar{n}_{i,th}\right)\delta_{ij}d\tau . \tag{3.36}$$

The integrated input and output mode amplitudes are identical to those defined in Eq. (3.32).

## 3.4 Summary

We presented the Hamiltonian that describes an optomechanical system. As the system interacts with its environment and is hence an open quantum system, the master equation is used to formally describe the dynamics of the system. The Hamiltonian is linearised in this chapter to simplify the analysis of the

optomechanical system. The conclusion of the analyses is that the detuning of the system with respect to an external driving field allows demonstration of different physics. With a blue-detuned driving field, quantum entanglement between the optical and mechanical modes can be generated, while a red-detuned driving field allows quantum state transfer between optical and mechanical modes.

We then return to the problem of solving the master equation. Since it is an operator equation with nonlinearity and hence cannot be solved in general, the strategy is to convert it into a complex-number equation known as the Fokker-Planck equation. We presented two ways that this transformation can be carried out, using what is known as the truncated Wigner and positive P representations. From the Fokker-Planck equation, it turns out that a set of stochastic differential equations dictating the time evolution of amplitudes of the optical and mechanical modes can be obtained. Explicit stochastic differential equations for the full, nonlinear optomechanical system, in both the truncated Wigner and positive P representations, are presented.

# Chapter 4

# Optomechanical quantum memory and coherent state transfer

We have seen how quantum states can be transferred between the optical and mechanical modes in an optomechanical system in Chapter 3. This is the basis of an optomechanical quantum memory, which is the topic of this chapter. A quantum memory is a device that stores quantum states. Optomechanics is a good candidate for a quantum memory: there are standard quantum optical techniques for the generation of quantum states of light that can be shaped temporally and spatially. These quantum states can be stored in long lived mechanical modes via a radiation pressure interaction. A quantum memory has important applications in proposed quantum internet systems [146–148], where a network of nodes are connected by optical fibers. There are many other proposed applications as well. Generally, optomechanical nodes can transmit and receive optical quantum states, which can be stored in mechanical oscillators at each node with low dissipation. Advances in mechanical quantum ground state cooling techniques [50, 53, 125, 126] further reduce the spurious effects of thermal noise entering the optomechanical system.

In Section 4.1, we describe a specific optomechanical quantum memory protocol involving two pulses, one for generating the quantum state and the other for transferring the quantum state between the optical cavity and mechanical modes. In particular, we study this protocol for coherent states. In Section 4.2, we look at a linearised quantum memory model. Finally, we present the phase space simulation results for the full, nonlinear optomechanical quantum memory protocol in Section 4.3. This chapter is based on the published work by Teh et al. [149].

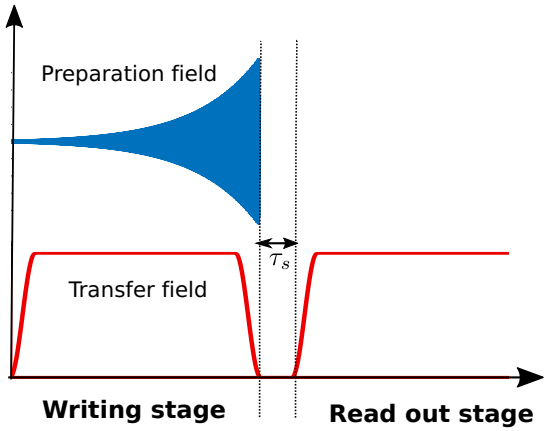


Figure 4.1: The two-pulse optomechanical state transfer protocol, where $\tau_s$ is the storage time of the quantum state in the mechanical mode. In this chapter, we also consider the effect of finite transfer field turning on/off (also known as the transfer field switching) time. This is the time taken for a transfer field to be fully turned on/off, and these are represented in the diagram where the transfer field has finite gradients.

## 4.1 Optomechanical quantum state transfer and quantum memory

Based on the fact that a red-detuned external field transfers quantum states between the cavity and mechanical oscillator, we consider a particular state transfer protocol as shown in Fig. 4.1, that involves two external field pulses, which we named the preparation and transfer fields. The preparation/signal field generates the cavity quantum state that is to be stored in the quantum memory and the transfer/control field facilitates the quantum state transfer between the cavity and mechanical modes. The preparation field has the same frequency as the resonance frequency of the resonator $\omega_c$ while the transfer field has frequency $\omega_d$ such that the detuning $\Delta$ between the resonator and the transfer field frequency is the frequency of the mechanical oscillator, i.e. $\Delta = \omega_c - \omega_d = \omega_m$.

The optomechanical state transfer protocol consists of three stages. The writing stage involves sending the quantum state into the cavity and transferring it to the mechanical system. During this stage, both the preparation and transfer fields are applied. This simultaneously generates the cavity quantum state and transfers it to the mechanical mode. After the quantum state is completely transferred to the mechanical mode, both fields are turned off in the storing stage. Due to the low mechanical decay rate $\gamma_m$, the mechanical oscillator serves as a good quantum memory. The stored quantum state will retain its coherence on a timescale of $1/\gamma_m$. Finally, a second transfer field is applied in the readout stage.

This transfers the quantum state from the mechanical mode back into the cavity, which will then leak out of the cavity and subsequently be detected.

Based on the Hamiltonian in Eq. (3.3), the optomechanical quantum memory Hamiltonian is expressed as

$$\tilde{H} = \hbar\omega_m a^\dagger a + \hbar\omega_m b^\dagger b + \hbar g_0 a^\dagger a\left(b + b^\dagger\right) - i\hbar\sqrt{2\gamma_{ext}}\left[\varepsilon(t)\, a - \varepsilon^*(t)\, a^\dagger\right], \tag{4.1}$$

where $\varepsilon(t) = \varepsilon_{trans}(t) + \varepsilon_{prep}(t)\, e^{-i\omega_m t}$. Here, $\varepsilon_{trans}(t)$ and $\varepsilon_{prep}(t)$ correspond to the transfer field and preparation field amplitudes, respectively. We choose to transform into the rotating frame of the transfer field, leaving the preparation field oscillating at the resonance frequency of the mechanical oscillator $\omega_m$. Note that both the transfer and preparation fields are time dependent. This is essential for an optimal optomechanical state transfer. We discuss this by considering a linearised quantum memory model in the next section and give more details of the precise time-dependence of preparation and transfer fields in later sections.

## 4.2 Linearised quantum memory model

In this section, we use the linearisation approximation so that analytical solutions for both the optical and mechanical modes time evolution equations can be found. As we will see shortly, these solutions make clear the choice of optimal temporal mode function of the preparation field. The temporal mode function determines the time scale of the optomechanical state transfer protocol. Similarly, the output field from the cavity that will be detected has a time dependence in its mode function and has to be mode matched too for efficient detection.

### 4.2.1 Input fields

The cavity mode is a function of space and time. In this chapter, we assume single (longitudinal) mode with the cavity resonance frequency $\omega_c$ which is fixed by the size of the cavity and express the cavity mode in terms of a set of orthogonal temporal transverse modes. For simplicity, we only consider the storage of a coherent cavity amplitude in one of these temporal modes. In order to optimise the coupling between the preparation field and the cavity, the preparation field containing the coherent state to be stored in the optomechanical system has to temporally mode match to one of these orthogonal cavity

temporal modes. Perfect mode matching ensures that only the intended cavity mode will remain in the cavity and other modes will either be reflected or leak out of the cavity.

The optimal mode function for the preparation field is obtained by solving the time evolution equations and since these equations are nonlinear and intractable in general, we invoke the linearisation approximation. Within this approximation, analytical expressions for both optical and mechanical modes will be obtained, which determine the optimal temporal mode function. The optimal mode function for the preparation field within the linearisation approximation was first obtained by He et al. [150, 151]. These linearised calculations are instructive as they provide a simple theoretical description of the subsequent experimental demonstrations of coherent state transfer [59]. In this section, we include linearised calculations similar to those of He et al. [150], but taking into account internal cavity losses. These calculations serve the purpose of checking the validity of the linearisation approximation in optomechanical quantum memory experiments. In their work, He and co-workers solved the stochastic differential equations describing the time evolution of both the cavity $a(t)$ and mechanical modes $b(t)$. Those equations are derived from the effective interaction Hamiltonian

$$H_{int} = \hbar g \left( a b^{\dagger} + a^{\dagger} b \right) , \tag{4.2}$$

where $g = g_0 \sqrt{N}$ is the effective coupling strength and $N$ is the intracavity photon number of the transfer field. The interaction Hamiltonian (4.2) contains the linearisation and rotating wave approximations.

The corresponding linearised Heisenberg time evolution equations

$$\begin{aligned} \frac{d}{dt} a(t) &= -\gamma_o a - igb + \sqrt{2\gamma_{ext}} a_{ext}^{in} + \sqrt{2\gamma_{int}} a_{int}^{in} \\ \frac{d}{dt} b(t) &= -\gamma_m b - iga + \sqrt{2\gamma_m} b^{in} \end{aligned} \tag{4.3}$$

can be solved analytically. Here, $a_{ext}^{in}$ contains the preparation field and other noises from outside of the cavity, while $a_{int}^{in}$ includes all other noises in the cavity. The general solution $\vec{a}(t) = \begin{pmatrix} a(t) \\ b(t) \end{pmatrix}$ for the writing stage is

$$\vec{a}(t) = \int_{-\infty}^{t} e^{\kappa_+ \tau} cosh(m\tau) I \vec{a}_{in}(\tau)\, d\tau + \int_{-\infty}^{t} e^{\kappa_+ \tau} \frac{sinh(m\tau)}{m} \begin{pmatrix} \kappa_- & ig \\ ig & -\kappa_- \end{pmatrix} \vec{a}_{in}(\tau)\, d\tau , \tag{4.4}$$

where $\vec{a}_{in}(t) = \begin{pmatrix} \sqrt{2\gamma_{ext}}a_{ext}^{in} + \sqrt{2\gamma_{int}}a_{int}^{in} \\ \sqrt{2\gamma_m}b^{in} \end{pmatrix}$, $\kappa_+ = (\gamma_o + \gamma_m)/2$, $\kappa_- = (\gamma_o - \gamma_m)/2$ and $m = \sqrt{\kappa_-^2 - g^2}$. The preparation field in the optomechanical state transfer protocol is $a_{ext}^{in} = a_0 u_{in}$, where $a_0$ is the initial mode-matched external field operator whose coherent amplitude we want to store, and $u_{in}$ is the temporal external mode function yet to be determined. The task is to find out what should the time dependence of the preparation field be for optimal state transfer.

To this end, we consider the stored mode in the mechanical system which is given by

$$b(0) = \sqrt{2\gamma_{ext}} \int_{-\infty}^{0} \frac{ig}{m} a_0 u_{in}(\tau) e^{\kappa_+ \tau} \sinh(m\tau)\, d\tau + \text{noise}. \tag{4.5}$$

From the mechanical mode amplitude solution above, we choose the mode function of the form

$$u_{in}(t) = -2i \frac{\sqrt{(\kappa_+ + m)(\kappa_+ - m)\kappa_+}}{m} \exp(\kappa_+ t) \sinh(mt), \tag{4.6}$$

which is normalised, i.e. $\int_{-\infty}^{0} |u_{in}(t)|^2 dt = 1$. To verify that this choice is an optimal one, solve Eq. (4.5) using the temporal input mode function $u_{in}(t)$ given in Eq. (4.6). The stored mode operator is then

$$b(0) = \frac{\sqrt{2\gamma_{ext}}ga_0}{2\sqrt{(\kappa_+ + m)(\kappa_+ - m)\kappa_+}} + \text{noise}. \tag{4.7}$$

For the case where there are no internal cavity losses and in the limit where the cavity decay rate is much larger than the mechanical dissipation rate $\gamma_o \gg \gamma_m$, it is straightforward to show that the stored mode operator (4.7) will always be the external operator $a_0$, in addition to a noise term that includes all possible noises:

$$b(0) = a_0 + \text{noise}. \tag{4.8}$$

Note that the optimal mode function is obtained from the solutions of Eq. (4.3) and the mode function is optimal for any arbitrary coupling strength $g$. In reality, the validity of the linearised interaction Hamiltonian in Eq. (4.2) might not hold in certain regimes where nonlinear effects cannot be neglected. For those cases, the mode function in Eq. (4.6) will not be the optimal one. Depending on the observ-

ables one wishes to compute, other methods, such as functional optimisation, can be used to obtain the optimal mode function.

**Remark**: The transfer field only affects the steady state of the cavity mode in the linearisation analyses. In nonlinear simulations, these intense transfer fields give rise to transient behavior in the cavity mode amplitude when transfer fields are switched on or off. They appear as huge spikes in the cavity mode amplitude. Power spectral densities reveal that the frequency content of the transfer and preparation fields overlap. Moreover, the finite transfer field switching time has significant effects on the efficiency of the optomechanical state transfer. This phenomenon cannot be easily studied in the linearisation scheme. In other words, the linearisation approximation can be problematic.

Next, we discuss the issue of the optomechanical state transfer protocol duration. The duration of the writing stage is determined by the temporal input mode function, which we analyse in the following. The input mode function has the form $\left[e^{(\kappa_+ + m)t} - e^{(\kappa_+ - m)t}\right]\Theta(-t)$ as in Eq. (4.6). In the limit where $\gamma_m \ll g \ll \gamma_o$, it can be shown that $\kappa_+ + m \approx \gamma_o$, $\kappa_+ - m \approx g^2/\gamma_o$ and hence $e^{(\kappa_+ - m)t}\Theta(-t)$ is the dominating term in the temporal input mode function during the writing stage. The duration of the writing stage has to be longer than $1/(\kappa_+ - m)$. Simply put, the duration has to be long enough to include the whole pulse. In the weak coupling limit ($g < \gamma_o$), the pulse duration depends on the ratio between $g$ and $\gamma_o$ and weaker coupling strength $g$ requires a longer writing stage.

In the strong coupling limit ($g > \gamma_o$), $m$ is a complex number and the duration of the writing stage has to be longer than $1/\kappa_+$. The storage time in the mechanical mode is determined by the mechanical dissipation rate and it has to be shorter than $1/\gamma_m$. In this chapter, the storage time is restricted to be much smaller than the mechanical lifetime in order to reduce the number of time steps in our simulations. In the state transfer protocol treated here, the output mode is a time-reversed version (around $t = t_s/2$) of the input field, where $t_s$ is storage time of the quantum state in the mechanical mode. Hence, the read-out stage duration is chosen to be the same as the writing stage. Other protocols are available where the input and output modes are symmetric functions [151], and in such cases the input and output modes are identical, which is more useful for cascaded quantum logic operations. The use of symmetric function in the input and output modes in a quantum protocol is discussed in Chapter 5.

### 4.2.2 Output fields

The output field from the cavity $a_{out}$ contains the signal stored in a single mode, as well as other

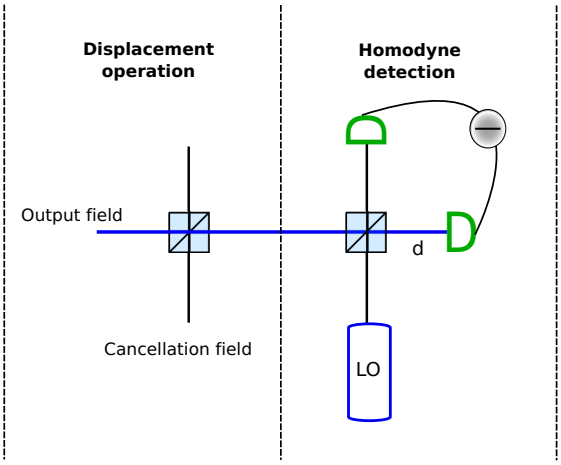


Figure 4.2: The transfer field contribution to the output field is subtracted using the cancellation field. The resulting field is then detected with a homodyne detection scheme.

noises, in all other independent, orthogonal modes. The output field obeys the standard input-output theory [140–143], which relates the output field to the input and cavity fields. Typically, the output fields are measured using a homodyne detection scheme. In order to detect and extract the signal, the local oscillator mode in the homodyne detection scheme has to be temporally mode matched to the mode function of the signal. The schematic of the above mentioned approach is shown in Fig. 4.2. This extraction is possible due to the orthogonality of these mode functions. Also, due to the time-reversal symmetry of the state transfer protocol around $t = t_s/2$, the output temporal mode function $u_{out}(t)$ is related to the input temporal mode function $u_{in}(t)$ by $u_{out}(t) = u_{in}^{*}(t_s - t)$, so that:

$$u_{out}(t) = 2\frac{\sqrt{(\kappa_+ + m)(\kappa_+ - m)\kappa_+}}{m}\exp\left[-\kappa_+(t - t_s)\right]\sinh\left[m(T - t)\right]. \tag{4.9}$$

We note that the output field is a product of the mode amplitude and the corresponding mode function. To extract the mode amplitude of the corresponding temporal mode, the integrated output is computed using

$$A_{out} = \int_{t_s}^{\infty} u_{out}^{*}(t)\, a_{out}(t)\, dt. \tag{4.10}$$

The integrated output in the linearised approximation is calculated to be

$$A_{out} = \frac{\gamma_{ext}}{2\left(\kappa_+ + m\right)\left(\kappa_+ - m\right)\kappa_+}\left(g^2 \mathrm{e}^{-\gamma_m t_s} - \gamma_m^2 e^{-\gamma_o t_s}\right) A_{in} + \text{noise}\,, \tag{4.11}$$

where $A_{in} = \int_{-\infty}^{0} u_{in}^{*}(t)\, a_{in}(t)\, dt$ is the integrated input.

The advantage of the output mode matching approach for quantum state retrieval is that both the amplitude and phase information of the quantum state are retained. This is crucial for any claim of a working quantum memory.

It is more common, however, to record the output power spectrum in experiments. This is mainly because output power spectra allow the characterisation of optomechanical parameters. In the case of optomechanical state transfer, integrating the power spectrum around the signal frequency gives the intensity or energy of the state stored. This can then be compared with the intensity or energy of the input state. The state transfer efficiency is subsequently deduced from the ratio of these two quantities. This method has the drawback of lost information on the phase of the state stored. The quantum nature of the stored state cannot be verified and the claim of a memory device is at best a classical one.

In this section, we solved linearised Heisenberg time evolution equations to demonstrate the need for time dependence in the preparation field for optimal coupling into the cavity. From the temporal mode function, the time scale of the optomechanical state transfer protocol is determined. In the next section, we present the numerical phase space simulation results of the optomechanical quantum memory protocol.

## 4.3 Numerical simulations and results

Using the phase space methods described in Section 3.3, it is possible to carry out the corresponding phase-space simulations using either normally ordered positive P methods, or symmetrically ordered truncated Wigner methods that include a truncation approximation. While the first are more precise, the second can be faster, depending on the random sampling error that is required. We carry out both types of calculation, and find that they give results that are the same within sampling error, for these parameter values. We present and discuss the results of our nonlinear phase space simulations.

We first briefly describe the experiment and its parameter that are used in the numerical simulations. An aspect which is not often discussed in the literature is the finite time needed to turn the transfer field

on or off. This finite switching time of the transfer field affects the efficiency of the protocol and this will be presented. Also in this section, we discuss how power spectral densities and quantum fidelity can be computed using phase space methods.

### 4.3.1 Electromechanical experiment and parameters

We simulated the quantum memory protocol using electromechanical experiment parameters of Palomaki et al. [59]. The experiment demonstrated coherent state transfer using an electromechanical system, consisting of an LC resonator where one of the plates of the capacitor is movable, behaving like a mechanical oscillator. The resonance frequency of the resonator is $\omega_c/2\pi \approx 7.5$GHz and the resonance frequency of the mechanical oscillator is $\omega_m/2\pi = 10.5$MHz. The decay and dissipation rates for the resonator and mechanical oscillator are characterized by $\gamma_o = \gamma_{int} + \gamma_{ext}$ and $\gamma_m$ respectively. The total decay rate of the resonator, $\gamma_o/2\pi$ is 170kHz with $\gamma_{ext}/2\pi = 137.5$kHz.

The mechanical dissipation rate $\gamma_m$ is $2\pi \times 17.5$Hz. The interaction between the resonator and mechanical modes is analogous to the interaction in cavity optomechanics due to the radiation pressure. The coupling between the resonator and mechanical mode is $g_0$, which is $2\pi \times 200$Hz in the experiment. The enhanced coupling strength $g$ is defined to be $g_0\sqrt{N}$, where $N$ is the average number of photons in the cavity. The electromechanical system is maintained at $25\mu$K, which corresponds to an average thermal phonon number of 50. The constant transfer field amplitude $\varepsilon_{trans}$ is determined from the steady state solutions of the corresponding stochastic differential equations. It is given by

$$\varepsilon_{trans} = \sqrt{\frac{(\omega_m^2 + \gamma_o^2)N}{2\gamma_{ext}}}, \tag{4.12}$$

where $N$ is the average number of photons in the cavity. The coherent state sent into the electromechanical system has a photon number expectation value of 35 and the storage time in mechanical oscillator is $t_s = 25\mu$s.

We assume both the resonator and mechanical oscillator to be in their ground states initially. This is a good approximation for the resonator in the gigahertz range as the average thermal occupation number is essentially zero at the temperature of order $\mu$K, as in their experiment. The mechanical ground state is harder to achieve as it is more susceptible to thermal noise. Besides, theoretical analyses [152, 153] showed that, even in the resolved sideband limit ($\omega_m \gg \gamma_o$), there is a nonzero lower bound

to the mean mechanical phonon number. However, mechanical ground state has been achieved in many different experimental implementations of optomechanics. In particular, recent experimental work demonstrated sideband cooling beyond the quantum back-action limit using squeezed light [126]. This allows mechanical quantum ground states to be reached.

### 4.3.2 Numerical methods

All numerical simulations are carried out using xSPDE, which is an open source software package written in Matlab to solve stochastic differential equations [154]. The numerical results were obtained using a fourth order Runge-Kutta method in the interaction picture [132, 154], with $10^5$ parallel trajectories for both the truncated Wigner and positive P simulations.

We express all stochastic differential equations in dimensionless form, by introducing dimensionless time variable $\tau = \gamma_o t$, where all parameters are relative to the cavity amplitude decay rate, $\gamma_o$. This makes clear the regimes of interest. For instance, $\Omega_m = \omega_m/\gamma_o$ determines whether the system is in the resolved sideband regime, which is important for mechanical ground state cooling [50, 53, 125]. The ratio $G = g/\gamma_o$, on the other hand, determines whether the system is in the strong coupling regime [59, 155]. All dimensionless parameters are denoted by capital Greek letters of their corresponding parameters given in Section 4.3.1, unless stated otherwise.

For instantaneous switching, as used in all the subsections below except subsections (4.3.5), and (4.3.6), the plots are obtained by first solving the dimensionless stochastic differential equations given in Eq. (4.3) with a time dependent input field $E(\tau)$ as follows:

$$E(\tau) = \begin{cases} E_{trans} + E_{prep}(\tau) & , -\tau_w \leq \tau \leq 0 \\ 0 & , \quad 0 \leq \tau \leq \tau_s \\ E_{trans} & , \quad \tau_s \leq \tau \leq \tau_r \,, \end{cases} \tag{4.13}$$

where $\tau_w$, $\tau_s$ and $\tau_r = \tau_w$ are the duration of the writing, storing and read-out stages, respectively.

The transfer field amplitude $E_{trans} = \sqrt{(\Omega_m^2 + \Gamma_o^2) N/(2\Gamma_{ext})}$, the preparation field amplitude $E_{prep}(\tau) = \alpha_0 u_{in}(\tau)$, with coherent state amplitude $\alpha_0 = \sqrt{N_c}$, where $N_c$ is the coherent photon number that is input for storage. The temporal input mode function is calculated as the optimal one, namely:

$$u_{in}(\tau) = -2i \frac{\sqrt{(K_+ + M)(K_+ - M)\kappa_+}}{M} e^{(K_+\tau)} \sinh(M\tau) e^{-i\Omega_m \tau} \,. \tag{4.14}$$

Here, $K_+ = (\Gamma_o + \Gamma_m)/2$, $\kappa_- = (\Gamma_o - \Gamma_m)/2$ and $M = \sqrt{K_-^2 - G^2}$. In most of the simulations, $N_c = 35$, as in recent coherent state transfer experiments, however, the effect of storing different input photon numbers on the measurable fidelity is explored in subsection (4.3.6). It should be noted that recent experiments did not use this optimal pulse shape.

In subsection (4.3.5), dealing with finite switching time, a different state transfer protocol is explored in which the transfer fields are turned on and off continuously over a finite time duration. This reduces the spectral width of the transfer field. It is closer to what is actually used in an experiment, although experimental transfer fields may have spectra that differ in detail from the relatively simple models used here. Details of this are given later.

The number of time steps differ for different coupling strengths $G$, since the optomechanical state transfer protocol duration varies with $G$. The step in dimensionless time $d\tau$ was chosen to be $1/[10(\Omega_m + \mathrm{Im}(M))]$, where $M = \sqrt{K_-^2 - G^2}$ is defined in the previous section. This choice of step in dimensionless time $d\tau$ is much smaller than that stated in the sufficient sampling rate criterion in the Shannon sampling theorem [156]. Consequently, the finite time step error, which was calculated by repeating calculations with a step-size reduced by 50%, was much less than the sampling error.

### 4.3.3 Power spectral densities

As mentioned previously, the spectral content of the output field reveals overlap between the control and signal fields. The spectral content of a field is obtained by computing the power spectral density. Here, we define the output power spectral density and its computation in the truncated Wigner representation. The output power spectral density is given by the expectation value:

$$S(\Omega) = \frac{2\pi}{T}\langle \hat{a}_{out}^{\dagger}(\Omega)\,\hat{a}_{out}(\Omega)\rangle \tag{4.15}$$

which gives the average dimensionless intensity of the output signal at the dimensionless frequency $\Omega$, over a dimensionless observation time $T = \tau_r - \tau_s$. The frequency domain mode operator $\hat{a}_{out}(\Omega)$ is defined as the windowed Fourier transform of the time domain mode operator $\hat{a}_{out}(\tau)$, i.e,

$$\hat{a}_{out}(\Omega) = \frac{1}{\sqrt{2\pi}}\int_{\tau_S}^{\tau_r} e^{i\Omega\tau}\hat{a}_{out}(\tau)\,d\tau \tag{4.16}$$

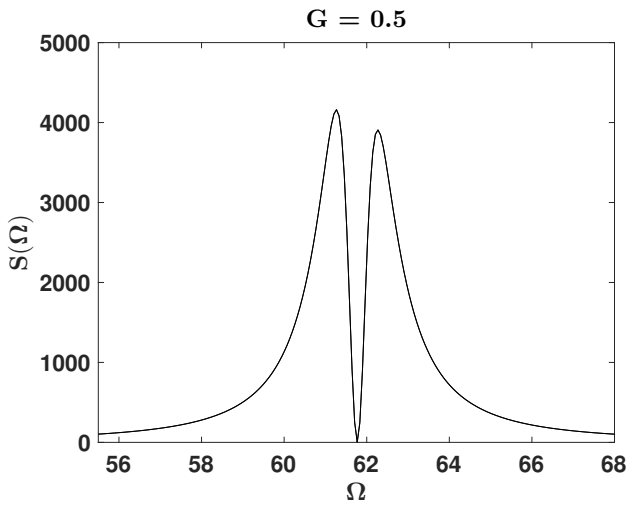


Figure 4.3: The output field power spectral density $S(\Omega)$ given in Eq. (4.18) for $G = 0.5$ from the nonlinear truncated Wigner simulations. The signal is on top of the transfer field frequency content.

and the operator $\hat{a}^{\dagger}(\Omega)$ is the Hermitian conjugate of the operator $\hat{a}(\Omega)$:

$$\hat{a}^{\dagger}_{out}(\Omega) = \frac{1}{\sqrt{2\pi}} \int_0^T \mathrm{e}^{-i\Omega\tau} \hat{a}^{\dagger}_{out}(\tau)\, d\tau\,. \tag{4.17}$$

The dimensionless output power spectral density is obtained in the truncated Wigner representation using the relation

$$S(\Omega) = \langle |\alpha_{out}(\Omega)|^2 \rangle_{Wigner} - \frac{1}{2}\,, \tag{4.18}$$

where $\alpha_{out}(\Omega)$ is the Fourier transform of the output field amplitude in the truncated Wigner representation $\alpha_{out}(\tau)$. The $\frac{1}{2}$ in Eq. (4.18) comes from the fact that Wigner representation is used to evaluate symmetrically ordered observables.

From nonlinear numerical simulations, without displacement operations as described in Section 4.2.2, we compute the output field power spectral densities expressed in Eq. (4.18). Fig. 4.3 and Fig. 4.4 show the full, nonlinear output field spectra for $G = 0.5$ and $G = 2.0$, respectively, in the truncated Wigner representation.

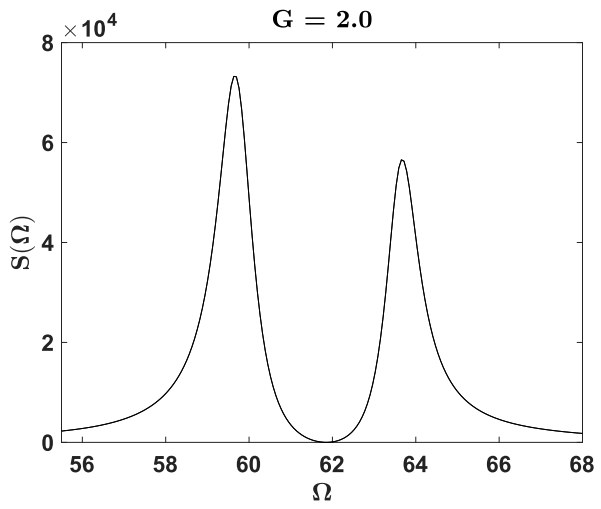


Figure 4.4: The output field power spectral density $S(\Omega)$ given in Eq. (4.18) for $G = 2.0$ from the nonlinear truncated Wigner simulations. The signal is on top of the transfer field frequency content.

We see in Fig. 4.3 and Fig. 4.4 that the signal content is situated on top of a large amplitude due to the intense transfer field. This overlap of signal and carrier in output spectra means that filtering is required for signal extraction. We note that this overlap occurs even when the transfer field and preparation field frequencies are about $2\pi \times 10^7$Hz apart. This overlap is due to the intense transfer field that drives the electromechanical system. Even for $G < 1$, the output spectrum is radically different to what is expected for a Lorentzian signal, owing to strong interference between the spectral tails of the transfer field and the signal itself, which has a very low amplitude by comparison. For $G > 1$, the output field spectra exhibit double-peak feature known as the optomechanical normal mode splitting. First observed experimentally by Gröblacher et al. [157] and subsequently with larger $G$ by Teufel et al. [52], the optomechanical normal mode splitting with the splitting set by $2G$ is a signature of the strong coupling regime. Note that the two peaks observed in the output field spectrum is distinctively different from the input spectrum expected for a coherent light, which has a Lorentzian signal. Hence, we expect the fidelity of the output field with respect to the input field to be lower in the strong coupling regime than in the weak coupling regime.

There are a number of ways one can attempt to remove the transfer field contribution in the output field that one detects. In the experimental work by Andrews et al. [158], the frequency content of the transfer field around the signal frequency is notch filtered before sending it into the electromechanical

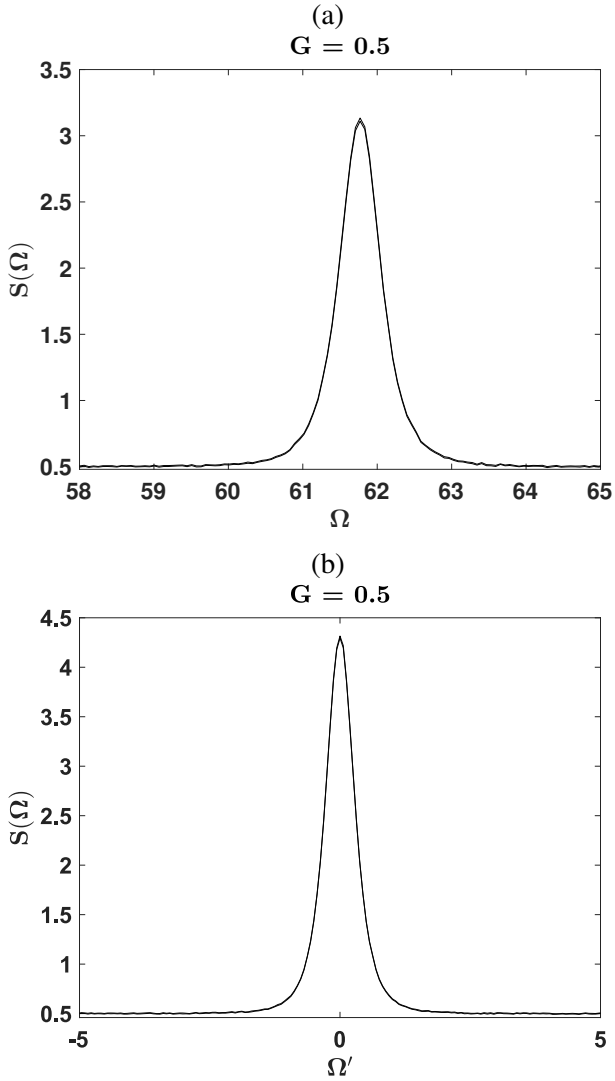


Figure 4.5: The top figure corresponds to the displaced, output field spectrum in a full, nonlinear truncated Wigner simulation while the bottom figure shows the output field spectrum of a linearised truncated Wigner simulation. The dimensionless signal frequency in the nonlinear simulation is at $\Omega = \Omega_m$ as the system is in the rotating frame of the transfer field, while the dimensionless signal frequency in the linearized simulation is at $\Omega' = 0$. The number of samples taken is $10^5$.

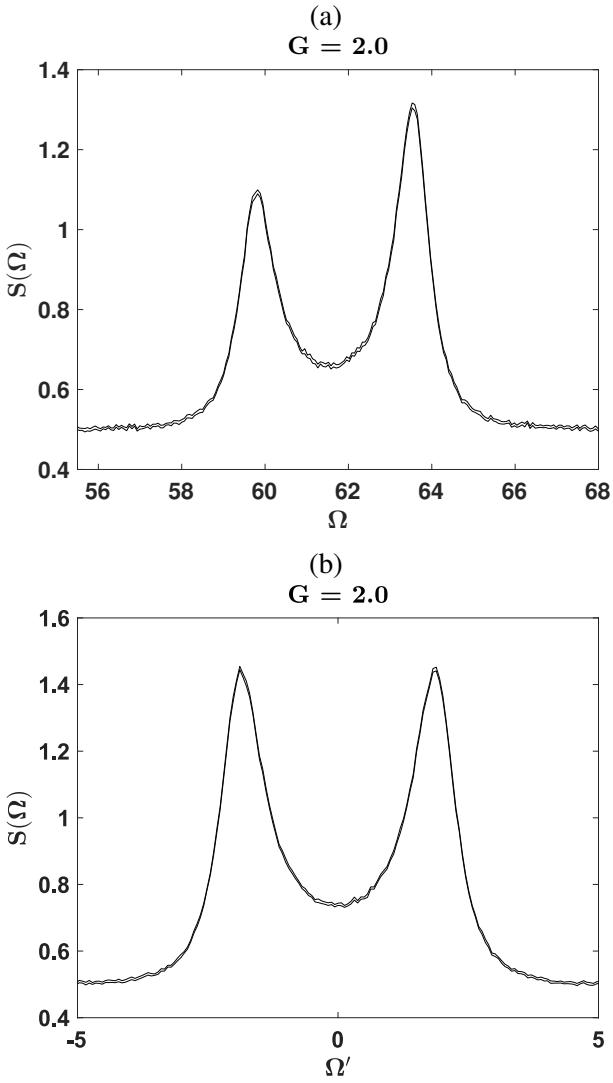


Figure 4.6: The top figure corresponds to the displaced output field spectrum in a full, nonlinear truncated Wigner simulation while the bottom figure shows the output field spectrum of a linearised truncated Wigner simulation. Axes labels as for Figure 4.5. The number of samples taken is $10^5$.

system. Another method removes the amplitude due to the transfer field in the time domain, using a beam splitter in what is essentially a type of Mach-Zehnder interferometer. Here we adopt the second approach in our nonlinear simulations.

This second approach of removing the transfer field amplitude in the output field involves a cancellation field. This has also been suggested by Akram et al. [159] by mixing the output field with a local oscillator field using a beam splitter. This procedure, achieved in quantum optics experiments [160–162], is nothing but a displacement of the phase space cavity amplitude by the amplitude due to the transfer field. The gedanken experiment that corresponds to this method is shown in Fig. 4.2. An output field containing amplitudes from both the signal $\alpha$ and transfer field $\beta$ is mixed with a cancellation field $A_{cancel}$ in a beam splitter with transmissivity $\eta$. The output port $d$ in the Fig. 4.2, obtained using the standard beam splitter operation, is given by

$$\begin{aligned} d &= \sqrt{\eta}\,(\alpha+\beta) - \sqrt{1-\eta}A_{cancel} \\ &= \sqrt{\eta}\alpha + \left(\sqrt{\eta}\beta - \sqrt{1-\eta}A_{cancel}\right). \end{aligned} \tag{4.19}$$

By setting the transmissivity $\eta$ close to 1, the amplitude of the cancellation field $A_{cancel}$ is adjusted accordingly to cancel out the second term. It is straightforward to see that a cancellation field $A_{cancel}$ that is much more intense than the transfer field is necessary. Ideally, the cancellation field is split off from the transfer field. This implies that the initial transfer field has to be greatly amplified, which is not always possible. For instance, in order to place the optomechanical system in the strong coupling regime, a very intense transfer field is needed to enhance the optomechanical coupling. This renders an even more intense cancellation field impractical. This scheme also leads to losses in the signal $\alpha$, but we treat this rather simple protocol to allow a clear explanation of the issues involved. Other schemes, like a balanced cancellation where the transfer fields are subtracted while the signals are added, may be feasible also.

The phase space amplitude displacement described above is implemented numerically by simulating the whole state transfer protocol without the preparation field. The mean output field from this simulation is then subtracted from the output field of a full, nonlinear optomechanical state transfer simulation.

Fig. 4.5(a) and Fig. 4.6(a) show the numerical results for the output field spectra after the displacement operation in the nonlinear truncated Wigner simulations. Also plotted are the output field

spectra obtained from the linearised truncated Wigner simulations as shown in Fig. 4.5(b) and Fig. 4.6(b). These plots are obtained by solving stochastic differential equations as given in Eq. (4.3), in the dimensionless form with the effective coupling strength

$$G(\tau) = \begin{cases} G & , -\tau_w \leq \tau \leq 0 \\ 0 & , \quad 0 \leq \tau \leq \tau_s \\ G & , \quad \tau_s \leq \tau \leq \tau_r \end{cases} \tag{4.20}$$

and the input field

$$E(\tau) = \begin{cases} E_{prep}(\tau) & , -\tau_w \leq \tau \leq 0 \\ 0 & , \text{otherwise} \ , \end{cases} \tag{4.21}$$

where $E_{prep}(\tau) = \alpha_0 u_{in}(\tau)$, with the coherent state amplitude $\alpha_0 = \sqrt{35}$ and the temporal input mode function

$$u_{in}(\tau) = -2i\frac{\sqrt{(K_+ + M)(K_+ - M)\kappa_+}}{M} e^{(K_+\tau)} \sinh(M\tau) \ . \tag{4.22}$$

The signal frequency in the linearised simulations is at $\Omega' = 0$ while the signal frequency in the nonlinear simulations is at $\Omega = \Omega_m$ since we transformed into the rotating frame of the transfer field.

### 4.3.4 Integrated input and output modes using temporal mode functions

Using the temporal mode functions introduced in Section 4.2.2, the energy retrieved with respect to the energy stored can be computed straightforwardly. However, due to the fact that the stored cavity amplitude in a particular mode contains a contribution from the transfer field, we remove this amplitude via a displacement operation in the phase space as described in Section 4.3.3. We integrate the input and output modes with their corresponding temporal mode functions to pick out the desired input and output signals. The efficiency of the protocol is defined to be

$$\zeta_{instant} \equiv \frac{|A_{out}|}{|A_{in}|} \ . \tag{4.23}$$

| G | Integrated input, $A_{in}$ | Integrated output, $A_{out}$ | $\zeta_{instant} = \frac{\lvert A_{out}\rvert}{\lvert A_{in}\rvert}$ |
|---|---|---|---|
| 0.50 | 5.9161 | $(4.7716+0.0971i)\pm(0.0056+0.0063\text{i})$ | $0.8067\pm0.0010$ |
| 0.75 | 5.9161 | $(4.7697+0.1869i)\pm(0.0052+0.0056\text{i})$ | $0.8068\pm0.0009$ |
| 1.00 | 5.9161 | $(4.7604+0.2890i)\pm(0.0062+0.0071\text{i})$ | $0.8061\pm0.0012$ |
| 1.25 | 5.9161 | $(4.7458+0.4328i)\pm(0.0067+0.0075\text{i})$ | $0.8055\pm0.0011$ |
| 1.50 | 5.9161 | $(4.7176+0.6097i)\pm(0.0054+0.0062\text{i})$ | $0.8041\pm0.0010$ |
| 1.75 | 5.9161 | $(4.6612+0.8108i)\pm(0.0095+0.0057\text{i})$ | $0.7997\pm0.0017$ |
| 2.00 | 5.9161 | $(4.5943+1.0495i)\pm(0.0089+0.0119\text{i})$ | $0.7966\pm0.0016$ |

Table 4.1: The efficiency of the state transfer protocol as defined in Eq. (4.23), for different coupling strengths $G$ with instantaneous transfer field switching. These values are obtained from positive P simulations.

We obtain numerical results for the state transfer energy efficiencies for different coupling strengths using both the truncated Wigner and positive P representations. The numerical results are shown in Table 4.1 and Table 4.2. They are obtained by solving the dimensionless form of stochastic differential equations given in Eq. (3.28) and Eq. (3.33) for the truncated Wigner and positive P representations, respectively, with the time dependent input field $E(\tau)$ as described in Eq. (4.13). The integrated input is

$$A_{in} = \int_{-\infty}^{0} u_{in}^{*}(\tau)\left[E(\tau)+\alpha_{ext}^{in}\right]d\tau, \tag{4.24}$$

where $u_{in}(\tau)$ is defined in Eq. (4.14) and $\alpha_{ext}^{in}$ is thermal Gaussian noise. The integrated output is given by

$$A_{out} = \int_{\tau_s}^{\infty} u_{out}^{*}(\tau)\,\alpha_{out}(\tau)\,d\tau. \tag{4.25}$$

Here, the temporal output mode function $u_{out}(\tau) = u_{in}^{*}(\tau_s-\tau)$ and the dimensionless output field $\alpha_{out}(\tau)$ is obtained from the input-output relation given in Eq. (3.31).

These numerical results are compared with the analytical result given in Eq. (4.11) in Fig. 4.7. The analytical results plotted here are the first term in Eq. (4.11), ignoring the additional noise term. The

| G | Integrated input, $A_{in}$ | Integrated output, $A_{out}$ | $\zeta_{instant} \equiv \frac{\lvert A_{out}\rvert}{\lvert A_{in}\rvert}$ |
|---|---|---|---|
| 0.50 | $(5.9146-0.0025i)\pm(0.0023+0.0025i)$ | $(4.7675+0.0939i)\pm(0.0028+0.0022i)$ | $0.8062\pm0.0002$ |
| 0.75 | $(5.9160+0.0010i)\pm(0.0020+0.0021i)$ | $(4.7651+0.1768i)\pm(0.0033+0.0026i)$ | $0.8060\pm0.0003$ |
| 1.00 | $(5.9169+0.0006i)\pm(0.0017+0.0024i)$ | $(4.7576+0.2896i)\pm(0.0028+0.0030i)$ | $0.8056\pm0.0003$ |
| 1.25 | $(5.9152+0.0007i)\pm(0.0026+0.0016i)$ | $(4.7431+0.4349i)\pm(0.0028+0.0021i)$ | $0.8052\pm0.0002$ |
| 1.50 | $(5.9167-0.0008i)\pm(0.0015+0.0027i)$ | $(4.7119+0.6098i)\pm(0.0034+0.0034i)$ | $0.8030\pm0.0003$ |
| 1.75 | $(5.9167+0.0013i)\pm(0.0025+0.0018i)$ | $(4.6669+0.8135i)\pm(0.0040+0.0029i)$ | $0.8007\pm0.0004$ |
| 2.00 | $(5.9139+0.0003i)\pm(0.0021+0.0023i)$ | $(4.5996+1.0445i)\pm(0.0021+0.0034i)$ | $0.7976\pm0.0002$ |

Table 4.2: The efficiency of the state transfer protocol as defined in Eq. (4.23), for different coupling strengths $G$ with instantaneous transfer field switching. These values are obtained from truncated Wigner simulations.

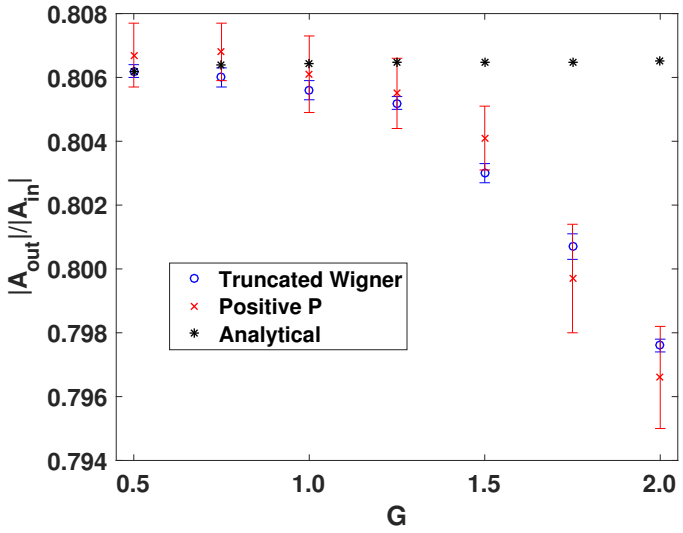


Figure 4.7: The efficiency of the state transfer protocol for different coupling strengths $G$. The number of samples taken for both the truncated Wigner and positive P simulations is $10^5$. The error bars denote the sampling errors in our phase space simulations. For a coherent state with a coherent amplitude of 5, using the given experimental parameter values, the corresponding dimensionless $G$ is 0.006. This puts the experiment well in the regime where the linearisation approximation holds.

errors in the error bars in Fig. 4.7 include both the sampling error and time step error. The main source of error is the sampling error.

It can be easily seen from the tables and figures that the two types of numerical simulation generate very similar results up to the numerical sampling error. The Wigner truncation error is negligible for these calculations, even though the coherent signal amplitude is not very large. However, the analytical predictions using linearization give large errors for $G > 1$.

### 4.3.5 Finite switching time

The state transfer protocol with minimal degradation relies on having the optimal, enhanced coupling strength $G = g_0\sqrt{N}/\gamma_o$, where $N$ is determined by the transfer field amplitude as in Eq. (4.12). In practice, it takes time to switch the transfer field to its required amplitude. Hence, the efficiency of the state transfer protocol defined in Eq. (4.23) depends on how fast the transfer field can be turned on and off. Within the linearised approximation, the finite switching time of the transfer field cannot be easily taken into account. A full, nonlinear simulation then becomes both more accurate and simpler to carry out. We run the same numerical simulations as in the Section 4.3.4, except that the transfer field is now time dependent, to take into account the finite switching of the field. We model the finite transfer field switching with a smoothing function as follows:

$$E_{trans}(\tau) = \begin{cases} E_{trans}\cos^2\left[\frac{(\tau-\tau_1)}{\tau_1+\tau_w}\frac{\pi}{2}\right] & , -\tau_w \le \tau \le \tau_1 \\ E_{trans} & , \quad \tau_1 \le \tau \le \tau_2 \\ E_{trans}\cos^2\left[\frac{(\tau_2-\tau)}{\tau_2}\frac{\pi}{2}\right] & , \quad \tau_2 \le \tau \le 0 \\ 0 & , \quad 0 \le \tau \le \tau_s \\ E_{trans}\cos^2\left[\frac{(\tau_r-\tau)}{\tau_r-\tau_3}\frac{\pi}{2}\right] & , \quad \tau_s \le \tau \le \tau_3 \\ E_{trans} & , \quad \tau_3 \le \tau \le \tau_r. \end{cases} \tag{4.26}$$

Here, $E_{trans}(\tau)$ is the time dependent transfer field and its constant amplitude $E_{trans} = \sqrt{(\Omega_m^2+\Gamma_o^2)N/(2\Gamma_{ext})}$. $\tau_w$ is the length of the writing stage, $\tau_1$ is the time when the writing stage transfer field is fully turned on, $\tau_2$ is the time when the writing stage transfer field starts to turn off, $\tau_3$ is the time we start turning on the read-out stage transfer field, $\tau_4$ is when the read-out stage transfer field is fully turned on and $\tau_r$ is the length of the read-out stage. As described in Section 4.2.2, the duration of the writing stage is the real

| G | Integrated input, $A_{in}$ | Integrated output, $A_{out}$ | $\zeta_{finite} \equiv \frac{\lvert A_{out}\rvert}{\lvert A_{in}\rvert}$ |
|---|---|---|---|
| 0.50 | 5.9161 | $(4.7561+0.1106i) \pm (0.0053+0.0048i)$ | $0.8041 \pm 0.0008$ |
| 0.75 | 5.9161 | $(4.7515+0.1951i) \pm (0.0068+0.0077i)$ | $0.8038 \pm 0.0010$ |
| 1.00 | 5.9161 | $(4.7124+0.2773i) \pm (0.0047+0.0041i)$ | $0.7979 \pm 0.0008$ |
| 1.25 | 5.9161 | $(4.6761+0.4056i) \pm (0.0067+0.0056i)$ | $0.7934 \pm 0.0010$ |
| 1.50 | 5.9161 | $(4.6300+0.5759i) \pm (0.0058+0.0068i)$ | $0.7886 \pm 0.0010$ |
| 1.75 | 5.9161 | $(4.5441+0.7632i) \pm (0.0044+0.0074i)$ | $0.7788 \pm 0.0009$ |
| 2.00 | 5.9161 | $(4.4531+0.9661i) \pm (0.0079+0.0068i)$ | $0.7702 \pm 0.0013$ |

Table 4.3: The efficiency of the state transfer protocol as the ratio between the integrated output $A_{out}$ and integrated input $A_{in}$. These are computed for different coupling strengths $G$ with finite transfer field switching time. These values are obtained from positive P simulations.

| G | Integrated input, $A_{in}$ | Integrated output, $A_{out}$ | $\zeta_{finite} \equiv \frac{\lvert A_{out}\rvert}{\lvert A_{in}\rvert}$ |
|---|---|---|---|
| 0.50 | $(5.9146-0.0025i) \pm (0.0023+0.0025i)$ | $(4.7566+0.0957i) \pm (0.0028+0.0022i)$ | $0.8044 \pm 0.0002$ |
| 0.75 | $(5.9160+0.0010i) \pm (0.0020+0.0021i)$ | $(4.7409+0.1781i) \pm (0.0031+0.0026i)$ | $0.8019 \pm 0.0003$ |
| 1.00 | $(5.9169+0.0006i) \pm (0.0017+0.0024i)$ | $(4.7149+0.2860i) \pm (0.0028+0.0030i)$ | $0.7983 \pm 0.0003$ |
| 1.25 | $(5.9152+0.0007i) \pm (0.0026+0.0016i)$ | $(4.6777+0.4226i) \pm (0.0028+0.0022i)$ | $0.7940 \pm 0.0002$ |
| 1.50 | $(5.9167-0.0008i) \pm (0.0015+0.0027i)$ | $(4.6205+0.5837i) \pm (0.0029+0.0034i)$ | $0.7871 \pm 0.0004$ |
| 1.75 | $(5.9167+0.0013i) \pm (0.0025+0.0018i)$ | $(4.5485+0.7684i) \pm (0.0039+0.0026i)$ | $0.7797 \pm 0.0004$ |
| 2.00 | $(5.9139+0.0003i) \pm (0.0021+0.0023i)$ | $(4.4532+0.9747i) \pm (0.0021+0.0035i)$ | $0.7708 \pm 0.0002$ |

Table 4.4: The efficiency of the state transfer protocol as the ratio between the integrated output $A_{out}$ and integrated input $A_{in}$. These are computed for different coupling strengths $G$ with finite transfer field switching time. These values are obtained from truncated Wigner simulations.

part of $1/(K_+ - M)$, where $K_+ = (\Gamma_o + \Gamma_m)/2$, $K_- = (\Gamma_o - \Gamma_m)/2$, $\Gamma_m = \gamma_m/\gamma_o$ and $M = \sqrt{K_-^2 - G^2}$.

We choose the switching time to be 1% of the duration of the writing stage. The resulting efficiencies are shown in Table 4.3 and Table 4.4. The reduced efficiency in percentage relative to the efficiency with instantaneous switching is defined as

$$\zeta_{reduced} = \frac{\zeta_{finite} - \zeta_{instant}}{\zeta_{instant}} \times 100\%\,, \tag{4.27}$$

where $\zeta_{finite}$ is the efficiency, taking the finite transfer field switching into account. The results are plotted in Fig. 4.8.

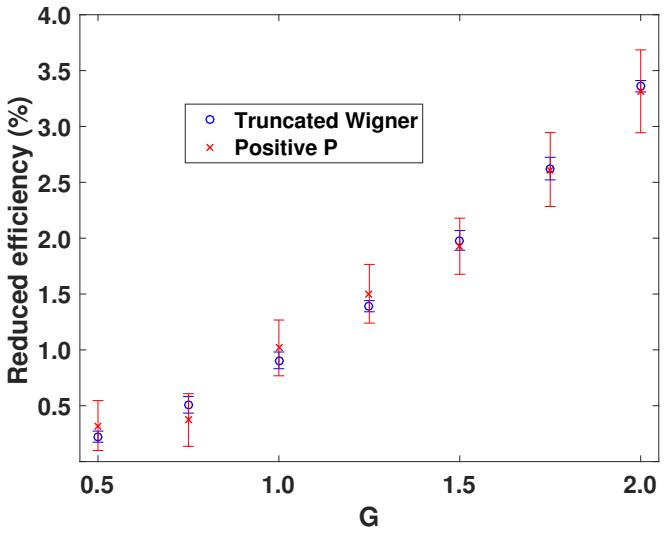


Figure 4.8: The reduced efficiency of the state transfer protocol due to finite switching for different coupling strengths $G$. The number of samples taken for both the truncated Wigner and positive P simulations is $10^5$. The error bars denote the sampling errors in our phase space simulations.

### 4.3.6 Quantum fidelity

In this section, we compute the quantum fidelity in the truncated Wigner representation. We note that the quantum fidelity computation in the positive P representation is nontrivial as the sampling error can be very large [163]. It was observed by Rosales-Zarate and Drummond [163] that a generalized Gaussian phase space representation is more suited in computing the quantum fidelity exactly.

The quantum fidelity is defined as

$$F = \mathrm{Tr}\left(\rho_i \rho_f\right), \tag{4.28}$$

where $\rho_i$ is the density operator of the stored quantum state and $\rho_f$ is the density operator of the retrieved quantum state. The fidelity (4.28) is just the overlap between two pure quantum states, if one of the density operators characterises a pure state. This is the case in our consideration where we take the stored quantum state $\rho_i$ to be pure. The quantum fidelity in the truncated Wigner representation is given by [164, 165]

$$F = \pi \int W_i(\alpha) W_f(\alpha)\, d^2\alpha\,. \tag{4.29}$$

| G | Fidelity, F |
|---|---|
| 0.50 | $0.2772 \pm 0.0012$ |
| 0.75 | $0.2702 \pm 0.0015$ |
| 1.00 | $0.2553 \pm 0.0014$ |
| 1.25 | $0.2276 \pm 0.0013$ |
| 1.50 | $0.1847 \pm 0.0016$ |
| 1.75 | $0.1325 \pm 0.0014$ |
| 2.00 | $0.0820 \pm 0.0008$ |

Table 4.5: The fidelity of the optomechanical state transfer protocol with instantaneous transfer field switching. These values are obtained from truncated Wigner simulations.

| G | Fidelity, F |
|---|---|
| 0.50 | $0.2716 \pm 0.0013$ |
| 0.75 | $0.2585 \pm 0.0015$ |
| 1.00 | $0.2359 \pm 0.0012$ |
| 1.25 | $0.2028 \pm 0.0014$ |
| 1.50 | $0.1578 \pm 0.0012$ |
| 1.75 | $0.1098 \pm 0.0014$ |
| 2.00 | $0.0665 \pm 0.0006$ |

Table 4.6: The fidelity of the optomechanical state transfer protocol with finite transfer field switching time as described in Section 4.3.5. The fidelity is lower compared to the case of instantaneous transfer field switching. These values are obtained from truncated Wigner simulations.

Here, $W_i(\alpha)$ and $W_f(\alpha)$ are the corresponding Wigner functions for $\rho_i$ and $\rho_f$ respectively. The derivation of the fidelity expression in Eq. (4.29) can be found in Appendix E. In particular, for a coherent state $|\alpha_0\rangle$, the corresponding Wigner function is given by

$$W(\alpha) = \frac{2}{\pi}\exp\left(-2|\alpha-\alpha_0|^2\right). \tag{4.30}$$

| $\mathbf{N_c}$ | $\mathbf{F}$ | $\mathbf{F_{pure}}$ | $\mathbf{F_{min}}$ |
|---|---|---|---|
| 1 | $0.7694 \pm 0.0027$ | 0.9641 | 0.6667 |
| 5 | $0.6825 \pm 0.0026$ | 0.8329 | 0.5455 |
| 15 | $0.5055 \pm 0.0019$ | 0.5779 | 0.5161 |
| 25 | $0.3743 \pm 0.0016$ | 0.4009 | 0.5098 |
| 35 | $0.2772 \pm 0.0012$ | 0.2782 | 0.5070 |

Table 4.7: Fidelities for different number of photons. Here, $N_c$ is the mean photon number of the corresponding coherent state one wishes to store. Fidelities $F$ are obtained from truncated Wigner simulations. These are compared with the corresponding fidelities as given in Eq. (4.33) and also the minimum fidelities required for claiming a quantum memory for a coherent state, as in Eq. (4.32).

The quantum fidelity can then be computed using the Monte Carlo method as follows:

$$\begin{aligned} F &= \pi \int W_i(\alpha) W_f(\alpha)\, d^2\alpha \\ &\approx \frac{\pi}{N_{sample}} \sum_{j=1}^{N_{sample}} W_i(\alpha_j) \\ &= \frac{2}{N_{sample}} \sum_{j=1}^{N_{sample}} \exp\left(-2|\alpha_j - \alpha_0|^2\right) . \end{aligned} \tag{4.31}$$

We can think of the first line in Eq. (4.31) as the expectation value of $W_i(\alpha)$ with the probability distribution $W_f(\alpha)$. The Monte Carlo method comes in the second line, where instead of the probability distribution $W_f(\alpha)$, we have a set of sampled values of $\alpha$ from the distribution $W_f(\alpha)$. We use the expression for $W_i$ as in Eq. (4.30) in the final line.

The fidelity for different coupling strengths is tabulated in Table 4.5. The fidelity, taking into account the effect of finite transfer field switching time, is shown in Table 4.6. The results show a decrease in fidelity when the transfer field takes a finite time to turn on and off, compared to the case where transfer field is assumed to be switched instantaneously. This is expected since the efficiency of the state transfer protocol as defined in Eq. (4.23) is reduced in the case of finite transfer field switching time.

Hammerer et al. [166] and Braunstein et al. [28] computed the minimum fidelity $F_{min}$ required for a quantum memory and it is given by

$$F \geq \frac{(1+N_c)}{(2N_c+1)} \equiv F_{min}\,, \tag{4.32}$$

where $N_c$ is the mean photon number of the quantum state one wishes to store. The criterion in Eq. (4.32) provides a benchmark for the quantum memory of a coherent state. Assuming that both the input and output states are pure coherent states with amplitudes $\alpha_0$ and $\eta\alpha_0$ respectively, the quantum fidelity of the coherent output state $|\eta\alpha_0\rangle$ with respect to the coherent input state $|\alpha_0\rangle$ is given by

$$F_{pure} = |\langle\eta\alpha_0|\alpha_0\rangle|^2 = \exp\left[-|\alpha_0(1-\eta)|^2\right]. \tag{4.33}$$

Here $\eta = 0.8088$, as quoted in the experiment by Palomaki et al. [59].

As suggested by Eq. (4.32) and Eq. (4.33), the state transfer protocol fidelity and its minimum value required for a quantum memory of a coherent state depends on the mean photon number of the coherent state. We computed the fidelities $F$ for coherent states with mean photon number $1, 5, 15, 25$ and 35, for $G = 0.5$ with instantaneous transfer field switching. They are carried out in the truncated Wigner representation. These fidelities are then compared to $F_{min}$ and $F_{pure}$ predicted by Eq. (4.32) and Eq. (4.33), respectively, as shown in Table 4.7. From the table, we see that $F_{pure}$ is quantitatively different from fidelity $F$ computed numerically. The discrepancies increase with smaller mean photon numbers of the corresponding coherent states. This is because a coherent state with small mean photon number is more susceptible to noise from the environment and hence the assumption that the output state is a pure coherent state is invalid.

On the other hand, the fidelities for coherent states with smaller mean photon numbers are increased to the point that they do exceed $F_{min}$. For these cases, a genuine quantum optomechanical memory of a coherent state can be achieved. For larger mean photon numbers the fidelity is reduced, since the losses will lead to a substantial probability of an output state with a different photon number, that is therefore orthogonal to the input. In these cases, the predicted fidelity is lower than that required by the criterion in Eq. (4.32). In order to achieve quantum state transfer, either the stored photon number of the internal cavity losses and thermal noises on mechanical oscillator have to be significantly reduced compared to a recent experiment on coherent state transfer.

## 4.4 Summary

Based on the fact that quantum state transfer can be achieved in an optomechanical system with a red-detuned field, we analysed a specific optomechanical state transfer protocol using two fields. One field (the preparation field) is used to generate the optical quantum state in a cavity while the other (the

transfer field) facilitates the transfer of this quantum state between the optical and mechanical modes. We analysed a linearised quantum memory model to demonstrate mode-matching for optimal coupling of the field into the cavity. This is achieved by choosing a specific temporal mode function for the preparation field.

The scheme presented in this chapter relies on the temporal mode-matching for a fixed coupling strength. More often, one wants to transfer a state that has a specific temporal mode. When this is the case, the coupling strength can be made time dependent that still ensures an optimal coupling of the state into the optomechanical system. This is done by making the transfer field time dependent. The theoretical work on this can be found in the paper of He et al. [150].

We then presented numerical phase space simulation results in the truncated Wigner and positive P representations. We computed the power spectral densities for the output fields from the optical cavity and observed the spectral content overlap between the control and signal fields. Removal of the control field is then required for signal extraction and we discussed the procedure of removing the control field amplitude in the time domain. The full, nonlinear simulations demonstrate that for stronger optomechanical coupling strengths, nonlinearity of the system cannot be neglected and the linearisation approximation breaks down.

Finally, we presented fidelity as a more suitable measure to quantify the efficiency of a quantum memory. We showed that either the use of coherent states with smaller photon numbers or improvements in the quality factor of the cavity and mechanical systems are necessary to increase the fidelity beyond the threshold required for a quantum memory.

We should mention the progress in achieving optomechanical quantum memory in the electromechanical implementation, where the experimental parameters are used in our numerical simulations. In the earliest work on optomechanical memory in an electromechanical system, Palomaki et al. [59] used a fixed coupling strength and specific temporal mode function for optimal coupling of the state into their electromechanical system. In that work, a coherent state was transferred. A coherent state is a Gaussian state, and it can be treated essentially as a classical state as its statistics can be simulated using a classical computer. The optomechanical quantum memory of highly nonclassical states such as the Schrodinger's cat or Fock states is challenging due to thermal noises from the environment and also the experimental challenges in characterising these quantum states. In a recent work by Reeds et al. [167] using the same electromechanical implementation, a quantum state in a quantum superposition of zero and one photon was transferred to and then read-out from their electromechanical system.

The state tomography were then carried out to infer both the density operator of the input and stored quantum states. This allows them to compute the fidelity, which is essential for a quantum memory. As experimental techniques advance, an optomechanical quantum memory of any arbitrary quantum states is very much feasible in the near future.

The publication relevant to this chapter is:

- R. Y. Teh, S. Kiesewetter, M. D. Reid, and P. D. Drummond, *Simulation of an optomechanical quantum memory in the nonlinear regime*, Phys. Rev. A **96**, 013854 (2017).

# Chapter 5

# Creating quantum entanglement between two optomechanical systems: a pulsed scheme

Quantum entanglement between the optical cavity and mechanical modes in an optomechanical system can be generated by applying a blue-detuned pump field as described in Chapter 3.2. This has been achieved, for instance, in the electromechanical experiment [62]. Theoretically, the use of phase space methods in investigating quantum entanglement in optomechanical systems first appeared in the work of Kiesewetter et al. [137]. In that work, the cavity and mechanical modes in an optomechanical system are entangled and the entanglement is certified by a criterion similar to those presented in Chapter 1. In this chapter, we extend this to quantum entanglement between two optomechanical systems, which resulted in a recently published paper by Kiesewetter et al. [168].

One motivation for this is to explore and discover alternative decay mechanisms of quantum correlations. Quantum correlations are known to be very fragile, especially in macroscopic systems. The most accepted explanation for the absence of quantum effects in macroscopic systems is decoherence due to interaction of these systems with their environment. In the conventional quantum mechanics, quantum correlations between two systems, in the ideal case, should remain correlated whether they are in the same room or in the opposite ends of the universe. This is true even for macroscopic systems. However, it is conceivable that there might be other mechanisms that can destroy quantum correlations in a system even if that system is well isolated from its environment. In fact, there are a couple

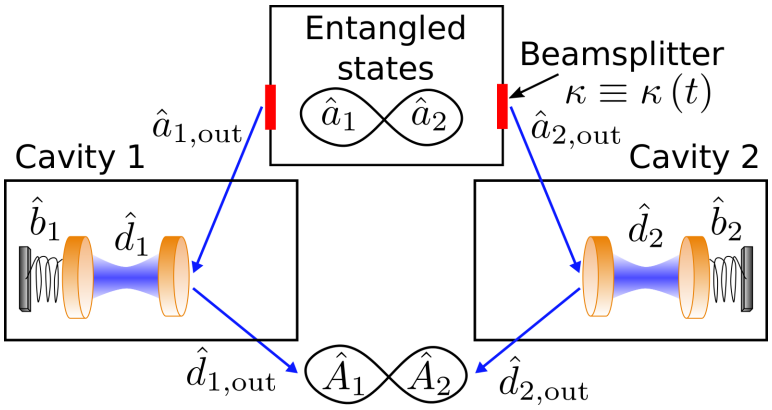


Figure 5.1: Schematic diagram of entanglement protocol.

of models [169–171] that consider this possibility and one of them is Furry's hypothesis [74]. This model concerns the decay of quantum correlations as a function of spatial separation. We know that the Furry's hypothesis is ruled out in the case of massless particles [2–4]: Entangled photons do not decay with spatial separation. However, no experiments thus far involving entanglement in center-of-mass motion in massive systems have been carried out to check against the Furry's hypothesis. Obviously, explicit decoherence models with spatial separation dependence are needed to predict any deviations from the standard decoherence model due to interaction of the quantum system with its environment. These Furry-type decoherence models [172] are being considered and they would predict different entanglement results as we will present in this chapter. This allows Furry's hypothesis to be tested.

In this chapter, we describe and analyse a proposal to generate quantum entanglement between two spatially separated quantum optomechanical systems. This proposal involves well established techniques in creating and transferring entanglement in optomechanical systems. The numerical results in this chapter are obtained from the linearised stochastic differential equations in the truncated Wigner representation. As we have seen in Chapter 4, in the weak coupling regime, the linearised, truncated Wigner simulation results agree well with the full, nonlinear truncated Wigner simulation results. All results in this chapter are in this weak coupling regime.

## 5.1 Proposal of quantum entanglement generation

In this section, we describe the protocol used to generate quantum entanglement between two spatially separated optomechanical system. The schematic depiction of the protocol is shown in Fig. 5.1.

The two mode squeezed state is first generated using the nondegenerate parametric down conversion. These entangled modes $a_1$ and $a_2$ are then subsequently sent into two spatially separated optomechanical systems, labelled Cavity 1 and Cavity 2, respectively. Using the quantum optomechanical state transfer technique described in Chapter 4, these entangled modes $a_1$ and $a_2$ are transferred to their corresponding mechanical modes $b_1$ and $b_2$. In other words, we now have two massive systems that are entangled with each other. Finally, we measure the quadratures of these mechanical modes and confirm that they are entangled using an entanglement criterion.

In the following, we elaborate each of these steps in detail. Let's first discuss the standard entanglement generation with the parametric down conversion process. As described in Chapter 1, the two mode squeezed state is created by pumping continuous wave laser field into a nonlinear optical medium that is placed in a cavity. We name this the source cavity to avoid the possible confusion of mixing up with the cavity in the optomechanical system. The two outputs from the source cavity are correlated and the degree of correlations are characterised by the squeezing parameter $r$ that depends on the strength and power of the pump field. The subsequent steps are more involved and they are described in separate subsections for clarity.

### 5.1.1 Transfer of entangled modes from source cavity to optomechanical system

Next, we move on to the transfer of these entangled modes into two spatially separated optomechanical systems. In particular, these two modes are pulses rather than continuous wave fields. Depending on the experimental implementation of the optomechanical system, the techniques and methods required to send these pulses from the source cavity into the optomechanical cavities differ. For instance, we envisage a low loss optical fiber which is connected between the source and optomechanical cavities. In practice, there will inevitably be losses in the transfer process. These losses can be modelled by a beam splitter sitting between the source and optomechanical cavities, with the transmissivity characterises the efficiency of the transfer. Losses during this transfer process are neglected in our theoretical analysis.

In order to maximise the coupling between these entangled pulses into their corresponding cavities in the optomechanical systems, their temporal mode functions have to match that of the cavities. In this chapter, we choose to feed symmetric pulses into the optomechanical systems. The shape of these output pulses from the source cavity can be modulated by changing the decay rate of the source cavity as a function of time. This is the cavity Q-switching method [173]. Other methods such as the time-dependent cavity detuning are possible and could be more practical experimentally [150, 174]. There

is, however, no significant difference in the theoretical analyses for both of these methods [150]. Here, we adopt the conceptually simpler Q-switching method.

Once the symmetric pulse is in the cavity of the optomechanical system, this pulse has to be transferred from the cavity mode to the mechanical mode. Recall from Chapter 3 that a red-detuned pump facilitates the state transfer between the cavity and mechanical modes in an optomechanical system. In the following, we analyse what is required of the red-detuned pump in order to transfer a symmetric pulse. Let's first express the time evolution of the source cavity mode $a_k$, where $k = 1,2$ denotes the two output modes in the source cavity from a parametric down conversion process:

$$\dot{a}_k = -\kappa(\tau)\, a_k + \sqrt{2\kappa(\tau)} a_{k,\text{in}} \tag{5.1}$$

Here, $\kappa(\tau)$ is the time dependent decay rate of the source cavity and $a_{k,in}$ is any input into the source cavity, including thermal noises. We neglect thermal noises into the source cavity to simplify our analytical analysis. Also, the source cavity satisfies the input-output relation that relates the source cavity mode $a_k$ and both the input $a_{k,in}$ and output $a_{k,out}$ modes of the source cavity:

$$a_{k,\text{out}} = \sqrt{2\kappa(\tau)} a_k - a_{k,\text{in}}. \tag{5.2}$$

Suppose that we wish to generate output mode with a pulse shape that is symmetric in time of the form $a_{k,out} \propto \text{sech}(\tau)$. It can be shown that this can be achieved by setting $\kappa(\tau) = [1 + \tanh(\tau)]/2$. We verify this by solving for Eq. (5.1), the source cavity and the corresponding output modes are

$$\begin{aligned} a_k &= a_k(-\infty) \sqrt{\left[\frac{1-\tanh(\tau)}{2}\right]} + a_{vac} \\ a_{k,out} &= \frac{a(-\infty)}{\sqrt{2}} \text{sech}(\tau) + a'_{vac}, \end{aligned} \tag{5.3}$$

where $a_{\text{vac}}$, $a'_{\text{vac}}$ are the input and output vacuum noises of the source cavity, respectively.

#### 5.1.1.1 Time dependent optomechanical coupling strength

Next, we see how these symmetric output pulses from the source cavity can be transferred into optomechanical systems by having a time dependent optomechanical coupling strength. The time evolution

equations of the cavity and mechanical modes in the optomechanical system are given by:

$$\begin{aligned} \dot{d}_k &= -d_k - ig(\tau) b_k + \sqrt{2} d_{k,\text{in}} \\ \dot{b}_k &= -ig(\tau) d_k . \end{aligned} \tag{5.4}$$

Here, $d_k$ and $b_k$ are the optomechanical cavity and mechanical modes respectively, $d_{k,in}$ is the input mode into the optomechanical cavity. In this scheme, $d_{k,in} = a_{k,out}$: the output pulse from the source cavity is the input into the optomechanical cavity, with no degradation and loss. The optomechanical cavity satisfies the input-output relation $d_{k,out} = \sqrt{2} d_k - d_{k,in}$. Also, for the linearised analytical analysis, we drop the dissipation and noise terms in the time evolution equation for the mechanical mode in Eq. (5.4). These terms are present in our numerical simulations.

To this end, we are ready to find the optimal time dependent optomechanical coupling strength $g(\tau)$ for optimal coupling and transfer of the source cavity output pulse into an optomechanical system. For an optimal coupling and transfer, the output of the optomechanical system should be zero during the transfer process. This implies, from the input-output relation, that $d_{k,in} = \sqrt{2} d_k$, giving $\dot{d}_k = d_k - ig(\tau) b_k$. Also, it follows from the time evolution equation of the mechanical mode $b_k$ that $-ig(\tau) = \dot{b_k}/d_k$. Putting all these together, we re-express the time evolution equation of the cavity mode $d_k$:

$$\left(\dot{d}_k + igb_k\right)/d_k = \dot{d}_k/d_k - \left(\dot{b}^2\right)/\left(2d_k^2\right) = 1 . \tag{5.5}$$

We note that $d_k = a(-\infty)\,\text{sech}(\tau - \tau_1)/2$, where $\tau_1$ is the time where the pulse shape reaches its peak. The task is to solve for $b_k$ from $\dot{d}_k/d_k - \left(\dot{b}^2\right)/\left(2d_k^2\right) = 1$ from Eq. (5.5) and then obtain the time dependent coupling strength $g$ from $-ig(\tau) = \dot{b_k}/d_k$. One can verify that $b_k = ia(-\infty)\left[1 + \tanh(\tau - \tau_1)\right]/2$ is the solution of $\dot{d}_k/d_k - \left(\dot{b}^2\right)/\left(2d_k^2\right) = 1$. The time-dependent coupling strength $g$ is then $g(\tau) = -\text{sech}(\tau - \tau_1)$. This analysis gives us $g(\tau)$ for the symmetric pulse to enter the cavity and be transferred to the mechanical mode. The coupling strength $g(\tau)$ for transfer of mechanical mode back into the cavity is identical apart from a different peak time.

**Remark**: It is worth pointing out the difference between the coupling and optomechanical transfer of this entanglement protocol and the state transfer protocol in Chapter 4. In the optomechanical state transfer protocol, the coupling strength is fixed and the pulse sent into the cavity has to have a temporal mode function that matches to that of the cavity, for optimal coupling, while in the entanglement protocol, we want the pulse to have a certain temporal mode function and the coupling strength $g$ in

turn has to be tuned to allow optimal coupling and state transfer.

### 5.1.2 Two-optomechanical system quantum entanglement verification

#### 5.1.2.1 Temporal mode function and optomechanical output modes

These optomechanical mechanical modes are stored for a time $\tau_s$. After that, these modes will be transferred back from the mechanical to the optomechanical cavity mode, and subsequently be detected. In order to measure the state stored in the mechanical mode, the output mode from the optomechanical system has to be integrated with time. In particular, we measure the integrated output from the optomechanical system. The procedure for measuring the integrated output is identical to the one explained in Section 4.2.2 of Chapter 4. The only difference is the temporal mode function used, since the pulses used are different in both optomechanical quantum protocols.

Since the input pulse into the optomechanical system from the source cavity has the form $\hat{a}_{k,\text{out}} \propto \text{sech}(\tau)$, the input temporal mode function for the optomechanical cavity input is $u_{in}(\tau) = N\text{sech}(\tau)$, where $N$ is the normalisation factor such that $\int |u_{in}(\tau)|^2 \, d\tau = 1$, and $N$ is given by

$$N = 1/\sqrt{\int_{-\infty}^{\infty} \text{sech}(\tau)^2 \, d\tau} = \sqrt{\frac{1}{2}}. \tag{5.6}$$

The integrated output is then:

$$A_{k,out} = \int_{\tau_1+\tau_s/2}^{\tau_{max}} u_{out}(\tau)\, d_{k,out}(\tau)\, d\tau, \tag{5.7}$$

where $u_{out}(\tau) = u_{in}(\tau - (\tau_1 + \tau_s/2))$. Note that the integration in Eq. (5.7) begins after the first transfer pulse has been completed. These integrated outputs are necessary to certify the quantum entanglement between the two optomechanical systems.

To certify quantum entanglement in these systems, we use an entanglement criterion similar to those presented in Chapter 1 [175]:

$$\Delta^p_{ent} = \frac{4\Delta\left(X_1 - GX_2^\theta\right)\Delta\left(P_1 + GP_2^\theta\right)}{(1+G^2)} > 1, \tag{5.8}$$

where $X_k^\theta = \frac{1}{2}\left[e^{-i\theta}A_{k,\text{out}} + e^{i\theta}A^\dagger_{k,\text{out}}\right]$, $P_k^\theta = X_k^{\theta+\pi/2}$ and $G$ is the gain and it is an adjustable real constant. When the inequality in Eq. (5.8) is violated, it implies the existence of entanglement between

the two optomechanical systems. In order to minimise the value of $\Delta^{p}_{ent}$ and maximise the violation of the inequality in Eq. (5.8), we find the optimal phase $\theta$ and gain $G$. These are obtained using the same method as presented in Chapter 1.

## 5.2 Numerical simulations and results

### 5.2.1 Experimental parameters

In this two-optomechanical systems entanglement protocol, we used experimental parameters similar to the optomechanical experiment of Chan et al. [50]. The initial average thermal occupation number for the mechanical modes are $n_{th,b}(0) = 0.7$. The cavity resonance frequency $\omega_c/2\pi = 195\,\text{THz}$ with a decay rate $\gamma_c/2\pi = 0.26\,\text{GHz}$; while the mechanical oscillator has a resonance frequency $\omega_m/2\pi = 3.68\,\text{GHz}$, with a mechanical dissipation rate of $\gamma_m/2\pi = 35\,\text{kHz}$. The bare optomechanical coupling strength is $g_0/2\pi = 0.91\,\text{MHz}$, which justifies the linearisation [61, 176] and adiabatic approximations [60].

### 5.2.2 Numerical methods

Numerical phase space simulations are carried out as described in Chapter 3. Here, we list down the stochastic differential equations dictating the time evolutions of the source cavity $\alpha_k$, optomechanical cavity $\delta_k$ and mechanical $\beta_k$ modes in the truncated Wigner representation. We note that dimensionless units are now used in all subsequent analyses, where all parameters with the unit of frequency are scaled with respect to the cavity decay rate $\gamma_c$. These stochastic differential equations were derived by Simon Kiesewetter using the quantum cascaded formalism [177–179] and they are given by:

$$\begin{aligned}
\dot{\alpha}_k &= -\kappa(\tau)\,\alpha_k + \sqrt{2\kappa(\tau)}\xi_k \\
\dot{\delta}_k &= -\delta_k - ig(\tau)\,\beta_k + 2\sqrt{\kappa(\tau)}\alpha_k - \sqrt{2}\xi_k \\
\dot{\beta}_k &= -\gamma_m\beta_k - ig(\tau)\,\delta_k + \sqrt{2\gamma_m\,(2\bar{n}_{\text{th},m}+1)}\xi_{2+k}\,.
\end{aligned} \tag{5.9}$$

Here, $\kappa(\tau) = \frac{1}{2}[1+\tanh(\tau-\tau_1)]$ is the time dependent source cavity decay rate, while the effective coupling strength is

$$g(\tau) = \begin{cases} -\sqrt{2}u(\tau-\tau_1), \forall\, 0 \le \tau \le \tau_1 + \frac{\tau_s}{2} \\ -\sqrt{2}u(\tau-\tau_2), \forall\, \tau_1 + \frac{\tau_s}{2} \le \tau \le \tau_{\max}, \end{cases} \tag{5.10}$$

where $\tau_1 = 8.17$ and $\tau_2 = \tau_1 + \tau_s$ are the dimensionless times when the storing and reading pulses peak, and $\tau_{\max} = 2\tau_1 + \tau_s$, while $\tau_s$ is the dimensionless time between the peaks of the storage and readout pulses. It is also the storage time of the entangled state in the mechanical mode. $\bar{n}_{\mathrm{th},m} = 1/[\exp(\hbar\Gamma_c\omega_m/k_BT) - 1]$ is the average thermal occupation number in the mechanical mode, and $\xi_k$ are complex Gaussian noises with variances that correspond to the 'half-quanta' occupations of symmetric Wigner vacuum correlations, $\langle \xi_k(\tau)\xi_l^*(\tau')\rangle = \frac{1}{2}\delta_{kl}\delta(\tau-\tau')$.

To solve the set of stochastic differential equations in Eq. (5.9), initial states of these modes have to be specified. We assume initial thermal states for both the optomechanical cavity and mechanical modes. On the other hand, the initial state of the source cavity is a two-mode squeezed state. The Wigner distribution for the two-mode squeezed state can be found in the standard quantum optics textbook of Walls et al. [77]. The Wigner distribution for this state is given by

$$W(\alpha_+, \alpha_-, \tau_0) = \frac{4}{\pi^2}\exp\left[-2\left(\frac{|\alpha_+|^2}{e^{2r}} + \frac{|\alpha_-|^2}{e^{-2r}}\right)\right], \tag{5.11}$$

where $\alpha_\pm = (\alpha_1 \pm \alpha_2^*)/\sqrt{2}$ and $r$ is the squeezing parameter that characterizes the degree of entanglement.

Instead of the source cavity modes $\alpha_1$ and $\alpha_2$, $\alpha_\pm$ is used as the variables in the Wigner distribution because the corresponding distribution consists of the product of two Gaussian distributions, which can be sampled straightforwardly. One can sample $\alpha_1, \alpha_2$ by generating Gaussian noise vectors $\xi_x^\pm, \xi_y^\pm$ with unit variance, defining $\alpha_\pm = \left[\xi_x^\pm + i\xi_y^\pm\right]e^{\pm r}/2$ and then obtaining mode amplitudes $\alpha_1 = (\alpha_+ + \alpha_-)/\sqrt{2}$ and $\alpha_2 = \left(\alpha_+^* - \alpha_-^*\right)/\sqrt{2}$.

All numerical results in this chapter are obtained with the linearised, truncated Wigner representation. The software package xSPDE [154] is used to solve the stochastic differential equations with the fourth order Runge-Kutta method in the interaction picture. The number of samples used is $10^4$ with 500 grid points in time. The corresponding time step is much smaller than that required according to the

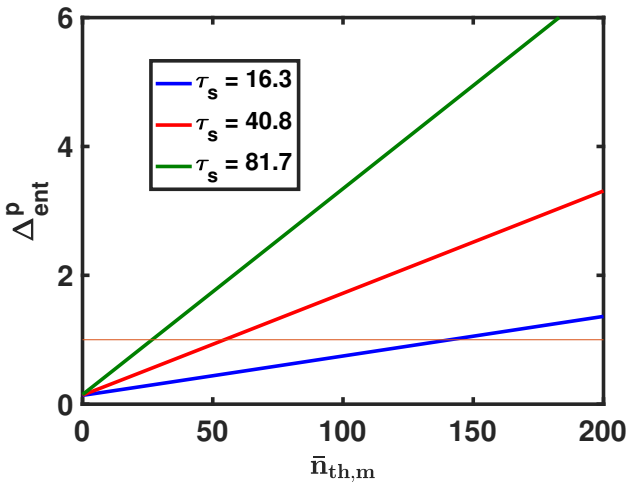


Figure 5.2: Entanglement criterion as a function of thermal occupation number for three different storage times. The results are obtained from phase space simulation in the linearised, truncated Wigner representation.

Shannon sampling theorem [156]. Consequently, both the sampling and time step errors are negligible in the numerical results presented in this chapter.

The full, nonlinear phase space simulations in both the truncated Wigner and positive P representations are carried out by Simon Kiesewetter and the results can be found in the paper by Kiesewetter et al. [168]. At the outset, we state that the numerical results using the linearised, truncated Wigner representation agree with the results using the nonlinear truncated Wigner and positive P representations. This is not surprising, as we have established in Chapter 4 that when the effective coupling strength, relative to the cavity decay rate, is weak, the linearisation approximation is a good one.

### 5.2.3 Entanglement

We compute $\Delta^p_{\text{ent}}$ in Eq. (5.8) as a function of average thermal occupation number for the mechanical modes. These are carried out for a set of three different storage times $\tau_s = 16.3,\ 40.8,\ 81.7$, corresponding to 10 ns, 25 ns and 50 ns, respectively, and a fixed squeezing parameter $r = 1$. To give an approximate analytic prediction, we consider only the degradation of the entanglement during its storage period in the mechanical oscillators. Using results described in [84], we predict an entanglement

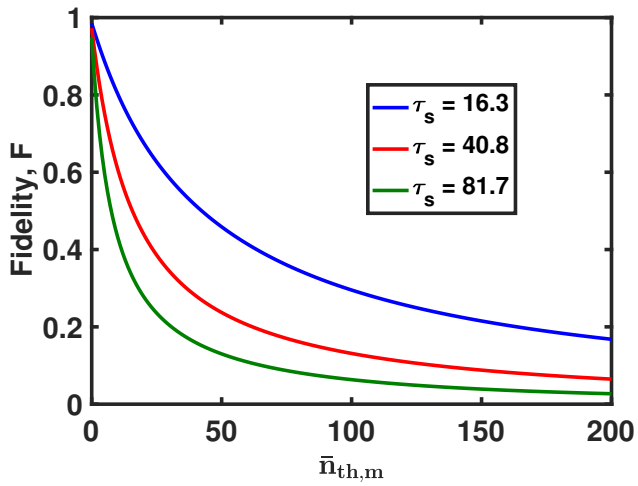


Figure 5.3: Fidelity $F$ as a function of the thermal occupation number and three different storage times.

value of

$$\Delta^{p}_{\text{ent}} = e^{-2\gamma_m \tau_s} e^{-2r} + \left(1 - e^{-2\gamma_m \tau_s}\right)\left(1 + 2\bar{n}_{\text{th},m}\right) . \tag{5.12}$$

Fig. 5.2 shows these numerical results, as compared to the corresponding theoretical predictions given in Eq. (5.12). The solid lines indicate simulation results in the linearised, truncated Wigner representation and dashed lines theoretical predictions. The sampling and time step errors are too small to be observed in the figure.

These chosen storage times are much smaller than the mechanical oscillators' lifetime $1/\gamma_m$, which means that the quantum coherence in the entangled state between the two optomechanical systems are still present. However, the noisy environment destroys the coherence and the entanglement. As cooling techniques are constantly improving and quantum systems are better isolated from their environment, the entanglement protocol proposed here is feasible.

### 5.2.4 Quantum fidelity

It is interesting to find out the efficiency lower bound of the protocol that still allows entanglement to be observed. To quantify the efficiency of the entanglement protocol, we compute the quantum fidelity

of the final output states from the optomechanical systems with respect to the two mode squeezed state generated in the source cavity. The quantum fidelity $F$ as defined in Eq. (4.28) is given by:

$$F = \mathrm{Tr}\left(\rho_i \rho_f\right) , \tag{5.13}$$

where $\rho_i$ is the density operator of the two mode squeezed state and $\rho_f$ is the density operator of the output states from the two optomechanical systems. In the Wigner representation [164, 165], the quantum fidelity is:

$$F = \pi^2 \int W_i\left(\alpha_1, \alpha_2\right) W_f\left(\alpha_1, \alpha_2\right)\, d^2\alpha_1 d^2\alpha_2 , \tag{5.14}$$

which follows from the derivation in Appendix E.

From the quantum simulations, we obtain sampled temporal output modes from the Wigner function $W_f$. The quantum fidelity $F$ is then computed using

$$F = \frac{\pi^2}{N_{\text{sample}}} \sum_m W_i\left(A^m_{1,\text{out}}, A^m_{2,\text{out}}\right) , \tag{5.15}$$

where $A^m_{k,\text{out}}$ is the $m$-th sample of temporal output mode $A_{k,\text{out}}$ and $N_{\text{sample}}$ is the total number of samples taken.

The quantum fidelity in Eq. (5.15) is also computed as a function of average mechanical thermal occupation number and storage time. The result is shown in Fig. 5.3. As expected, for a fixed temperature, longer storage time leads to more losses and hence lower fidelity. Larger mechanical thermal occupation numbers also leads to lower fidelities. More interestingly, by comparing plots in Fig. 5.2 and Fig. 5.3, a fidelity $F$ of at least about 0.3 is needed for entangled output modes.

## 5.3 Summary

This chapter analysed a protocol that aims to entangle two spatially separated optomechanical systems. An entangled two mode squeezed state is generated by the well-established parametric down conversion process in a source cavity. By changing the source cavity decay rate as a function of time, two entangled pulses from the source cavity are sent into two spatially separated optomechanical systems. Detailed explanations for the optimal coupling of these pulses into the optomechanical systems and

the subsequent optomechanical state transfer between the optical and mechanical modes are presented. In order to verify the entanglement in the quadrature amplitudes of these optomechanical systems, we compute an entanglement criterion. The quantum fidelity that measures the "closeness" of the detected physical state to the initial entangled two mode squeezed state is also computed. This entanglement protocol can be implemented, in principle, and the results presented based on the conventional quantum mechanics in this chapter allow alternative decoherence mechanisms to be checked.

The publication relevant to this chapter is:

- S. Kiesewetter, R. Y. Teh, P. D. Drummond, and M. D. Reid, *Pulsed entanglement of two optomechanical oscillators and Furry's hypothesis*, Phys. Rev. Lett. **119**, 023601 (2017).

# Chapter 6

# Conclusion

We discussed the different classes of quantum correlations. In particular, we focused on criteria that certify the presence of genuine multipartite continuous-variable entanglement in a physical state. The advantage of these criteria is that they are not state dependent and only involve statistics of measurable observables, making them more general. Using these criteria, other properties of quantum correlations, such as the monogamy of quantum entanglement, which restricts the shareability of entanglement among different modes in a multimode system, can be studied. Monogamy relations of quantum entanglement were formulated in terms of these criteria. Yet another quantum property is the quantum coherence of quantum states, which is the source of quantum correlations. However, the verification of the presence of the quantum coherence is not trivial.

In the second part of the thesis, we study an optomechanical system, which is a macroscopic system where the traditional, conventional wisdom is that macroscopic systems obey classical physics. However, it has been shown that quantum properties do exhibit in these macroscopic systems, blurring the boundary between classical and quantum physics. We study the quantum properties of a quantum optomechanical system. In particular, two quantum protocols were analysed. These quantum protocols are timely as the technological advancement in the field of optomechanics allow these protocols to be carried out. They allow fundamental issues in quantum mechanics to be addressed. For instance, the classical-quantum boundary problem and alternative decoherence mechanisms of quantum correlations. However, to study the dynamics of an optomechanical system, operator equations that are inherently nonlinear have to be solved. The analytical solutions are generally not possible. A very powerful approach using the phase space methods transform these operator equations into complex number equations, allowing numerical solutions to be obtained.

To simplify the analysis of an optomechanical system, the linearisation approximation is often employed. The argument provided for the validity of this approximation invoked the weak nature of the optomechanical coupling strength. With the phase space methods, the linearisation approximation is not needed which allows the validity of the approximation to be checked. From the numerical results using both the truncated Wigner and positive P representations, deviations from the results within the linearisation approximation were found. The cause of this is that the intense control field contains spectral content that overlaps with that of the signal field and hence cannot be easily removed. We also point out that the linearisation approximation breaks down in the regime where optomechanical coupling strength is strong. As experiments are achieving ever stronger optomechanical coupling strength, full analysis of the system without approximations is needed.

# Appendix A

# Monogamy inequalities of quantum entanglement

We have seen how to quantify tripartite quantum entanglement. Can we understand more about the entanglement shared between two of the parties? Consider the example of a discrete tripartite GHZ state $|\psi_1\rangle = \frac{1}{\sqrt{2}}(|000\rangle_{ABC} + |111\rangle_{ABC})$. Are modes $A$ and $B$ entangled? A quick analysis gives negative result. The density operator of the system is $\rho_{ABC} = \frac{1}{2}(|000\rangle\langle 000| + |000\rangle\langle 111| + |111\rangle\langle 000| + |111\rangle\langle 111|)$. Trace out the mode $C$ and we obtain $\rho_{AB} = \frac{1}{2}(|00\rangle\langle 00| + |11\rangle\langle 11|)$, which is a statistical mixture of product states $|00\rangle_{AB}$ and $|11\rangle_{AB}$. The conclusion from the above example is that quantum entanglement cannot be shared between two parties in a tripartite state where entanglement is shared among all three parties. However, a GHZ state is maximally entangled (defined from the fact that the reduced density operator is a diagonal matrix with uniform probability distribution). Is it possible to have bipartite entanglement in a tripartite state with weaker entanglement shared among all three parties?

Let's consider another example with a bipartite entangled state $|\psi_2\rangle = \frac{1}{\sqrt{2}}(|00\rangle_{AB} + |11\rangle_{AB})$ between modes $A$ and $B$. Suppose that a third mode $C$ is allowed to form an entangled state with mode $A$. This implies that mode $C$ is entangled with both modes $A$ and $B$. However, the corresponding density operator after tracing out mode $C$ will not be that of the state $|\psi_2\rangle$, but rather a mixed state. Hence, a mode in a bipartite entangled state $|\psi_2\rangle$ cannot simultaneously form an entangled state with a third party. There is a limit on how quantum entanglement can be shared and distributed. This is important in any quantum information protocols involving quantum entanglement, where, for instance, a third party attempts to gain access to the state of a party in a bipartite entangled system.

Coffman *et al.* [180] tackled the problem of shareability and distribution of quantum entanglement and came up with an inequality that advances the understanding of shareability of entanglement. The Coffman-Kundu-Wootters (CKW) inequality goes as follows:

$$E^{A|(BC)} \geq E^{A|B} + E^{A|C}, \tag{A.1}$$

where $E^{A|(BC)}$ is a measure of entanglement between mode $A$ and modes $BC$, while $E^{A|B}$ and $E^{A|C}$ are measures of entanglement between mode $A$ and $B$, and between mode $A$ and $C$, respectively. These measures are known as concurrences. They are not quantities that are easily measurable in experiments, making them less useful in practice. Also, the inequality in Eq. (A.1) was derived for discrete-variable systems. Recent works by Adesso *et al.* [181], Adesso and Illuminati [182], Adesso *et al.* [183] address these two issues, by using measures that can be experimentally measured and also generalise these measures for continuous-variable systems. These works assume Gaussian states, which include most quantum states that are generated in a continuous-variable quantum optical system.

In the following, we present inequalities to study the shareability of quantum entanglement in the multipartite CV quantum optical system, without assuming Gaussian states. These inequalities are known as monogamy inequalities of entanglement. They constraint the entanglement allowed to be shared with a third party, when bipartite entanglement has already been established between two other parties. They also constraint the entanglement allowed to be shared between two parties in a tripartite entangled state. In particular, these inequalities involve quantities that are routinely measured in laboratories. This section is based on the work by Rosales-Zárate *et al.* [76]. All analytical expressions presented in the following are obtained with Laura Rosales-Zárate and Bogdan Opanchuk.

### A.0.1 Monogamy relation for TDGCZ entanglement certifier

The observables involved in the monogamy inequalities are the quadratures of light modes as described in Section 1.2. As mentioned before, these monogamy relations study the shareability of quantum entanglement in multipartite systems. It is thus natural that these inequalities involve bipartite entanglement certifiers, which are measures to certify the presence of quantum entanglement between two modes $A$ and $B$. In this section, we consider the Tan-Duan-Giedke-Cirac-Zoller (TDGCZ) entangle-

ment certifier defined by Tan [184] and Duan *et al.* [185]:

$$D_{AB} = \frac{1}{4}\left[\Delta^2\left(X_A - X_B\right) + \Delta^2\left(P_A + P_B\right)\right], \tag{A.2}$$

where $\Delta^2\left(X_A - X_B\right)$ and $\Delta^2\left(P_A + P_B\right)$ are the variances of the observables $X_A - X_B$ and $P_A + P_B$, respectively. Entanglement is present if $D_{AB}$ is less than 1. Here, we present the monogamy relation involving TDGCZ entanglement certifiers, leaving the proof in Appendix B.

**Result (1):** For any three modes $A$, $B$ and $C$, the following monogamy relation holds

$$D_{BA} + D_{BC} \geq 1\,. \tag{A.3}$$

The monogamy relation in Eq. (A.3) constraints how entanglement is shared in a tripartite system. For instance, if modes $A$ and $B$ are entangled, indicated by $D_{BA} < 1$, then modes $B$ and $C$ has to satisfy $D_{BC} \geq 1 - D_{BA}$, which places a lower bound on how strongly modes $B$ and $C$ can be entangled. Next, we relate the notion of entanglement monogamy with EPR-steering. By expressing the monogamy relation in terms of EPR-steering certifier, the lower bound established in Eq. (A.3) can be increased, further restricting the amount of bipartite entanglement allowed in a tripartite system.

First, let us define the steering certifier $S_{B|\{AC\}}$, with the subscript $B|\{AC\}$ representing the steering of mode $B$ by modes $A$ and $C$:

$$S_{B|\{AC\}} = \Delta\left[X_B + \left(g_{BA,x}X_A + g_{BC,x}X_C\right)\right]\Delta\left[P_B + \left(g_{BA,p}P_A + g_{BC,p}P_C\right)\right], \tag{A.4}$$

where $g_{BA,x}, g_{BC,x}, g_{BA,p}, g_{BC,p}$ are gains which can be chosen to minimise the steering certifier. Here, the mode $B$ has a quantum description while modes $AC$ are represented by any density operators that are not quantum in nature. With the steering certifier $S_{B|\{AC\}}$, we present the monogamy relation in Result (2).

**Result (2):** The following inequality holds:

$$D_{BA} + D_{BC} \geq \max\left\{1, S_{B|\{AC\}}\right\}. \tag{A.5}$$

We will consider a few examples to demonstrate that $S_{B|\{AC\}}$ can indeed be larger than 1, further restricting the amount of bipartite entanglement that can be shared in a tripartite system.

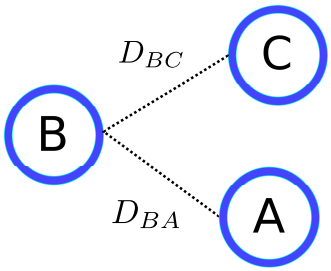


$$D_{BA} + D_{BC} \geq 1$$

Figure A.1: Entanglement relation between mode $B$ and modes $A$ and $C$. The amount of entanglement shared has to satisfy the monogamy relation.

### A.0.2 Monogamy relation for GMVT entanglement certifier

The monogamy relations in Results (1) and (2) have fixed gains. However, we learned in Section 1.4 that entanglement certifiers can be minimised by choosing a set of optimal gain coefficients. It is possible then that with these minimised certifiers, monogamy relations can be violated. The general, optimisable gains are incorporated in the GMVT entanglement certifier which will be defined below. The GMVT entanglement certifier is the generalisation of the DGCZ entanglement certifier and has the form

$$Ent_{AB}(\mathbf{g_{AB}}) = \frac{\Delta(X_A - g_{AB,x}X_B)\Delta(P_A + g_{AB,p}P_B)}{(1 + g_{AB,x}g_{AB,p})}, \tag{A.6}$$

where $\mathbf{g_{AB}} = (g_{AB,x}, g_{AB,p})$, with $g_{AB,x}$ and $g_{AB,p}$ as real numbers that can be optimised to minimise $Ent_{AB}(\mathbf{g_{AB}})$. Entanglement between modes $A$ and $B$ is certified when $Ent_{AB}(\mathbf{g_{AB}})$ is less than 1. The monogamy relation involving the GMVT entanglement certifier is presented in Result (3). Note that in Result (3), the gains for the $x$ and $p$ quadratures are chosen to be identical, i.e. $g_{AB,x} = g_{AB,p} = g_{AB}$. This set of gain coefficients are optimal for EPR type states where the correlations among different modes have the same form in both the $x$ and $p$ quadratures. For any arbitrary states, the set of optimal gain coefficients has to be determined separately.

**Result (3):** The monogamy inequality

$$Ent_{BA}(g_{BA})Ent_{BC}(g_{BC}) \geqslant M_B \tag{A.7}$$

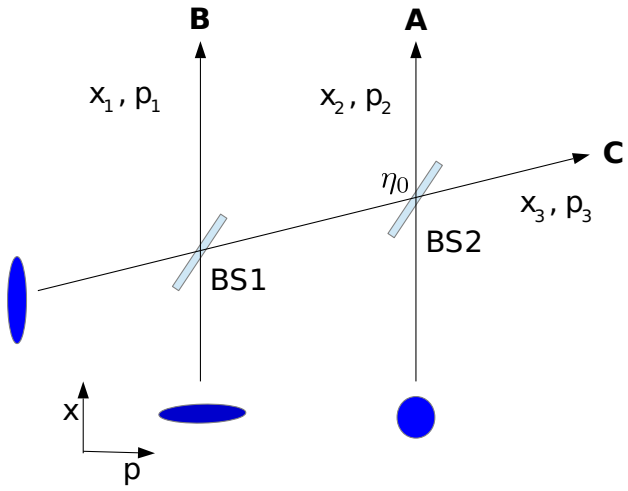


Figure A.2: Experimental setup for the generation of CV tripartite entangled states. The transmittivity of the beam splitter $BS2$ is $\eta_0$.

holds for any real values $g_{BA}$, $g_{BC}$, where

$$M_B = \frac{\max\{1, S^2_{B|\{AC\}}\}}{\left(1+g^2_{BA}\right)\left(1+g^2_{BC}\right)} \tag{A.8}$$

and $S^2_{B|\{AC\}} = \Delta^2\left[X_B + (g_{BA}X_A + g_{BC}X_C)\right]\Delta^2\left[P_B + (g_{BA}P_A + g_{BC}P_C)\right]$.

### A.0.3 Monogamy for CV tripartite entangled states

Here, we apply the monogamy relations of Results (2) and (3) in Eqs. (A.5) and (A.7) to CV GHZ and CV $W$-type states. Instead of labelling the modes $1,2$ and $3$ as in Section 1.2, the modes are labelled as $A,B$ and $C$. Fig. A.2 shows the setup and notations used in this section. This setup generates a CV tripartite $W$-type state; while a CV GHZ state is generated by using a squeezed vacuum state into the second beam splitter BS2. We look at CV GHZ states first, as they are maximally entangled states and should therefore satisfy monogamy relations.

#### A.0.3.1 CV tripartite GHZ states

We evaluate the monogamy relations of Results (1) and (2) for the CV tripartite GHZ state. The covariances are obtained using Eq. (1.13) and the entanglement certifiers can be showed to be $D_{BA} =$

$D_{BC}$ and it is given by

$$D_{BA} = \frac{1}{4}\left(\frac{3}{2}e^{-2r_2} + \frac{1}{2}e^{-2r_3} + \frac{4}{3}e^{-2r_1} + \frac{1}{6}e^{2r_2} + \frac{1}{2}e^{2r_3}\right), \tag{A.9}$$

which diverges as $r_1, r_2, r_3 \to \infty$. Since $D_{BA} > 1$ and $D_{BC} > 1$, monogamy relations are always trivially satisfied. This is consistent with what we expect from the analysis of the example in the beginning of Appendix A, that there is no bipartite entanglement in a GHZ state.

### A.0.3.2 CV tripartite $W$-type states

From our previous analysis, we find that there is no bipartite entanglement in a maximally entangled tripartite state. For these maximally entangled states then, it should be of no surprise that monogamy relations are satisfied. What about states that are not maximally entangled? Do they contain bipartite entanglement such that monogamy relations are violated? To answer this question, we look at CV tripartite W-state, which is "less" entangled than a maximally entangled state. In order to show that, we first consider the discrete tripartite W state, given by

$$|\psi_W\rangle = \frac{1}{\sqrt{3}}\left(|001\rangle + |010\rangle + |100\rangle\right). \tag{A.10}$$

We attempt to find out whether there can be bipartite entanglement for the tripartite W state by tracing out one of the modes, say mode $C$, of the corresponding W state density operator $\rho_W$. This leads to

$$\begin{aligned}\rho_{AB} &= \mathrm{Tr}_C \rho_W \\ &= \frac{1}{3}\left(|00\rangle\langle 00| + |01\rangle\langle 01| + |01\rangle\langle 10| + |10\rangle\langle 01| + |10\rangle\langle 10|\right),\end{aligned} \tag{A.11}$$

which is a statistical mixture of bipartite entangled state $\frac{1}{\sqrt{2}}\left(|01\rangle + |10\rangle\right)$ with probability $\frac{2}{3}$ and a vacuum state $|00\rangle$ with probability $\frac{1}{3}$. This simple analysis shows that bipartite entanglement can be observed in a W state. It is possible then to have $D_{BA} < 1$ and $D_{BC} < 1$ while violating monogamy relations. Explicit calculations are needed to check for this possibility.

In order to evaluate the monogamy inequalities, the covariances are computed for both the CV

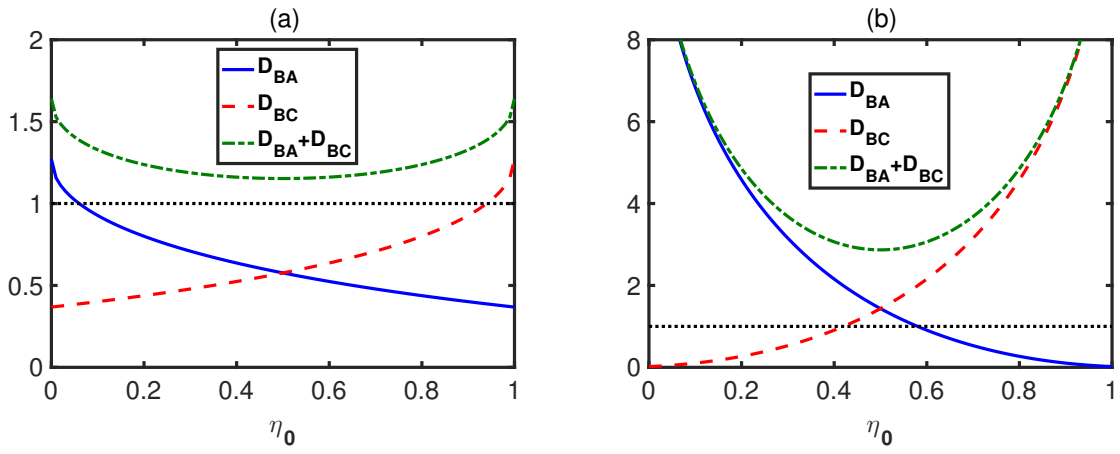


Figure A.3: Checking the monogamy relation for the CV $W$-type states. The $D_{BA}$, $D_{BC}$ and $D_{BA}+D_{BC}$ versus $\eta_0$ . Here $r = 0.5$ (a) and $r = 2$ (b). The monogamy bound of 1 is indicated by the gray dotted line.

tripartite $W$-type and CV GHZ states. They are denoted by $n_{IJ} = \langle X_I, X_I \rangle$, $m_{IJ} = \langle X_J, X_J \rangle$ and $c_{IJ} = \langle X_I, X_J \rangle$. These covariances are evaluated for general transmittivity $\eta_0$ for the beam splitter $BS2$ and also the squeezing parameter $r$, which characterises the degree of squeezing of the input states. For the CV tripartite $W$-type state, the covariances for this case are $n_{BA} = \cosh 2r$, $m_{BA} = \eta_0 \cosh 2r + (1-\eta_0)$ and $c_{BA} = \sqrt{\eta_0} \sinh 2r$. Those for modes $B$ and $C$ are obtained by replacing $\eta_0$ with $1-\eta_0$. For this case, $D_{BA}$ reduces to

$$D_{BA} = \left( \eta_0 \cosh 2r + (1-\eta_0) + \cosh 2r - 2\sqrt{\eta_0} \sinh 2r \right)/2 . \tag{A.12}$$

The expression for $D_{BC}$ is found by replacing $\eta_0$ with $1-\eta_0$.

We plot the quantities $D_{BA}$, $D_{BC}$ and $D_{BA}+D_{BC}$ as a function of the transmittivity $\eta_0$ of BS2 for the squeezing parameter $r = 0.5$ and $r = 2.0$, in Fig. A.3(a) and Fig. A.3(b) respectively. From these figures, we see that the monogamy relation of Result (1) always holds. In other words, bipartite entanglement of arbitrary strength cannot exist in a tripartite entangled state. In Fig. A.3(a) which corresponds to a state with squeezing parameter $r = 0.5$, we see that it is possible to have bipartite entanglement between modes $BA$ and modes $BC$. However, this is not the case for $r = 2.0$ as shown in Fig. A.3(b). For this squeezing parameter, it seems that if we observe bipartite entanglement in two of the modes, say $BA$, then there cannot be bipartite entanglement between modes $BC$. We check for the validity of this observation using the more general GMVT entanglement certifiers with variable gain

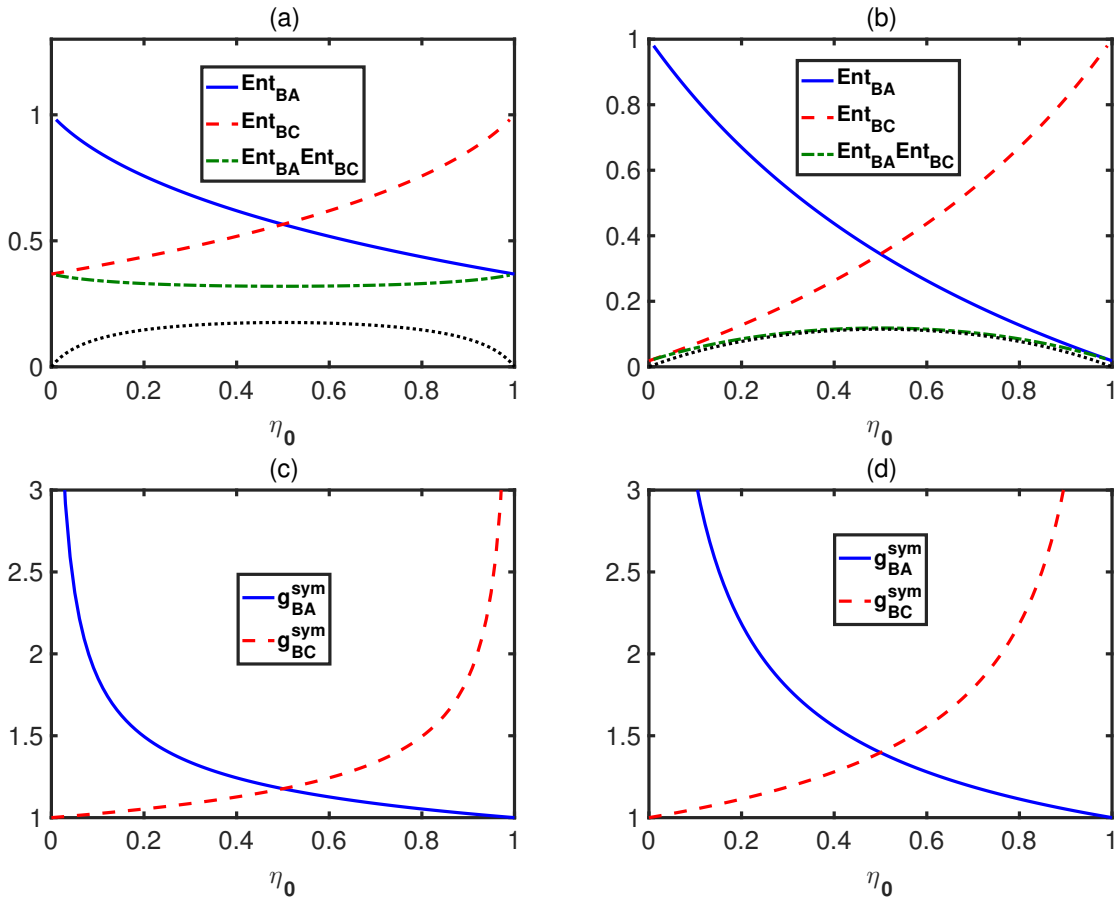


Figure A.4: Checking the monogamy relation for the CV $W$-type states. The $Ent_{BA}$, $Ent_{BC}$, $Ent_{BA}Ent_{BC}$ and the monogamy bound $M_B$ (gray dotted line) are plotted versus $\eta_0$. The symmetry parameters $g_{BA}^{(sym)}, g_{BC}^{(sym}$ are plotted in Figs. (c) and (d). Here $r = 0.5$ (a,c) and $r = 2$ (b,d).

coefficients.

In order to compute the monogamy relation of Result (2), we evaluate the steering parameter $S_{B|F}$ for the CV tripartite $W$-type states and it is given by

$$S_{B|F} = \left(n_{BF} - c_{BF}^2/m_{BF}\right), \tag{A.13}$$

where $g_x = c_{BF}/m_{BF}$, $g_p = c_{BF}/m_{BF}$.

In Fig. A.4(a) and Fig. A.4(b), we plot the quantities $Ent_{BA}$, $Ent_{BC}$ and $Ent_{BA}Ent_{BC}$ as a function of the transmittivity $\eta_0$ of BS2, for the squeezing parameter $r = 0.5$ and $r = 2.0$ respectively. We see that it is possible to have bipartite entanglement between modes $BA$ and modes $BC$ where both $D_{BA} < 1$ and $D_{BC} < 1$. However, we also see that the monogamy relation of Result (2) always holds for CV tripartite $W$-type states. This suggests that monogamy entanglement is an intrinsic property of a system with multipartite entanglement. It dictates the shareability of entanglement in multipartite systems, putting constraints on entanglement among parties that is fewer than the total number of parties.

# Appendix B

# Monogamy relation: Result (1)

We prove two lemmas that will be used in the proof of Result (1) in Appendix A.

**Lemma 1**: $\Delta^2(X_B - X_A) \geq \Delta^2(X_B|X_A)$, where $\Delta^2(X_B|X_A)$ is the average variance of $X_B$ over all possible measurement outcomes of $X_A$.

**Proof**:

$$\begin{aligned}
\Delta^2(X_B - X_A) &= \sum_{x_A, x_B} P(x_A, x_B)\,(x_B - x_A - \langle X_B - X_A\rangle)^2 \\
&= \sum_{x_A, x_B} P(x_A, x_B)\,(x_B - x_A - \langle X_B\rangle - \langle X_A\rangle)^2 \\
&\equiv \sum_{x_A} P(x_A) \sum_{x_B} P(x_B|x_A)\,(x_B - f(x_A))^2 \\
&\geq \sum_{x_A} P(x_A) \sum_{x_B} P(x_B|x_A)\,\left(x_B - \mu_{B|x_A}\right)^2 \\
&\equiv \Delta^2(X_B|X_A)\,.
\end{aligned}$$

The second lemma is related to the EPR-Reid criterion, first derived by Reid [17] to demonstrate the EPR paradox. It has been shown to be an EPR-steering criterion by Cavalcanti *et al.* [19]. The EPR-Reid criterion is given by $\Delta(X_B - X_A)\,\Delta(P_B - P_A) \geq 1$. From Lemma 1, we obtain the inequality $\Delta(X_B|X_A)\,\Delta(P_B|P_A) \geq 1$.

**Lemma 2**: $\Delta(X_B|X_A)\,\Delta(P_B|P_A) \geq 1$ implies $\Delta^2(X_B|X_A) + \Delta^2(P_B|P_A) \geq 2$.

**Proof**: The proof follows from the inequality $x^2 + y^2 \geq 2xy$. It is straightforward to show that

$$\begin{aligned}\Delta^2(X_B|X_A) + \Delta^2(P_B|P_A) &\geq 2\Delta(X_B|X_A)\,\Delta(P_B|P_A) \\ &\geq 2\,.\end{aligned}$$

With Lemmas (1) and (2), we proof Result (1):

$$D_{BA} + D_{BC} \geq 1\,.$$

Proof:

$$\begin{aligned}D_{BA} + D_{BC} &\geq \frac{1}{4}\left[\Delta^2(X_B - X_A) + \Delta^2(P_B - P_A) + \Delta^2(X_B - X_C) + \Delta^2(P_B - P_C)\right] \\ &\geq \frac{1}{4}\left[\Delta^2(X_B|X_A) + \Delta^2(P_B|P_A) + \Delta^2(X_B|X_A) + \Delta^2(P_C|P_C)\right] \\ &\geq 1\,.\end{aligned}$$

# Appendix C

# Steering inequalities including losses

The detected fields $a_{det}$, $b_{det}$ and the undetected fields $a_{loss}$, $b_{loss}$ due to losses are given by

$$\begin{aligned} a_{det} &= \sqrt{\eta_a}a + \sqrt{1-\eta_a}a_v \\ a_{loss} &= -\sqrt{1-\eta_a}a + \sqrt{\eta_a}a_v \\ b_{det} &= \sqrt{\eta_b}b + \sqrt{1-\eta_b}b_v \\ b_{loss} &= -\sqrt{1-\eta_b}b + \sqrt{\eta_b}b_v\,, \end{aligned} \tag{C.1}$$

where $a_v$ and $b_v$ are vacuum states. Using these mode operators, we express $a$, $b$ in terms of $a^\dagger_{det}$, $a^\dagger_{loss}$, $b^\dagger_{det}$ and $b^\dagger_{loss}$. The density operator for a NOON state, $\rho = |\psi\rangle\langle\psi|$, can then be expressed in terms of these operators. Since we are not interested in the modes $a_{loss}$ and $b_{loss}$ (which we label $A, loss$ and $B, loss$) we take the trace over the states of the loss mode to evaluate $\rho' \equiv Tr_{A,loss;B,loss}\rho$. After using the binomial expansion for terms such as $\left(\sqrt{\eta_a}a^\dagger_{det} - \sqrt{(1-\eta_a)}a^\dagger_{loss}\right)$ and performing the trace, the reduced density operator for the detected modes is:

$$\begin{aligned} \rho' = \frac{1}{2}\Bigg[ &\sum_s \binom{N}{N-s} (\eta_a)^{N-s}(1-\eta_a)^s \,|N-s\rangle_{A,det}\langle N-s| \otimes |0\rangle_{B,det}\langle 0| + (\sqrt{\eta_a\eta_b})^N e^{-i\phi}\,|N\rangle_{A,det}\langle 0| \otimes |0\rangle_{B,det}\langle N| \\ &+ (\sqrt{\eta_a\eta_b})^N e^{i\phi}\,|0\rangle_{A,det}\langle N| \otimes |N\rangle_{B,det}\langle 0| + \sum_s \binom{N}{N-s} (\eta_b)^{N-s}(1-\eta_b)^s \,|0\rangle_{A,det}\langle 0| \otimes |N-s\rangle_{B,det}\langle N-s| \Bigg] \end{aligned} \tag{C.2}$$

## C.1 Calculating $\Delta^2_{inf}(P_b^N)$ and $\Delta^2_{inf}(X_b^N)$

As described in Section 2.1, the $\Delta^2_{inf}(P_b^N)$ and $\Delta^2_{inf}(X_b^N)$ are the inferred variances of quantities $P_b^N$ and $X_b^N$ due to a measurement in $X_a$. We evaluate these inferred variances using the density operator for modes $a_{det}$ and $b_{det}$ given in Eq. (C.2). For the inferred variances we evaluate the density operator $\rho''$, where we consider that the mode $A,det$ is in the state $|x\rangle$. This density operator is given by:

$$\begin{aligned}
\rho'' &= \frac{|x\rangle_{A,det}\langle x|\rho'|x\rangle_{A,det}\langle x|}{P(x)} \\
&= \frac{1}{2P(x)}\left[\sum_s \binom{N}{N-s} (\eta_a)^{N-s}(1-\eta_a)^s \langle x|N-s\rangle_{Ad}\langle N-s|x\rangle|x\rangle_{Ad}\langle x| \otimes |0\rangle_{Bd}\langle 0|\right. \\
&+ (\sqrt{\eta_a\eta_b})^N e^{-i\phi}\langle x|N\rangle_{Ad}\langle 0|x\rangle|x\rangle_{Ad}\langle x| \otimes |0\rangle_{Bd}\langle N| + (\sqrt{\eta_a\eta_b})^N e^{i\phi}\langle x|0\rangle_{Ad}\langle N|x\rangle|x\rangle_{Ad}\langle x| \otimes |N\rangle_{Bd}\langle 0| \\
&\left. + \sum_s \binom{N}{N-s} (\eta_b)^{N-s}(1-\eta_b)^s \langle x|0\rangle_{Ad}\langle 0|x\rangle|x\rangle_{Ad}\langle x| \otimes |N-s\rangle_{Bd}\langle N-s|\right]
\end{aligned} \tag{C.3}$$

where

$$\begin{aligned}
P(x) &= Tr\left[|x\rangle_{A,det}\langle x|\rho'|x\rangle_{A,det}\langle x|\right] \\
&= \frac{1}{2}\left[\sum_s \binom{N}{N-s} (\eta_a)^{N-s}(1-\eta_a)^s |\langle x|N-s\rangle|^2 + \sum_s \binom{N}{N-s} (\eta_b)^{N-s}(1-\eta_b)^s |\langle x|0\rangle|^2\right]
\end{aligned} \tag{C.4}$$

For clarity of the expressions, we denote the detected modes by $Ad \equiv A,det$ and $Bd \equiv B,det$ in the following. In order to compute $\Delta^2(P_b^N|x)$ and $\Delta^2(X_b^N|x)$, we trace out the $A,det$ mode to get the reduced density operator for $B,det$ mode:

$$\begin{aligned}
\rho_{red,det,x} &= Tr_{A,det}\left(\rho''\right) \\
&= \frac{1}{2P(x)}\left[\sum_s \binom{N}{N-s} (\eta_a)^{N-s}(1-\eta_a)^s \langle x|N-s\rangle_{Ad}\langle N-s|x\rangle|0\rangle_{Bd}\langle 0|\right. \\
&+ (\sqrt{\eta_a\eta_b})^N e^{-i\phi}\langle x|N\rangle_{Ad}\langle 0|x\rangle|0\rangle_{Bd}\langle N| + (\sqrt{\eta_a\eta_b})^N e^{i\phi}\langle x|0\rangle_{Ad}\langle N|x\rangle|N\rangle_{Bd}\langle 0| \\
&\left. + \sum_s \binom{N}{N-s} (\eta_b)^{N-s}(1-\eta_b)^s \langle x|0\rangle_{Ad}\langle 0|x\rangle|N-s\rangle_{Bd}\langle N-s|\right]
\end{aligned} \tag{C.5}$$

The inferred variances are defined as:

$$\begin{aligned}\Delta^2(X_b^N|x) &= \langle \left(X_b^N\right)^2|x\rangle - \langle X_b^N|x\rangle^2 \\ \Delta^2(P_b^N|x) &= \langle \left(P_b^N\right)^2|x\rangle - \langle P_b^N|x\rangle^2\end{aligned} \tag{C.6}$$

Next we evaluate $\langle X_b^n|x\rangle = Tr\left[\rho_{red,det,x}X_b^n\right]$ and $\langle P_b^n|x\rangle = Tr\left[\rho_{red,det,x}P_b^n\right]$ using the density operator given in Eq. (C.5) obtaining:

$$\begin{aligned}\langle X_b^n|x\rangle = \frac{1}{2P(x)}\Bigg[&\sum_s \binom{N}{N-s}(\eta_a)^{N-s}(1-\eta_a)^s \langle x|N-s\rangle_{Ad}\langle N-s|x\rangle \int x_B^n\langle 0|x_B\rangle\langle x_B|0\rangle\, dx_B \\ &+ (\sqrt{\eta_a\eta_b})^N e^{-i\phi}\langle x|N\rangle_{Ad}\langle 0|x\rangle \int x_B^n\langle N|x_B\rangle\langle x_B|0\rangle dx_B + (\sqrt{\eta_a\eta_b})^N e^{i\phi}\langle x|0\rangle_{Ad}\langle N|x\rangle \int x_B^n\langle 0|x_B\rangle\langle x_B|N\rangle dx_B \\ &+ \sum_s \binom{N}{N-s}(\eta_b)^{N-s}(1-\eta_b)^s \langle x|0\rangle_{Ad}\langle 0|x\rangle \int x_B^n\langle N-s|x_B\rangle\langle x_B|N-s\rangle\, dx_B\Bigg]\end{aligned} \tag{C.7}$$

$$\begin{aligned}\langle P^n|x\rangle = \frac{1}{2P(x)}\Bigg[&\sum_s \binom{N}{N-s}(\eta_a)^{N-s}(1-\eta_a)^s \langle x|N-s\rangle_{A,det}\langle N-s|x\rangle \int p_B^n\langle 0|p_B\rangle\langle p_B|0\rangle\, dp_B \\ &+ (\sqrt{\eta_a\eta_b})^N e^{-i\phi}\langle x|N\rangle_{Ad}\langle 0|x\rangle \int p_B^n\langle N|p_B\rangle\langle p_B|0\rangle dp_B + (\sqrt{\eta_a\eta_b})^N e^{i\phi}\langle x|0\rangle_{Ad}\langle N|x\rangle \int p_B^n\langle 0|p_B\rangle\langle p_B|N\rangle\, dp_B \\ &+ \sum_s \binom{N}{N-s}(\eta_b)^{N-s}(1-\eta_b)^s \langle x|0\rangle_{A,det}\langle 0|x\rangle \int p_B^n\langle N-s|p_B\rangle\langle p_B|N-s\rangle\, dp_B\Bigg]\end{aligned} \tag{C.8}$$

The value of the corresponding variances for $\Delta^2(X_b^N|x)$ and $\Delta^2(P_b^N|x)$ of equations (C.6) is evaluated using the expressions given in equations (C.7) and (C.8) considering $n = N$ or $n = 2N$.

## C.2 Inferred variances $\Delta^2_{inf}(n_b)$ including losses

$\Delta^2_{inf}(n_b)$ is the inferred variance of $n_b$ due to a measurement in $n_a$. In order to evaluate this variance we will consider that the outcome in $n_a$ is $m$. We define $P(m)$ as the probability for obtaining the result $m$ for $n_a$. Next, we evaluate the reduced density operator $\rho_m$ for the modes $A, det$ and $B, det$ given that the

outcome is $m$:

$$\begin{aligned}\rho_m &= \frac{1}{P(m)}\left[|m\rangle_{Ad}\langle m|\rho'|m\rangle_{Ad}\langle m|\right] \\ &= \frac{1}{2P(m)}\left[\binom{N}{m}\eta_a^m(1-\eta_a)^{N-m}|m\rangle_{Ad}\langle m|\otimes|0\rangle_{Bd}\langle 0|+\sum_s\binom{N}{N-s}\eta_b^{N-s}(1-\eta_b)^s|0\rangle_{Ad}\langle 0|\otimes|N-s\rangle_{Bd}\langle N-s|\right]\end{aligned} \tag{C.9}$$

where

$$P(m) = Tr\left[|m\rangle_{A,det}\langle m|\rho'|m\rangle_{A,det}\langle m|\right] = \frac{1}{2}\binom{N}{m}\eta_a^m(1-\eta_a)^{N-m}+\frac{1}{2}. \tag{C.10}$$

Next we evaluate $\langle n_B\rangle_{inf,m} = Tr\left[\rho_m n_B\right]$ and $\langle n_B^2\rangle_{inf,m} = Tr\left[\rho_m n_B^2\right]$ obtaining:

$$\langle n_B\rangle_{inf,m} = \frac{1}{2}\frac{\sum_s\binom{N}{N-s}\eta_b(1-\eta_b)^s\delta_{m,0}(N-s)}{P(n_A=m)}$$

$$\langle n_B^2\rangle_{inf,m} = \frac{1}{2}\frac{\sum_s\binom{N}{N-s}\eta_b(1-\eta_b)^s\delta_{m,0}(N-s)^2}{P(n_A=m)}. \tag{C.11}$$

Since $n_A = m = 0$ is the only non-zero contribution for the statistical moments we obtain:

$$\begin{aligned}\langle n_B\rangle_{inf,0} &= \frac{1}{2}\frac{N\eta_b}{P(n_A=0)} \\ \langle n_B^2\rangle_{inf,0} &= \frac{1}{2}\frac{\eta_b\left(N-N\eta_b+N^2\eta_b\right)}{P(n_A=0)} \\ P(n_A=0) &= \frac{1}{2}\left((1-\eta_a)^N+1\right).\end{aligned} \tag{C.12}$$

Using the above results we evaluate the inferred variance for $m=0$, which we denote by $\Delta_{inf}^2 n_{b,0}$:

$$\Delta_{inf}^2 n_{b,0} = \frac{\eta_b(N-N\eta_b)+N\eta_b(1-\eta_a)^N(1-\eta_b+N\eta_b)}{\left((1-\eta_a)^N+1\right)^2} \tag{C.13}$$

The variance of the inferred value $n_B$ is then obtained by summing over all possible values of $m$:

$$\begin{aligned}\Delta^2 n_{inf} &= \sum_m^N P\left(n_A = 0\right) \Delta^2 n_{inf,m=0} \\ &= \frac{\eta_b \left(N - N\eta_b\right) + N\left(1-\eta_a\right)^N \left(\eta_b - \eta_b^2 + N\eta_b^2\right)}{2\left(\left(1-\eta_a\right)^N + 1\right)}.\end{aligned} \tag{C.14}$$

## C.3 Evaluation of $\left|\left\langle\left[n_b, X_b^N\right]\right\rangle\right|_{inf}$ and $\left|\left\langle\left[n_b, P_b^N\right]\right\rangle\right|_{inf}$

Full evaluation of the terms $\left|\left\langle\left[n_b, X_b^N\right]\right\rangle\right|_{inf}$ and $\left|\left\langle\left[n_b, P_b^N\right]\right\rangle\right|_{inf}$ reveals that for the lossy system and for $N \leq 5$:

$$\begin{aligned}\left|\left\langle\left[n_b, X_b^N\right]\right\rangle\right|_{inf} &= N\left|-\left\langle b^N\right\rangle + \left\langle b^{\dagger N}\right\rangle\right|_{inf} \\ \left|\left\langle\left[n_b, P_b^N\right]\right\rangle\right|_{inf} &= N\left|\left\langle b^N\right\rangle + (-1)^{N+1}\left\langle b^{\dagger N}\right\rangle\right|_{inf}\end{aligned} \tag{C.15}$$

We evaluate $\left\langle b^N\right\rangle = Tr\left[\rho_{red,det,x} b^N\right]$ and $\left\langle b^{\dagger N}\right\rangle = Tr\left[\rho_{red,det,x}\left(b^\dagger\right)^N\right]$ using the reduced density matrix given in Eq. (C.5) and perform the corresponding trace. The expression is:

$$\left\langle b^N\right\rangle_{inf,x} = \frac{1}{2P\left(x\right)}\left(\sqrt{\eta_a \eta_b}\right)^N e^{i\phi}\left\langle x|N\right\rangle\left\langle 0|x\right\rangle\sqrt{N!} \tag{C.16}$$

and $\left\langle\left(b^\dagger\right)^N\right\rangle_{inf,x} = \left(\left\langle b^N\right\rangle_{inf,x}\right)^*$.

# Appendix D

# Linearised optomechanical Hamiltonian in the interaction picture

In the following, we transform the linearised optomechanical Hamiltonian (3.21) into a Hamiltonian in the interaction picture. The corresponding dynamics from this interaction picture Hamiltonian $H_{int}$ arises solely from the interaction between the optical and mechanical modes.

$$
\begin{aligned}
H_{int} &= e^{\frac{i}{\hbar}H_0 t} H_1 e^{-\frac{i}{\hbar}H_0 t} \\
&= \hbar e^{i\left(\Delta\delta a^\dagger \delta a + \omega_m \delta b^\dagger \delta b\right)t} \left(g^* \delta a \delta b + g^* \delta a \delta b^\dagger + g\delta a^\dagger \delta b + g\delta a^\dagger \delta b^\dagger\right) e^{-i\left(\Delta\delta a^\dagger \delta a + \omega_m \delta b^\dagger \delta b\right)t} \\
&= \hbar \left\{ \left(g^* \delta a \delta b + g^* \delta a \delta b^\dagger + g\delta a^\dagger \delta b + g\delta a^\dagger \delta b^\dagger\right) + it\left[\Delta\delta a^\dagger \delta a + \omega_m \delta b^\dagger \delta b, g^* \delta a \delta b\right] \right. \\
&\quad + it\left[\Delta\delta a^\dagger \delta a + \omega_m \delta b^\dagger \delta b, g^* \delta a \delta b^\dagger\right] + it\left[\Delta\delta a^\dagger \delta a + \omega_m \delta b^\dagger \delta b, -g\delta a^\dagger \delta b\right] + \\
&\quad \left. it\left[\Delta\delta a^\dagger \delta a + \omega_m \delta b^\dagger \delta b, -g\delta a^\dagger \delta b^\dagger\right] + H.O.T \right\} \\
&= \hbar \left\{ \left(g^* \delta a \delta b + g^* \delta a \delta b^\dagger - g\delta a^\dagger \delta b - g\delta a^\dagger \delta b^\dagger\right) + it\left(-\Delta g^* \delta a \delta b - \omega_m g^* \delta a \delta b\right) \right. \\
&\quad \left. + it\left(-\Delta g^* \delta a \delta b^\dagger + \omega_m g^* \delta a \delta b^\dagger\right) + it\left(\Delta g \delta a^\dagger \delta b - \omega_m g \delta a^\dagger \delta b\right) \right. \\
&= \hbar g^* \delta a \delta b \left[1 + i(\Delta + \omega_m)t + ...\right] + \hbar g^* \delta a \delta b^\dagger \left[1 + i(\Delta - \omega_m)t + ...\right] \\
&\quad + \hbar g \delta a^\dagger \delta b \left[1 - i(\Delta - \omega_m)t + ...\right] + \hbar g \delta a^\dagger \delta b^\dagger \left[1 - i(\Delta + \omega_m)t + ...\right] \\
H_{int} &= \hbar \left[e^{i(\Delta+\omega_m)t} g^* \delta a \delta b + e^{i(\Delta-\omega_m)t} g^* \delta a \delta b^\dagger + e^{-i(\Delta-\omega_m)t} g\delta a^\dagger \delta b + e^{-i(\Delta+\omega_m)t} g\delta a^\dagger \delta b^\dagger\right],
\end{aligned}
$$

where the Baker-Hausdorf lemma is used:

$$
e^{i\lambda\hat{\delta a}} \hat{\delta b} e^{-i\lambda\hat{\delta a}} = \hat{\delta b} + i\lambda\left[\hat{\delta a}, \hat{\delta b}\right] + \frac{(i\lambda)^2}{2!}\left[\hat{\delta a}, \left[\hat{\delta a}, \hat{\delta b}\right]\right] + .... \tag{D.1}
$$

# Appendix E

# Fidelity expression in the Wigner representation

The Wigner representation of a density operator is given by

$$\rho = \int W(\alpha)\,\Lambda(\alpha)\,d^2\alpha\,, \tag{E.1}$$

where $W(\alpha)$ is the Wigner function and $\Lambda(\alpha)$ is a projector operator. For instance, in the Glauber P representation, the projection operator is $|\alpha\rangle\langle\alpha|$. In the computation of the fidelity, the exact form of $\Lambda(\alpha)$ is not required, as we will show below.

Using the expression of a density operator in the Wigner representation as in Eq. (E.1), the fidelity defined in Eq. (4.28) is

$$\begin{aligned} F &= \mathrm{Tr}\,(\rho_i\rho_f) \\ &= \int\int W_i(\alpha)\,W_f(\beta)\,\mathrm{Tr}\,[\Lambda(\alpha)\,\Lambda(\beta)]\,d^2\alpha d^2\beta \\ &= \pi\int W_i(\alpha)\,W_f(\alpha)\,d^2\alpha\,, \end{aligned} \tag{E.2}$$

where $\mathrm{Tr}[\Lambda(\alpha)\,\Lambda(\beta)]$=$\pi\delta(\alpha-\beta)$ [163].

# Bibliography


[1] P. van Loock and A. Furusawa, Phys. Rev. A **67**, 052315 (2003).

[2] M. Giustina, M. A. M. Versteegh, S. Wengerowsky, J. Handsteiner, A. Hochrainer, K. Phelan, F. Steinlechner, J. Kofler, J.-A. Larsson, C. Abellán, W. Amaya, V. Pruneri, M. W. Mitchell, J. Beyer, T. Gerrits, A. E. Lita, L. K. Shalm, S. W. Nam, T. Scheidl, R. Ursin, B. Wittmann, and A. Zeilinger, Phys. Rev. Lett. **115**, 250401 (2015).

[3] L. K. Shalm, E. Meyer-Scott, B. G. Christensen, P. Bierhorst, M. A. Wayne, M. J. Stevens, T. Gerrits, S. Glancy, D. R. Hamel, M. S. Allman, K. J. Coakley, S. D. Dyer, C. Hodge, A. E. Lita, V. B. Verma, C. Lambrocco, E. Tortorici, A. L. Migdall, Y. Zhang, D. R. Kumor, W. H. Farr, F. Marsili, M. D. Shaw, J. A. Stern, C. Abellán, W. Amaya, V. Pruneri, T. Jennewein, M. W. Mitchell, P. G. Kwiat, J. C. Bienfang, R. P. Mirin, E. Knill, and S. W. Nam, Phys. Rev. Lett. **115**, 250402 (2015).

[4] B. Hensen, H. Bernien, A. E. Dreau, A. Reiserer, N. Kalb, M. S. Blok, J. Ruitenberg, R. F. L. Vermeulen, R. N. Schouten, C. Abellan, W. Amaya, V. Pruneri, M. W. Mitchell, M. Markham, D. J. Twitchen, D. Elkouss, S. Wehner, T. H. Taminiau, and R. Hanson, Nature **526**, 682 (2015).

[5] A. Einstein, B. Podolsky, and N. Rosen, Phys. Rev. **47**, 777 (1935).

[6] J. Yin, Y. Cao, Y.-H. Li, S.-K. Liao, L. Zhang, J.-G. Ren, W.-Q. Cai, W.-Y. Liu, B. Li, H. Dai, G.-B. Li, Q.-M. Lu, Y.-H. Gong, Y. Xu, S.-L. Li, F.-Z. Li, Y.-Y. Yin, Z.-Q. Jiang, M. Li, J.-J. Jia, G. Ren, D. He, Y.-L. Zhou, X.-X. Zhang, N. Wang, X. Chang, Z.-C. Zhu, N.-L. Liu, Y.-A. Chen, C.-Y. Lu, R. Shu, C.-Z. Peng, J.-Y. Wang, and J.-W. Pan, Science **356**, 1140 (2017).

[7] V. Scarani, arXiv preprint arXiv:0910.4222 (2009).

[8] V. Scarani, Acta Phys. Slov. **62** (2012).

[9] N. Brunner, D. Cavalcanti, S. Pironio, V. Scarani, and S. Wehner, Rev. Mod. Phys. **86**, 419 (2014).

[10] J. S. Bell, Physics **1**, 195 (1964).

[11] J. F. Clauser, M. A. Horne, A. Shimony, and R. A. Holt, Phys. Rev. Lett. **23**, 880 (1969).

[12] E. Schrödinger, Naturwissenschaften **23**, 807 (1935).

[13] R. F. Werner, Phys. Rev. A **40**, 4277 (1989).

[14] A. Peres, Phys. Rev. Lett. **77**, 1413 (1996).

[15] M. Horodecki, P. Horodecki, and R. Horodecki, Physics Letters A **223**, 1 (1996).

[16] E. Schrodinger, Mathematical Proceedings of the Cambridge Philosophical Society **31**, 555 (1935).

[17] M. D. Reid, Phys. Rev. A **40**, 913 (1989).

[18] H. M. Wiseman, S. J. Jones, and A. C. Doherty, Phys. Rev. Lett. **98**, 140402 (2007).

[19] E. G. Cavalcanti, S. J. Jones, H. M. Wiseman, and M. D. Reid, Phys. Rev. A **80**, 032112 (2009).

[20] C. Branciard, E. G. Cavalcanti, S. P. Walborn, V. Scarani, and H. M. Wiseman, Phys. Rev. A **85**, 010301 (2012).

[21] C. H. Bennett and G. Brassard, in *International Conference on Computers, Systems & Signal Processing, Bangalore, India, Dec 9-12, 1984* (1984) pp. 175–179.

[22] D. Deutsch, A. Ekert, R. Jozsa, C. Macchiavello, S. Popescu, and A. Sanpera, Phys. Rev. Lett. **77**, 2818 (1996).

[23] R. B. Griffiths and C.-S. Niu, Phys. Rev. A **56**, 1173 (1997).

[24] H.-K. Lo and H. F. Chau, Science **283**, 2050 (1999).

[25] D. Mayers, J. ACM **48**, 351 (2001).

[26] C. H. Bennett, G. Brassard, C. Crépeau, R. Jozsa, A. Peres, and W. K. Wootters, Phys. Rev. Lett. **70**, 1895 (1993).

[27] S. L. Braunstein and H. J. Kimble, Phys. Rev. Lett. **80**, 869 (1998).

[28] S. L. Braunstein, C. A. Fuchs, and H. J. Kimble, Journal of Modern Optics **47**, 267 (2000).

[29] B. Opanchuk, L. Arnaud, and M. D. Reid, Phys. Rev. A **89**, 062101 (2014).

[30] A. Acín, D. Cavalcanti, E. Passaro, S. Pironio, and P. Skrzypczyk, Phys. Rev. A **93**, 012319 (2016).

[31] A. Máttar and A. Acín, Physica Scripta **91**, 043003 (2016).

[32] F. Fröwis, P. Sekatski, W. Dür, N. Gisin, and N. Sangouard, arXiv preprint arXiv:1706.06173 (2017).

[33] A. O. Caldeira and A. J. Leggett, Phys. Rev. A **31**, 1059 (1985).

[34] D. F. Walls and G. J. Milburn, Phys. Rev. A **31**, 2403 (1985).

[35] W. Zurek, Physics Today **44**, 36 (1991).

[36] M. Brune, E. Hagley, J. Dreyer, X. Maître, A. Maali, C. Wunderlich, J. M. Raimond, and S. Haroche, Phys. Rev. Lett. **77**, 4887 (1996).

[37] C. Monroe, D. M. Meekhof, B. E. King, and D. J. Wineland, Science **272**, 1131 (1996).

[38] J. R. Friedman, V. Patel, W. Chen, S. K. Tolpygo, and J. E. Lukens, Nature **406**, 43 (2000).

[39] D. Leibfried, E. Knill, S. Seidelin, J. Britton, R. B. Blakestad, J. Chiaverini, D. B. Hume, W. M. Itano, J. D. Jost, C. Langer, R. Ozeri, R. Reichle, and D. J. Wineland, Nature **438**, 639 (2005).

[40] A. Ourjoumtsev, R. Tualle-Brouri, J. Laurat, and P. Grangier, Science **312**, 83 (2006).

[41] A. Ourjoumtsev, H. Jeong, R. Tualle-Brouri, and P. Grangier, Nature **448**, 784 (2007).

[42] H. Takahashi, K. Wakui, S. Suzuki, M. Takeoka, K. Hayasaka, A. Furusawa, and M. Sasaki, Phys. Rev. Lett. **101**, 233605 (2008).

[43] R. Dong, A. Tipsmark, A. Laghaout, L. A. Krivitsky, M. Ježek, and U. L. Andersen, J. Opt. Soc. Am. B **31**, 1192 (2014).

[44] J. Etesse, M. Bouillard, B. Kanseri, and R. Tualle-Brouri, Phys. Rev. Lett. **114**, 193602 (2015).

[45] C. Wang, Y. Y. Gao, P. Reinhold, R. W. Heeres, N. Ofek, K. Chou, C. Axline, M. Reagor, J. Blumoff, K. M. Sliwa, L. Frunzio, S. M. Girvin, L. Jiang, M. Mirrahimi, M. H. Devoret, and R. J. Schoelkopf, Science **352**, 1087 (2016).

[46] B. Yurke and D. Stoler, Phys. Rev. Lett. **57**, 13 (1986).

[47] L. Krippner, W. J. Munro, and M. D. Reid, Phys. Rev. A **50**, 4330 (1994).

[48] T. Monz, P. Schindler, J. T. Barreiro, M. Chwalla, D. Nigg, W. A. Coish, M. Harlander, W. Hänsel, M. Hennrich, and R. Blatt, Phys. Rev. Lett. **106**, 130506 (2011).

[49] A. D. O'Connell, M. Hofheinz, M. Ansmann, R. C. Bialczak, M. Lenander, E. Lucero, M. Neeley, D. Sank, H. Wang, M. Weides, *et al.*, Nature **464**, 697 (2010).

[50] J. Chan, T. M. Alegre, A. H. Safavi-Naeini, J. T. Hill, A. Krause, S. Gröblacher, M. Aspelmeyer, and O. Painter, Nature **478**, 89 (2011).

[51] S. Gröblacher, J. B. Hertzberg, M. R. Vanner, G. D. Cole, S. Gigan, K. Schwab, and M. Aspelmeyer, Nature Physics **5**, 485 (2009).

[52] J. D. Teufel, D. Li, M. S. Allman, K. Cicak, A. J. Sirois, J. D. Whittaker, and R. W. Simmonds, Nature **471**, 204 (2011).

[53] J. Teufel, T. Donner, D. Li, J. Harlow, M. Allman, K. Cicak, A. Sirois, J. D. Whittaker, K. Lehnert, and R. W. Simmonds, Nature **475**, 359 (2011).

[54] A. H. Safavi-Naeini, J. Chan, J. T. Hill, T. P. M. Alegre, A. Krause, and O. Painter, Phys. Rev. Lett. **108**, 033602 (2012).

[55] N. Brahms, T. Botter, S. Schreppler, D. W. C. Brooks, and D. M. Stamper-Kurn, Phys. Rev. Lett. **108**, 133601 (2012).

[56] T. J. Kippenberg and K. J. Vahala, Science **321**, 1172 (2008).

[57] M. Aspelmeyer, S. Gröblacher, K. Hammerer, and N. Kiesel, J. Opt. Soc. Am. B **27**, A189 (2010).

[58] J. Zhang, K. Peng, and S. L. Braunstein, Phys. Rev. A **68**, 013808 (2003).

[59] T. Palomaki, J. Harlow, J. Teufel, R. Simmonds, and K. Lehnert, Nature **495**, 210 (2013).

[60] S. G. Hofer, W. Wieczorek, M. Aspelmeyer, and K. Hammerer, Phys. Rev. A **84**, 052327 (2011).

[61] S. Mancini, V. Giovannetti, D. Vitali, and P. Tombesi, Phys. Rev. Lett. **88**, 120401 (2002).

[62] T. A. Palomaki, J. D. Teufel, R. W. Simmonds, and K. W. Lehnert, Science **342**, 710 (2013).

[63] S. Mancini, V. I. Man'ko, and P. Tombesi, Phys. Rev. A **55**, 3042 (1997).

[64] S. Bose, K. Jacobs, and P. L. Knight, Phys. Rev. A **56**, 4175 (1997).

[65] W. Marshall, C. Simon, R. Penrose, and D. Bouwmeester, Phys. Rev. Lett. **91**, 130401 (2003).

[66] M. Ludwig, B. Kubala, and F. Marquardt, New Journal of Physics **10**, 095013 (2008).

[67] J. Qian, A. A. Clerk, K. Hammerer, and F. Marquardt, Phys. Rev. Lett. **109**, 253601 (2012).

[68] M. Aspelmeyer, T. J. Kippenberg, and F. Marquardt, Rev. Mod. Phys. **86**, 1391 (2014).

[69] P. Rabl, Phys. Rev. Lett. **107**, 063601 (2011).

[70] T. Hong, H. Yang, H. Miao, and Y. Chen, Phys. Rev. A **88**, 023812 (2013).

[71] E. Wigner, Phys. Rev. **40**, 749 (1932).

[72] R. Graham and F. Haake, *Quantum Statistics in Optics and Solid-state Physics*, Ergebnisse der exakten Naturwissenschaften (Springer, 1973).

[73] P. D. Drummond and C. W. Gardiner, Journal of Physics A: Mathematical and General **13**, 2353 (1980).

[74] W. H. Furry, Phys. Rev. **49**, 393 (1936).

[75] R. Y. Teh and M. D. Reid, Phys. Rev. A **90**, 062337 (2014).

[76] L. Rosales-Zárate, R. Y. Teh, B. Opanchuk, and M. D. Reid, Phys. Rev. A **96**, 022313 (2017).

[77] D. Walls and G. Milburn, *Quantum Optics*, SpringerLink: Springer e-Books (Springer Berlin Heidelberg, 2007).

[78] P. Drummond and M. Hillery, *The Quantum Theory of Nonlinear Optics* (Cambridge University Press, 2014).

[79] H. P. Yuen, Phys. Rev. A **13**, 2226 (1976).

[80] C. M. Caves, Phys. Rev. D **23**, 1693 (1981).

[81] M. D. Reid and P. D. Drummond, Phys. Rev. A **40**, 4493 (1989).

[82] M. D. Reid and P. D. Drummond, Phys. Rev. Lett. **60**, 2731 (1988).

[83] P. D. Drummond and M. D. Reid, Phys. Rev. A **41**, 3930 (1990).

[84] L. Rosales-Zárate, R. Teh, S. Kiesewetter, A. Brolis, K. Ng, and M. Reid, JOSA B **32**, A82 (2015).

[85] Z. Y. Ou, S. F. Pereira, H. J. Kimble, and K. C. Peng, Phys. Rev. Lett. **68**, 3663 (1992).

[86] C. M. Caves and B. L. Schumaker, Phys. Rev. A **31**, 3068 (1985).

[87] P. Drummond and Z. Ficek, *Quantum Squeezing*, Springer Series on Atomic, Optical, and Plasma Physics (Springer Berlin Heidelberg, 2013).

[88] S. Barnett and P. Radmore, *Methods in Theoretical Quantum Optics*, Oxford Series in Optical and Imaging Sciences (Clarendon Press, 2002).

[89] W. P. Bowen, R. Schnabel, P. K. Lam, and T. C. Ralph, Phys. Rev. Lett. **90**, 043601 (2003).

[90] M. D. Reid, P. D. Drummond, W. P. Bowen, E. G. Cavalcanti, P. K. Lam, H. A. Bachor, U. L. Andersen, and G. Leuchs, Rev. Mod. Phys. **81**, 1727 (2009).

[91] D. M. Greenberger, M. A. Horne, and A. Zeilinger, in *Bell's theorem, quantum theory and conceptions of the universe* (Springer, 1989) pp. 69–72.

[92] N. D. Mermin, Physics Today **43**, 9 (1990).

[93] P. van Loock and S. L. Braunstein, Phys. Rev. Lett. **84**, 3482 (2000).

[94] P. van Loock and S. L. Braunstein, Phys. Rev. A **63**, 022106 (2001).

[95] T. Aoki, N. Takei, H. Yonezawa, K. Wakui, T. Hiraoka, A. Furusawa, and P. van Loock, Phys. Rev. Lett. **91**, 080404 (2003).

[96] S. Armstrong, J.-F. Morizur, J. Janousek, B. Hage, N. Treps, P. K. Lam, and H.-A. Bachor, Nature Communications **3**, 1026 EP (2012).

[97] S. Armstrong, M. Wang, R. Y. Teh, Q. Gong, Q. He, J. Janousek, H.-A. Bachor, M. D. Reid, and P. K. Lam, Nature Physics (2015).

[98] M. D. Reid, Phys. Rev. A **88**, 062108 (2013).

[99] E. G. Cavalcanti, C. J. Foster, M. D. Reid, and P. D. Drummond, Phys. Rev. Lett. **99**, 210405 (2007).

[100] Q. Y. He, E. G. Cavalcanti, M. D. Reid, and P. D. Drummond, Phys. Rev. Lett. **103**, 180402 (2009).

[101] Q. Y. He, P. D. Drummond, M. K. Olsen, and M. D. Reid, Phys. Rev. A **86**, 023626 (2012).

[102] G. Svetlichny, Phys. Rev. D **35**, 3066 (1987).

[103] B. Opanchuk, Q. Y. He, M. D. Reid, and P. D. Drummond, Phys. Rev. A **86**, 023625 (2012).

[104] M. D. Reid, Q.-Y. He, and P. D. Drummond, Frontiers of Physics **7**, 72 (2012).

[105] B. J. Dalton, J. Goold, B. M. Garraway, and M. D. Reid, Physica Scripta **92**, 023004 (2017).

[106] B. J. Dalton, J. Goold, B. M. Garraway, and M. D. Reid, Physica Scripta **92**, 023005 (2017).

[107] R. Y. Teh, L. Rosales-Zárate, B. Opanchuk, and M. D. Reid, Phys. Rev. A **94**, 042119 (2016).

[108] B. Opanchuk, L. Rosales-Zárate, R. Y. Teh, and M. D. Reid, Phys. Rev. A **94**, 062125 (2016).

[109] C. F. Wildfeuer, A. P. Lund, and J. P. Dowling, Phys. Rev. A **76**, 052101 (2007).

[110] T. Haigh, A. Ferris, and M. Olsen, Optics Communications **283**, 3540 (2010).

[111] L. D. Carr, D. R. Dounas-Frazer, and M. A. Garcia-March, EPL (Europhysics Letters) **90**, 10005 (2010).

[112] E. G. Cavalcanti and M. D. Reid, Phys. Rev. Lett. **97**, 170405 (2006).

[113] E. G. Cavalcanti and M. D. Reid, Phys. Rev. A **77**, 062108 (2008).

[114] S. J. Jones and H. M. Wiseman, Phys. Rev. A **84**, 012110 (2011).

[115] M. Fuwa, S. Takeda, M. Zwierz, H. M. Wiseman, and A. Furusawa, **6**, 6665 EP (2015).

[116] P. Kok, H. Lee, and J. P. Dowling, Phys. Rev. A **65**, 052104 (2002).

[117] H. Lee, P. Kok, and J. P. Dowling, *Journal of Modern Optics*, Journal of Modern Optics **49**, 2325 (2002).

[118] M. W. Mitchell, J. S. Lundeen, and A. M. Steinberg, Nature **429**, 161 (2004).

[119] P. Walther, J.-W. Pan, M. Aspelmeyer, R. Ursin, S. Gasparoni, and A. Zeilinger, Nature **429**, 158 (2004).

[120] J. P. Dowling, *Contemporary Physics*, Contemporary Physics **49**, 125 (2008).

[121] H. Kim, H. S. Park, and S.-K. Choi, Opt. Express **17**, 19720 (2009).

[122] Y. Israel, I. Afek, S. Rosen, O. Ambar, and Y. Silberberg, Phys. Rev. A **85**, 022115 (2012).

[123] R. Kruse, L. Sansoni, S. Brauner, R. Ricken, C. S. Hamilton, I. Jex, and C. Silberhorn, Phys. Rev. A **92**, 053841 (2015).

[124] I. Afek, O. Ambar, and Y. Silberberg, Science **328**, 879 (2010).

[125] A. Schliesser, R. Rivière, G. Anetsberger, O. Arcizet, and T. J. Kippenberg, Nature Physics **4**, 415 (2008).

[126] J. B. Clark, F. Lecocq, R. W. Simmonds, J. Aumentado, and J. D. Teufel, Nature **541**, 191 (2017).

[127] J.-Q. Liao, H. K. Cheung, and C. K. Law, Phys. Rev. A **85**, 025803 (2012).

[128] H. Carmichael, *Statistical Methods in Quantum Optics 1: Master Equations and Fokker-Planck Equations*, Theoretical and Mathematical Physics (Springer Berlin Heidelberg, 2013).

[129] T. Kippenberg and K. Vahala, Opt. Express **15**, 17172 (2007).

[130] A. Schließer, *Cavity optomechanics and optical frequency comb generation with silica whispering-gallery-mode microresonators*, Ph.D. thesis, lmu (2009).

[131] K. Wagner, J. Janousek, V. Delaubert, H. Zou, C. Harb, N. Treps, J. F. Morizur, P. K. Lam, and H. A. Bachor, Science **321**, 541 (2008).

[132] P. Drummond and I. Mortimer, Journal of Computational Physics **93**, 144 (1991).

[133] P. Kloeden and E. Platen, *Numerical Solution of Stochastic Differential Equations*, Stochastic Modelling and Applied Probability (Springer Berlin Heidelberg, 2011).

[134] M. Werner and P. Drummond, Journal of Computational Physics **132**, 312 (1997).

[135] D. J. Higham, SIAM Review **43**, 525 (2001).

[136] C. Gardiner, *Handbook of Stochastic Methods for Physics, Chemistry, and the Natural Sciences*, Springer complexity (Springer, 2004).

[137] S. Kiesewetter, Q. Y. He, P. D. Drummond, and M. D. Reid, Phys. Rev. A **90**, 043805 (2014).

[138] R. Horn and C. Johnson, *Matrix Analysis* (Cambridge University Press, 1990).

[139] B. Opanchuk, *Quasiprobability methods in quantum interferometry of ultracold matter*, Ph.D. thesis, Swinburne University of Technology (2014).

[140] B. Yurke and J. S. Denker, Phys. Rev. A **29**, 1419 (1984).

[141] M. J. Collett and C. W. Gardiner, Phys. Rev. A **30**, 1386 (1984).

[142] C. W. Gardiner and M. J. Collett, Phys. Rev. A **31**, 3761 (1985).

[143] B. Yurke, Phys. Rev. A **32**, 300 (1985).

[144] A. Gilchrist, C. W. Gardiner, and P. D. Drummond, Phys. Rev. A **55**, 3014 (1997).

[145] P. Deuar and P. D. Drummond, Phys. Rev. A **66**, 033812 (2002).

[146] J. I. Cirac, P. Zoller, H. J. Kimble, and H. Mabuchi, Phys. Rev. Lett. **78**, 3221 (1997).

[147] H. J. Kimble, Nature **453**, 1023 (2008).

[148] S. Ritter, C. Nölleke, C. Hahn, A. Reiserer, A. Neuzner, M. Uphoff, M. Mücke, E. Figueroa, J. Bochmann, and G. Rempe, Nature **484**, 195 (2012).

[149] R. Y. Teh, S. Kiesewetter, M. D. Reid, and P. D. Drummond, Phys. Rev. A **96**, 013854 (2017).

[150] Q. Y. He, M. D. Reid, E. Giacobino, J. Cviklinski, and P. D. Drummond, Phys. Rev. A **79**, 022310 (2009).

[151] Q. Y. He, M. D. Reid, and P. D. Drummond, Opt. Express **17**, 9662 (2009).

[152] F. Marquardt, J. P. Chen, A. A. Clerk, and S. M. Girvin, Phys. Rev. Lett. **99**, 093902 (2007).

[153] I. Wilson-Rae, N. Nooshi, W. Zwerger, and T. J. Kippenberg, Phys. Rev. Lett. **99**, 093901 (2007).

[154] S. Kiesewetter, R. Polkinghorne, B. Opanchuk, and P. D. Drummond, SoftwareX **5**, 12 (2016).

[155] E. Verhagen, S. Deléglise, S. Weis, A. Schliesser, and T. J. Kippenberg, Nature **482**, 63 (2012).

[156] C. E. Shannon, Proceedings of the IEEE **86**, 447 (1998).

[157] S. Groblacher, K. Hammerer, M. R. Vanner, and M. Aspelmeyer, Nature **460**, 724 (2009).

[158] R. Andrews, A. Reed, K. Cicak, J. Teufel, and K. Lehnert, Nature Communications **6** (2015).

[159] U. Akram, N. Kiesel, M. Aspelmeyer, and G. J. Milburn, New Journal of Physics **12**, 083030 (2010).

[160] A. Furusawa, J. L. Sørensen, S. L. Braunstein, C. A. Fuchs, H. J. Kimble, and E. S. Polzik, Science **282**, 706 (1998).

[161] W. P. Bowen, N. Treps, B. C. Buchler, R. Schnabel, T. C. Ralph, H.-A. Bachor, T. Symul, and P. K. Lam, Phys. Rev. A **67**, 032302 (2003).

[162] C. Wittmann, U. L. Andersen, M. Takeoka, D. Sych, and G. Leuchs, Phys. Rev. Lett. **104**, 100505 (2010).

[163] L. E. C. Rosales-Zárate and P. D. Drummond, Phys. Rev. A **84**, 042114 (2011).

[164] K. E. Cahill and R. J. Glauber, Phys. Rev. **177**, 1882 (1969).

[165] B. Schumacher, Phys. Rev. A **54**, 2614 (1996).

[166] K. Hammerer, M. M. Wolf, E. S. Polzik, and J. I. Cirac, Phys. Rev. Lett. **94**, 150503 (2005).

[167] A. P. Reed, K. H. Mayer, J. D. Teufel, L. D. Burkhart, W. Pfaff, M. Reagor, L. Sletten, X. Ma, R. J. Schoelkopf, E. Knill, and K. W. Lehnert, ArXiv e-prints (2017), arXiv:1703.02548 [quant-ph] .

[168] S. Kiesewetter, R. Y. Teh, P. D. Drummond, and M. D. Reid, Phys. Rev. Lett. **119**, 023601 (2017).

[169] L. Diósi, Phys. Rev. A **40**, 1165 (1989).

[170] R. Penrose, General Relativity and Gravitation **28**, 581 (1996).

[171] L. Diósi, Journal of Physics A: Mathematical and Theoretical **40**, 2989 (2007).

[172] P. D. Drummond and M. D. Reid, Presented at 605 WE-Heraeus-Seminar (Physikzentrum Bad Honnef, Germany, 2016).

[173] J. D. Simon, *Review of Scientific Instruments*, Review of Scientific Instruments **60**, 3597 (1989).

[174] G. Hétet, J. J. Longdell, A. L. Alexander, P. K. Lam, and M. J. Sellars, Phys. Rev. Lett. **100**, 023601 (2008).

[175] V. Giovannetti, S. Mancini, D. Vitali, and P. Tombesi, Phys. Rev. A **67**, 022320 (2003).

[176] V. Giovannetti, S. Mancini, and P. Tombesi, EPL (Europhysics Letters) **54**, 559 (2001).

[177] M. I. Kolobov and I. V. Sokolov, Optics and Spectroscopy **62**, 69 (1987).

[178] C. W. Gardiner, Phys. Rev. Lett. **70**, 2269 (1993).

[179] H. J. Carmichael, Phys. Rev. Lett. **70**, 2273 (1993).

[180] V. Coffman, J. Kundu, and W. K. Wootters, Phys. Rev. A **61**, 052306 (2000).

[181] G. Adesso, A. Serafini, and F. Illuminati, Phys. Rev. A **73**, 032345 (2006).

[182] G. Adesso and F. Illuminati, Phys. Rev. Lett. **99**, 150501 (2007).

[183] G. Adesso, D. Girolami, and A. Serafini, Phys. Rev. Lett. **109**, 190502 (2012).

[184] S. M. Tan, Phys. Rev. A **60**, 2752 (1999).

[185] L.-M. Duan, G. Giedke, J. I. Cirac, and P. Zoller, Phys. Rev. Lett. **84**, 2722 (2000).